Antal Kerpely Doctoral School of Materials Science and Technology

Evaluation of conventional sintering, induction sintering, and selective laser melting manufacturing procedures of 17-4PH materials

PhD dissertation

By

Mohammed Qasim Kareem/Yasi

(M.Sc. in Metallurgical Engineering)

Prof. Dr. Zoltan Gacsi, Professor

Dr. Gréta Gergely, Associate Professor

Head of the Doctoral School

Prof. Dr. Valéria Mertinger

Miskolc, 2025

بِسْمِ اللَّـهِ الرَّحْمَـٰنِ الرَّحِيمِ

وَأَنْ لَيْسَ لِلْإِنْسَانِ إِلَّا مَا سَعَى ﴿٣٩﴾

And that man shall have nothing but what he strives for- (39)

وَأَنَّ سَعْيَهُ سَوْفَ يُرَى ﴿٤٠﴾

And that his striving shall soon be seen- (40)

ثُمَّ يُجْزَاهُ الْجَزَاءَ الْأَوْفَى ﴿٤١﴾

Then shall he be rewarded for it with the fullest reward- (41)

Sura 53: AN-NAJM (THE STAR), Quran Karim.

ACKNOWLEDGEMENT

The thanks and gratitude should first be directed to Allah, the Exalted, the Majestic. Secondly, I extend my appreciation to myself for my efforts, my challenging days, my strength, my mindset, my persistence, my determination, my plans, my tears, my moments of struggle, my days of solitude, my goals, and my faith in Allah (the Exalted, the Majestic) and in myself. Special thanks to my family, especially my mother and father, for their unwavering support, their belief in me, and their prayers.

I would like to express my deepest appreciation to my supervisors, **Prof. Dr. Zoltán Gácsi** and **Dr. Gréta Gergely,** for their guidance, support, commitment, advice, and the opportunities they provided.

I would also like to express my deepest gratitude to **Dr. Tamas Miko** for his exceptional assistance, kind and respectful communication, and unwavering support. Words cannot fully capture his kindness and support from the beginning of my Ph.D. studies to the end. We consistently collaborated, devising numerous plans and uncovering many side effects not documented in the literature. These experiments required significant time and effort but ultimately enhanced our expertise in my field of study.

I would like to extend my gratitude to all the esteemed professors at the University of Miskolc who taught me various subjects during the first two years of the Ph.D. program. The author sincerely thanks **Mr. Kovacs Arpad** for his contributions to the SEM and EDX analyses, **Dr. Ferenc Kristály** for his work on the X-ray analysis, and **Dr. Dániel Koncz-Horváth** for the FIB-SEM analysis. I also wish to express my appreciation to the reviewer, **Prof. Dr. László Varga**, for his insightful comments and suggestions on my semester reports for the Ph.D. study. Additionally, I would like to convey my deepest appreciation to all the staff members of the Antal Kerpely Doctoral School of Materials Science and Technology, University of Miskolc, for their advice, technical support, ongoing assistance, and cooperation during the implementation of the experimental work over the past years. I would like to express my sincere gratitude to **Ms. Agnes Solczi** for her support and kind communications. I would like to express my sincere gratitude to the Tempus Public Foundation (Stipendium Hungaricum) for the scholarship.

LIST OF ABBREVIATIONS AND NOTATIONS

PSM	Press and sinter method
MIM	Metal powder injection molding
HPAT	High-performance atomisation
CAT	Conventional atomization
WA	Water atomised
HVn	Vickers hardness, n represents the applied load
HK	Knoop hardness
HRB	Rockwell B hardness
HRA	Rockwell A hardness
RC	Rockwell C hardness
HB	Brinell hardness
--	Not provided
Y.S.	Yield strength (MPa)
UTS	Ultimate tensile strength (MPa)
FDM	Fused deposition modeling (a 3D printing process)
LPBF	Laser powder bed fusion (a 3D printing process)
SLM	Selective laser melting
ρ	Laser power, (w)
ν	Laser speed, (mm/s)
t	Layer thickness, (µm)
H	Hatching distance, (µm)
H900	Ageing at 482 °C for 4-hours
H1100	Ageing at 552 °C for 4-hours
H1150	Ageing at 620 C for 4-hours
δ-ferrite	Delta-ferrite phase (formed at high temperature)
ICP-OES	Inductively coupled plasma optical emission spectrometry
wt.%	Weight percentage
DSS	Different stainless-steel powders
GB	Grian boundary
Bal.	Balance
OM	Optical microscope
IJ	ImageJ software
SEM	Scanning electron microscopy
SE	Second electron microscopic
EDS	Energy dispersion spectroscopy
DSC	Differential scanning calorimetry technique
XRD	X-ray diffraction
FIB	The focused ion beam
DP	The densification parameter
DCTT	Different cold pressing, sintering temperature and time
BCC	Body-centered cubic
FCC	Face-centered cubic
BCT	Body-centered tetragonal
α	Ferrite phase (formed at room temperature)

ά	Martensite
γ	Austenite
O and R	Original and recycled
PP	Perimeter frequencies
INDS	Induction sintering
EBSD	Electron back scatter diffraction
IQ	Quality image
IPF	Inverse pole figure

TABLE OF CONTENT

Contents

LIST OF TABLES

LIST OF FIGURES

1. CHAPTER 1: Introduction

The press and sinter method (PSM) remains the leader in manufacturing ferrous parts among all other powder metallurgical methods worldwide. According to Figure 1(a), the ferrous products obtained through PSM accounted for 63% of the total. A report on the metal powder market size in the United States from 2016 to 2027, which is shown in Figure 1(b), explains the high demand for PSM products compared to additive manufacturing (AM), metal powder injection molding (MIM), and hot isostatic pressing (HIP). The PSM offers low-cost stainless-steel products, net-shaping processing at relatively low sintering temperatures, customised microstructures, beneficial mechanical properties, high surface finishing and dimensional accuracy, and does not cause high pollution [1], [2], [3], [4], [5], [6], [7]. To gain perspective on more advantages of PSM, one can compare it with MIM technology. MIM includes the preparation of the starting material (polymer blend with metal-like properties), injection molding, debinding, and sintering [8], [9], [10], [11]. The PSM involves the compaction of the powder (metal or metal alloy, with or without binders), usually in molds, followed by sintering of the molded bodies [6], [7]. The thermal debinding in a high-temperature burnout furnace should be done before sintering in the MIM process, which takes up to 50 hours [4]. In contrast, there is no debinding step in PSM and less periods of sintering cycle. Another advantage of PSM is that the particles bond together directly (without organic materials such as wax), resulting in less oxidation compared with MIM [12].

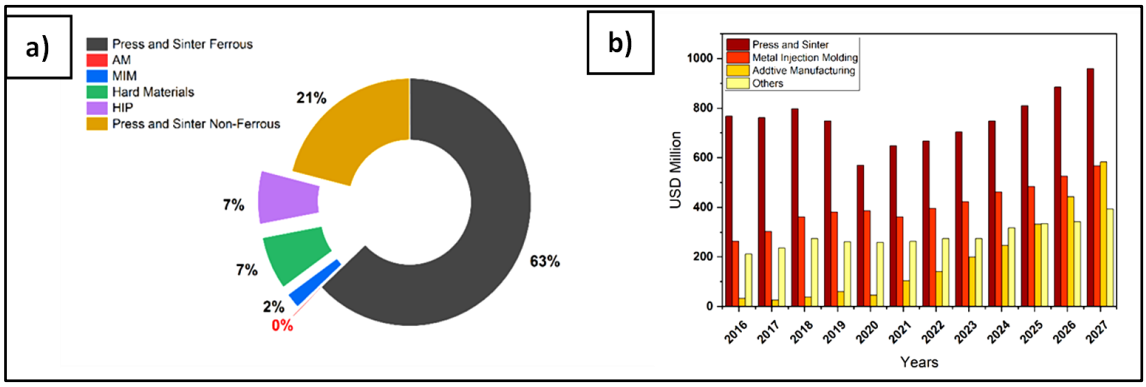

Figure 1.The use of press and sinter technology compared to other processes for producing powdered materials in a) Europe in 2019 and b) the US market over a range of years (according to [13])

17-4PH grade, a precipitation-hardened martensitic stainless steel, has a wide range of applications in the medical, shipbuilding, food, chemical, nuclear, and automotive industries

[1], [14], [15], [16], [17]. 17-4PH parts are typically used in the aerospace, chemical, petrochemical, and general metal processing industries [4], [13], [18], [19]. Designers and engineers prefer 17-4PH stainless steel because of its beneficial properties such as high strength, hardness, easy modification by heat treatment, and corrosion resistance at temperatures below 300 °C [19], [20], [21]. This is attributed to the alloy containing more chromium and nickel [22], [23]. 17-4PH is usually chosen to produce stainless steel materials with high strength and medium ductility[22], [24]. However, unfortunately, PSM could not previously be used to produce high-density parts from 17-4PH powder due to the poor compressibility of the 17-4PH powder, 17-4PH stainless steel is four times harder than 316L stainless steel[13]. Therefore, few PSM studies were published. The low compressibility of the 17-4PH powder, which leads to low densification, was the main reason for few PSM studies [25], [26], [27]. PSM can produce stainless-steel parts with a sintered density of 6.8 to 7.3 g/cm^3 [28]. In contrast, the theoretical density of 17-4PH materials reported in the literature ranges from 7.75 to 7.85 g/cm^3 [29]. However, since both MIM and PSM have similar sintering phenomena, the studies on MIM 17-4PH can be utilised in this dissertation as supportive references.

Additionally, this dissertation work investigated several factors influencing the limitations of PSM 17-4PH parts. These factors included applying high cold pressing, utilising conventional and induction furnaces for low and high sintering temperatures, and sintering for various short and long times. Additionally, these investigations performed, for the first time, using gas-atomised instead of water-atomised 17-4PH powder, the water-atomised 17-4PH powder is common for PSM 17-4PH parts. Moreover, the compaction behiavour of the 17-4PH powder, under high cold pressing, versus different types of stainless steels with different hardnesses was examined also. The effect of decreasing the 17-4PH powder particle size on the densification property and recyclability of 17-4PH from the 3D printing process to produce PSM 17-4PH parts were investigated as well. Furthermore, different primary SLM parameters were investigated to produce high density SLM 17-4PH parts. A heat-treatment condition was applied to compare the physical-mechanical properties of 17-4PH parts produced by sintering and melting routes. A comprehensive review of the literature was conducted, highlighting the existing knowledge gap. Objectives were established, experiments were designed, conducted, and evaluated scientifically, and subsequently presented for consistency.

2. CHAPTER 2: Literature review:

Earlier studies attempted to increase the sinter density of 17-4PH parts produced by PSM. In 1994, Reinshagen and Witsberger demonstrated that aged, sintered PSM 17-4PH parts could achieve a relative sinter density of 93.47% [8]. Moreover, Schade et al. discovered that cutting the carbon content of conventional water-atomized 17-4PH powder (0.023 wt.% carbon) in half with an HPAT technique increased the relative sinter density to 94.75% [25]. Additionally, in 2008, water-atomized PSM 17-4PH parts that were sintered and heat-treated reached the maximum relative sinter density of 92.45% [8]. In 2013, it was found that increasing the sintering temperature improved the sinter density by 92.19%.3 Moreover, adding 0.6 wt.% of boron increased the relative sinter density of PSM 17-4PH parts from 84.54% to 96.4% [20].

As a result of the above literature, PSM is still the most demanded technology worldwide in the powder metallurgy market for producing stainless-steel parts. According to Figure 1(b), PSM will also be demanded in the future. However, PSM is still unable to provide high-density 17-4PH parts. The densification is considerably affected by many forming factors such as cold pressing, powder compressibility, powder particle shape, particle size distribution, sintering temperature and time, and sintering atmosphere.

2.1 Press and sinter method

2.1.1 Cold pressing

The densification of green compacts (i.e. compacted powders before sintering) affects the strength and shrinkage ratio of the sintered parts. Lower green density means lower sinter density [25], and increased sinter shrinkage[30]. Consequently, low sinter density leads to poor mechanical properties [31].

Cold pressing is the process of repackaging metal powders. Pressing begins with the reduction of the pore space and increasing the powder's efficiency, eliminating the bridges created during filling, and forming new surfaces free of oxide [32]. However, the metal powder's compressibility (hardness) is the main factor that directly affects green densification. The high compressibility of metal powder (low hardness) leads to an elevated green density. The effect of cold pressing on metal powders with different hardness (pure iron 104 HV, titanium 144 HV, and 304L 205 HV) was investigated [33]. The findings indicated that the powder hardness and densification behavior had an inverse relationship. Moreover, different powders of stainless steel with different compressibility (434L, 304L, and 17-4PH) were cold pressed up to 690 MPa

[25]. The results showed that the parts made from 434L and 304L (high ferrite content and high compressibility) had a higher density than those made from 17-4PH (containing martensite and low compressibility). Since ferrite is less hard than martensite, it is possible to achieve higher green and sinter densities [34].

Additionally, the effect of cold pressing on the green densification of PSM stainless steel have been investigated. These investigations are summarised in Table 1. The increase in cold pressing from 600 to 760 MPa increased the relative green density from 76.82% to 80.67% for PSM 17-4PH parts. Additionally, the effect of particle size distribution has been investigated, which is also presented in Table 1. The lowest average particle size was around 45 μm. It also indicates that the rise in cold pressing has had a more significant effect than reducing particle size on improving green densification. Additionally, the fraction of pores decreases with increasing cold pressing, and the shapes of pores change from irregular to more spherical shapes. According to a previous study, increasing the cold pressing from 200 to 600 MPa transformed the shapes of the pores of 316L into regular shapes, and the volume fraction of regular pores increased from 10% to 22% [35]. Low porosity and more regular pores shapes lead to improve the mechanical properties of PSM stainless-steel parts.

Table 1. Effects of cold pressing on green densifications of different PSM stainless-steel parts.

Stainless steel powder	Particle size, μm	Cold pressing, MPa	Green density, %	Ref.
WA-17-4PH	Average-60	600	76.82	[24]
WA-17-4PH	45 - 150		80.67	[36]
WA-17-4PH		690	80.67	[25]
WA-17-4PH		760	80.67	[37]
WA-316L	~ 45 - 50	200	69	[35]
WA-316L	45 - 150	400	74	[36]
WA-316L		600	81	
WA-17-4PH		400	72	
WA-316L	~ 45 - 50	600	83	[35]
WA-316L	150		87.41	[38]

2.1.2 Sintering

The energy stored in the cold-pressed metal part is released during sintering. Sintering is a complicated process in which the development of the microstructure occurs through the action of several different transport mechanisms [39]. In the solid state, the sintering of crystalline

solids can occur by vapor transport, and surface, lattice, or grain boundary diffusion, in addition to plastic deformation by dislocation migration [40]. In the sintering of powdered steel, the green parts are solidified to the desired composition using temperatures below the melting point (but above half the melting temperature) for the appropriate amount of time [32]. During the sintering process, there are three kinetic stages: bonding after the reduction of oxides from the surfaces of powder particles (bonding between adjacent particles with the formation necks); densification (adhesion between the solid and porous phases); and grain coarsening (significant grain growth and interaction between pores and grain boundaries) [41]. Thus, a higher green density, which means there are more points of contact between the particles, speeds up adhesion and densification during sintering [32]. An example of the conventional sintering stages for a 17-4PH part is presented in Figure 2.

Generally, the sintering process for iron-based compacted materials is conducted using a conventional electric furnace[42]. The sintering cycle lasts approximately 8 to 12 hours in the traditional sintering process due to the slow heating and cooling rates dictated by heat transfer through radiation, which prolongs the process [43]. As an alternative to conventional sintering methods, innovative rapid sintering processes have emerged, including microwave, plasma, laser, and induction heating (sintering) [42]. Research has indicated that each of these techniques offers potentially significant advantages, but they also come with limitations. For instance, the effectiveness of microwave sintering has been demonstrated across various ceramic systems. However, it remains challenging for metallic powders, as metallic materials tend to reflect microwave energy rather than absorb it [43]. Therefore, induction sintering is an alternative heating method applicable to conductive materials. Induction sintering heats samples through induced eddy currents generated by an alternating magnetic field, making it feasible only with conductive materials [44]. The mechanism of induction sintering for densifying stainless-steel parts follows the same kinetics as other powder metallurgy sintering strategies, consisting of three clearly defined stages [44]. Neck growth is initiated, where particles in direct contact form grain boundaries through atomic diffusion, and necks begin to develop at the contact points (stage I). Surface diffusion is the primary mass-transport mechanism at this stage. The intermediate sintering stage is marked by the densification and grain growth of the samples, with pores becoming isolated and closed (stage II). Grain boundary diffusion prevails at this stage, leading to the migration of material from the core of the powder particles to the surface,

resulting in densification. Finally, we showcase the last sintering stage (stage III). Once most pores are closed and grain boundaries increase, the gas trapped within the pores escapes to the surface, subsequently reducing the volume of the sintered part. Furthermore, induction sintering possesses several characteristics, including the ability to produce high temperatures across a suitable range, adjustable high heating and cooling rates, rapid control, high energy efficiency, and a simple, relatively inexpensive equipment setup [43], [45], [46] Early research on induction sintering for metal powders primarily focuses on Fe-based powders. The physical and mechanical properties of induction-sintered Fe-based compacts are superior to those of conventional sintered parts, and they also improve with longer sintering times [42], [47]. However, the application of induction sintering has not been previously explored in the context of 17-4PH stainless steel compacted materials.

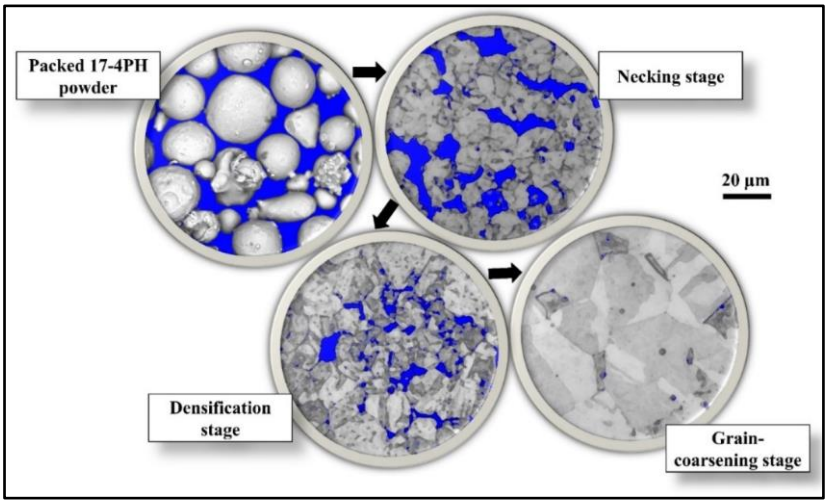

Figure 2. An example of the conventional sintering stages of a 17-4PH part. Note: the blue colour indicates porosity.

The signals for the beginning of the sintering process of 17-4PH parts, manufactured by PSM or MIM, can be constructed by dilatometric measurements of sintering peaks. The majority of studies discovered that, regardless of lubricant, debinding conditions, or protective atmosphere, the sintering behavior of PSM and MIM 17-4PH parts is similar [9], [24], [36], [48]. According to those studies, several dilatometric peaks can describe the sintering process and phase transformations of 17-4PH sintered parts. They showed the following peaks:

1. Between 725 and 750 °C, the peak of thermal expansion shows that martensite BCC is transforming into austenite FCC.

2. The initial sintering shrinkage peak appeared between 964 and 1050 °C.
3. The isothermal sintering peak can be seen at temperatures ranging from 112 to 1143 °C. This peak started with heating shrinkage and ended with delayed shrinkage.
4. The hydrogen peak shows that high sinterability can be reached by reducing the silicon oxides that cover the 17-4PH powder between 1250 and 1308 °C. This peak is reached when hydrogen is used as a protective atmosphere.

2.2 Factors related to the properties of sintered stainless-steel materials

2.1.1 Sintering time and temperature

Densification

Increasing the sintering temperature and time improves the density. The effect of sintering temperature on the densification of PSM 316L parts was investigated [35]. The relative sintering density of PSM 316L parts produced at 800 MPa increased from 79.88% to 87.71% by increasing the sintering temperature from 1200 to 1300 °C [49]. Moreover, applying a high sintering temperature of 1400 °C to 316L parts (cold pressed at 600 MPa) increased the relative sintering density to 92%. The impacts of different sintering temperatures and times on the densification of PSM 17-4PH parts cold pressed at 600 MPa were also investigated [36]. The relative sintering density increased proportionally from 84.5% to 89% as the sintering temperature increased from 1200 to 1300 °C, for a sintering time of 60 min. Extending the sintering time from 60 to 120 min at a sintering temperature of 1300 °C increased the relative sintering density from 89% to 92%. Further experiments performed to improve the sintering densification of PSM 17-4PH parts are summarized in Figure 3. Increasing the sintering temperature from 1300 to 1340 °C for the same sintering time and cold pressing (60 min, 600 MPa) resulted in a 2.3% increase in the relative sinter density. In addition, increasing the sintering time from 20 to 60 min at a fixed cold pressing and sintering temperature (690 MPa, 1260 °C) was investigated.20 The results showed an increase in the relative sintering density from 89.6% to 93.47% for 20 and 60 min, respectively.

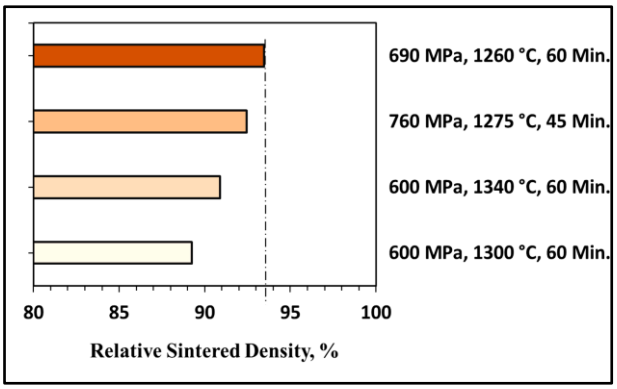

Figure 3. The sinter densification of press and sinter 17-4PH products at (a) different conditions (produced from [24], [25], [51]) (produced from [24], [25], [50])

Increasing the sintering temperature and time affects the ratio and shape of the pores. In a previous study, the relative density of 17-4PH samples prepared by MIM was controlled from 61% to 99% by increasing the sintering temperature from 1200 to 1350 °C.28 The results showed that not only did the pore fraction decrease but also the shapes of the pores became more regular as the sintering temperature increased. Additionally, the relative sinter density of MIM 17-4PH parts increased up to 98% when the sintering temperature was increased from 1150 to 1300 °C under the same production conditions [51]. In addition, the effect of sintering time and temperature on the densification of a MIM 17-4PH part containing 1% FeB was investigated [52]. The results showed that changes in sintering temperature, from 1265 to 1285 °C, and time, from 10 to 45 min, led to a nearly complete density (around 99%) due to the formation of the eutectic liquid phase (δ-ferrite), which exhibited high diffusivity and rapid densification.

However, increasing the sintering time at elevated temperatures can lead to overheating of the steel structure. For example, the effect of using different sintering times on the properties of HK30, an austenitic stainless steel, was studied [53]. Sintering at 1270, 1280, and 1300 °C revealed that, for the same holding time, density increases with increasing temperature. At 1280 °C, the highest density of 7.61 g/cm^3 was reached after seven hours of holding time, and further holding led to a slightly lower density, indicating the possibility of overheating. A higher sintering temperature of 1300 °C led to the overheating of the microstructure, reducing the bond strength between grain boundaries. As a result, the density and mechanical properties decreased further.

Mechanical properties

The porosity ratio affects the mechanical and physical properties of powdered steel parts. The balanced effects of reduced porosity and grain coarsening enhanced tensile strength and elongation, while yield strength remained unchanged [54]. Usually, a decrease in porosity raises the yield strength, but it was terminated by the grain-coarsening phenomenon. Moreover, by increasing the sintering time from 20 to 60 min, the sintered density of conventional water-atomized 17-4PH green compacts has increased from 87 to 93.4% [13]. The high density resulted in high mechanical properties. Conversely, pores reduce mechanical properties by acting as stress concentrations and promoting fracture growth [55]. In another study, when the sintering time was increased from 20 to 40 min, the sinter density increased, and subsequently, the hardness increased from 59 to 65 HRA [25]. In addition, the effect of different sintering temperatures on MIM 17-4PH parts was investigated [10]. The results showed that the 17-4PH parts had a higher relative density at the high sintering temperature of 1360 °C than at 1200 °C, but there was no significant change in hardness. Table 2 presents the mechanical properties of

Table 2.The mechanical properties of various stainless-steel parts produced by PSM are compared to those made using other processing methods.

Stainless-steel	**Green density, %**	**Sinter density, %**	**Hardness**	**Yield strength, MPa**	**Ref.**
WA-17-4PH	80.67	93.47	HRA= 65	--	[25]
WA-17-4PH	80.67	92.45	HRB= 89	768	[37]
WA-17-4PH	76.82	91.24	--	~ 580	[24]
WA-316L	69	84	HV5=119±5	135±3	[35]
WA-316L	83	92	HV5=159±4	224±26	[35]
WA-316L	--	90.25	HV10 = 189	--	[14]
Wrought 316L	--	--	HV5= 220	172	[35]
17-4PH cast	--	--	HV10= 366	--	[56]
17-4PH warm-forming sheet	--	--	--	986	[57]

previously studied 17-4PH and 316L parts produced through PSM processes, in comparison to other traditional methods (casting and wrought). Increased green density results in higher sinter density, which in turn enhances hardness and yield strength, irrespective of the stainless-steel type. Furthermore, the low sinter density of PSM stainless steel leads to inferior mechanical properties when compared to cast and wrought stainless steel.

Pores and grain size

Multiple factors influence the shape of the pores, including the powder particle morphology, sintering temperature and time, and the atmosphere. Using gas-atomized and water-atomized powders for producing MIM 17-4PH parts has been investigated [58]. The sintering results at 1250 °C showed that the pores between particles were quite different for the MIM 17-4PH made of gas-atomized and water-atomized powders. Spherical powder particles produce more rounded pores compared to irregular powder particles. The shape of the particles in gas-atomized samples is spherical, while it is irregular in water-atomized samples. In another study, the MIM 17-4PH parts sintered at 1300 °C had round pores compared to those sintered at 1150 °C [59]. Consequently, the mechanical properties of the sintered 17-4PH materials may be related to the pore shapes, which are related to the form of the powder particles, as mentioned earlier. The tensile properties of MIM 17-4PH parts made from gas-atomized powder over a range of sintering temperatures (1250−1350 °C) were around 10% higher than those of these parts made from water-atomized powder [60]. More rounded pores also led to higher ductility [23]. Regular pore geometries and low porosity at elevated sintering temperatures contributed to the increase in the tensile strength of parts made of chromium alloy steel that were produced by PSM [30]. However, water-atomised stainless-steel powder was chosen for the manufacturing of PSM parts, as there was no research utilising gas-atomised powder for producing PSM stainless steel components.

Furthermore, high porosity causes the hardness values to vary within the same manufactured part. For wrought steel, the porosity reduces heat transfer, favoring bainite formation rather than martensite, which may explain the tremendous difference in hardness with decreasing density [61]. Additionally, the martensite phase is harder than the bainite phase.

The effect of sintering temperature or time on the shapes of the pores has also been observed in PSM 316L parts. Both the 17-4PH and 316L parts showed similar sintering behavior [36]. Increasing the sintering temperature from 1200 to 1300 °C for PSM 316L parts decreased the pore fraction from 20% to 12%, and the shapes of the pores changed from irregular to more regular[62]. However, sintering at a temperature of 1200 °C was considered insufficient and resulted in low mechanical properties [49]. Increasing the sintering time and temperature increases grain growth and decreases the porosity ratio and the diameter of the pores [54]. For example, the average grain sizes of the samples were 45, 64, and 76 μm after sintering at 1280

°C for 5, 7, and 9 h, respectively[63]. The higher the sintering temperature, the larger the average grain size [64]. However, mechanical properties depend more on porosity than on grain size, because the fracture is mostly caused by the growth of micropores and coalescence [54].

2.1.2 Particle size and carbon content

Fine powder particles and low-carbon content improve the densification properties of 17-4PH parts. The effect of gas-atomized 17-4PH powders in the range of 10 to 32 μm was investigated by MIM [60]. The result showed that the particle size distribution at higher sintering temperatures (above 1300 °C) had little effect on the tensile strength. On the contrary, the highest strength properties were obtained at the lowest sintering temperature (1149 °C) with the lowest particle size (10 μm).

There is an inverse connection between the carbon content and the densification property of powdered steel materials. The effect of using water-atomized 17-4PH powder was studied, but it was prepared using two different methods: CAT and HPAT [25]. HPAT 17-4PH powder has lower carbon and nitrogen content and finer particles than the CAT powder. The results showed that the sintered parts made of HPAT powder had a higher density (7.4 g/cm3) than those made of CAT powder (7.3 g/cm3), regardless of the sintering conditions. Moreover, parts with low-carbon content in the range of 0.02 to 0.04 wt.% gave optimum combinations of strength and ductility, although the wide specification range for carbon is 0.00 to 0.070 wt.% in the MIM 17-4PH parts [23]. The percentage of carbon in low-carbon stainless steel must be kept low to prevent carbide precipitation from chromium carbides. For example, in austenitic stainless steels that are cooled slowly, the carbon content must be in the range of 0.02–0.03 wt.%. The results showed that, as the amount of carbon in the material increased, the tensile strength, yield strength, and hardness all increased, but elongation decreased [32].

The phase diagram of 17-4PH with a carbon content of less than 0.04 wt.% indicates that the liquid phase occurs slightly above 1360 °C (Figure 4) [4]. The formation of δ-ferrite during high sintering temperatures and the development of the microstructure during sintering are summarized in the following structures: α; γ; and γ + δ-ferrite. The phase diagram shows that the formation of δ-ferrite strongly depends on the carbon content, and δ-ferrite drops with increasing carbon content [65]. However, an investigation of the microstructural evolution of MIM 17-4 PH stainless steel at room temperature revealed that a martensitic phase occurs [66]. The martensite transforms into γ at approximately 700 °C. The second-phase transformation is

the transformation of γ to δ-ferrite, which starts at nearly 1200 °C and is related to the dilatometric peaks explained in the sintering section (2.1.2).

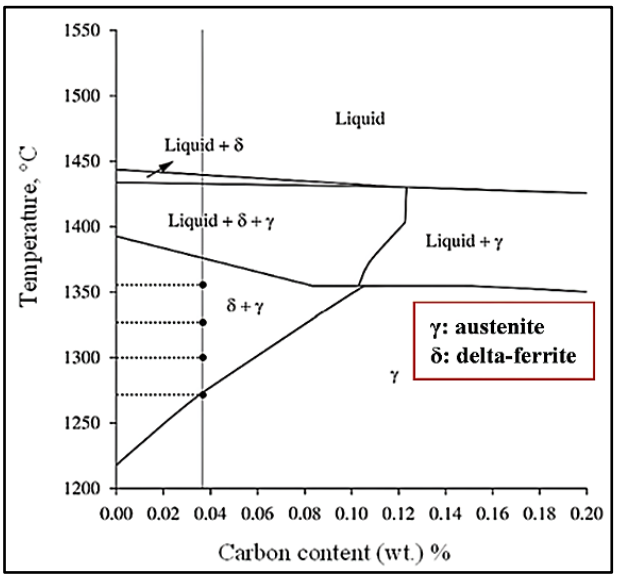

Figure 4.Phase diagram of 17-4PH alloy (reproduced from [4]). reproduced from [4]).

2.1.3 Sintering atmosphere and oxidation

Atmosphere

By controlling the phases in the microstructures of 17-4PH materials, it is possible to determine a connection between the sintering atmosphere and the densification property. δ-ferrite formation in PSM 17-4PH parts produced under different sintering atmospheres has been studied [48]. The results demonstrated that the formation of δ-ferrite commenced in a pure hydrogen (H_2) environment at sintering temperatures exceeding 1220 °C, which can occur along the grain boundaries. Other results obtained using H_2 and hydrogen/nitrogen (H_2/N_2) atmospheres at an elevated sintering temperature (1360 °C) revealed that no δ-ferrite phase formed and that the microstructure contained significant amounts of porosity. Additionally, it was mentioned that δ-ferrite formation can occur at a temperature lower than 1220 °C, according to the two-phase master sintering curve model [66]. Moreover, Ar +20% H_2 was used as an atmosphere to sinter PSM 17-4PH green compacts [67]. A range of sintering temperatures from 1240 to 1290 °C for 90 min was used. A chromium–nickel–martensite matrix with a few small islands of δ-ferrite at the grain boundaries comprised the final microstructure. Thus, the formation temperature of the δ-ferrite depends on the chemical composition of the powder, the sintering atmosphere, and the residual carbon [58].

Overall, sintering in a vacuum atmosphere lowers the oxygen content. For example, the results of sintering water-atomized iron powder pre-alloyed with 1.8 wt.% Cr showed that the oxygen content in the green compacts before sintering was 0.15 wt.%, while the highest oxygen content after sintering in a vacuum was 0.02 wt.% [30]. To achieve a higher final density, oxidation during sintering should be avoided entirely. Sintering in an Ar atmosphere or vacuum is the preferred choice for 17-4PH materials. Depending on the sintering atmosphere, Cr_2O_3 may be formed. The effect of using different sintering atmospheres (vacuum, Ar, and N_2/H_2) to produce MIM parts from gas-atomized 17-4PH stainless-steel powder was investigated by X-ray analysis [12]. No oxygen was found in the case of vacuum or Ar, whereas oxygen was observed when N_2+H_2 was used as a protective atmosphere. Cr_2O_3 was created after sintering in the N_2+H_2 atmosphere, but no Cr_2O_3 was formed when sintering in the Ar and vacuum atmospheres. In addition, it was found that the increase in Cr_2O_3 was related to the higher sintering temperature Cr_2O_3 formed on the surface of the sintered particles, which stopped diffusion and made the material less dense.

Oxides source

Steel powder atomised with water contains more oxide than powder atomized with gas, such as Cr_2O_3, NiO, and SiO_2.Therefore, water-atomized sintered powdered materials will always contain small amounts of fine oxides [23]. In addition, these oxides might exist either on the surface or within the particles. As mentioned previously, surface oxides need to be reduced for sinter necks to form between powder particles. The transformation of the surface oxides and their entrapment inside the sinter necks can occur during the heating phase [30]. Oxidized particles enriched with Si and Mn were found on the surface of H13 steel powder atomized with water [64]. After sintering, these oxide particles of about 1–3 μm were randomly distributed in the grain boundaries and matrix. Additionally, the gas-atomized powder has a more regular shape than the water-atomized 17-4PH powder. Therefore, the gas-atomised powder results in more regular pores. These regular pores reduce the oxidation rate during the sintering process because they reduce the amount of exposed surface area [68].

Furthermore, several critical oxides in austenitic stainless steels were residues from the water atomization process: Cr_2O_3, MoO_3, and SiO_2 [6]. Cr_2O_3 has high stability and is challenging to reduce, while Mo and Si must be removed before or during the sintering process. Moreover, the mechanical properties of stainless-steel parts can be improved by reducing oxides. For example,

it was found that the mechanical properties of MIM 17-4PH parts made from gas-atomized powder were improved compared with MIM 17-4PH parts made from water-atomized powder, mainly due to the lower Si, O, and SiO_2 contents in the case of gas-atomized 17-4PH powder [29].

2.3 Selective laser melting (SLM)

SLM is an additive manufacturing technique that falls under the powder bed fusion category of 3D printing methods, capable of producing nearly fully dense metal parts from pre-alloyed materials such as 17-4 PH, AlSi12, and Ti6Al4V, as well as other materials like Co-based and Cu-based alloys [69], [70]. SLM can achieve near-net-shaped components without the need for post-processing treatments [70], [71], [72]. The most common applications of SLM are found in the automotive and aerospace industries, where it enables the production of complex components that are otherwise challenging to create using conventional methods [70], [71], [72], [73]. When it comes to producing mono-material 17-4 PH, the SLM method is particularly suitable, as this pre-alloyed material boasts a wide range of applications due to its high mechanical properties and excellent corrosion resistance, with an operating temperature below 300 °C [70], [71], [73], [74], [75], [76]. SLM operates similarly to other welding processes, utilizing a layer-wise consolidation approach [77]. A thin layer of powder is deposited over a substrate plate or on the previously deposited layer, and a laser beam scans the powder particles selectively, melting and fusing them according to the CAD data [69], [70], [73]. After scanning a layer, the build cylinder moves down one step—typically between 30 and 100 µm—and the next powder layer is applied over the previous one using a powder coater mechanism. Once all layers have been deposited, the unscanned powder can be removed, allowing the produced part to be extracted from the machine. The entire process occurs within a closed chamber, typically filled with an inert gas like N_2 or Ar, depending on the reactivity of the metal powder used [78]. Complex physics are involved, including the absorption, transmission, and reflection of laser energy; adhesion of micron-scale particles; rapid melting and solidification; molten metal flow; metal evaporation; and microstructural evolution [71], [79], [80].

2.3.1 Scanning strategy

The microstructure of SLM-built parts is influenced by the cooling rate and temperature gradients. Furthermore, the scanning strategy significantly affects the densification properties of 3D 17-4PH parts due to heat-affected zones and their impact on microstructural defects such

as porosity. Choosing an appropriate scanning strategy can minimize residual stresses, pores, and enhance surface quality [81]. It has also been reported that samples fabricated via SLM were not entirely martensitic, with the presence of retained austenite observed [82]. A study investigating the effect of laser scan patterns revealed that using a scan pattern perpendicular to the loading direction resulted in 25% retained austenite, whereas employing a scan pattern parallel to the loading direction produced twice the amount of retained austenite for the 17-4 stainless steel [83]. The effect of altering the scanning angle from normal at 90° to normal at 45° on the microstructural properties was partially investigated [75]. The results indicated that the 3D 17-4PH samples scanned at 45° exhibited greater hardness than those scanned at 90°, attributed to the larger grain size of α/ά regions and a lower austenite volume fraction in the 45° samples. Conversely, it was noted in [81] that changing the hatching style of the stripe scanning strategy resulted in fully dense and homogeneous 316L stainless-steel parts, where the tracks of adjacent layers were offset by half the hatching distance and rotated 90° every two layers. Another study explored the impact of the scan strategy on 17-4PH in[84]. It was demonstrated that samples processed using the double scan strategy achieved superior results regarding relative density.

During the printing of SLM 17-4PH parts, three distinct strategies (normal with 45° and -45°, concentric from the outside to the centre of the sample, and hexagon strategy) were investigated [81]. Compared to other strategies, the hexagonally scanned samples demonstrated superior densification. The effect of scanning angles of 45° and -45°, as well as single and double scanning for the same layer, on the physical and mechanical properties of SLM parts printed from gas-atomised 17-4PH powder were examined in [84]. Compared to single scanned samples (0.14%), the results demonstrated that double scanned samples had pores that were 0.2% smaller. The hexagon scanning strategy was implemented with variable defocus adjustments of -1 and +1 mm for each printed layer, such that the sixth layer will have the same defocus as the first. The results revealed no significant microstructural differences. Except for the minor difference in hardness between samples with different defocusing (274-306 HV) [85]. Thus, choosing the appropriate scan strategy and scan angle is complicated due to the direct influence of these parameters on the thermal history of the printed stainless-steel parts, which affects the phases and their volume fractions.

2.3.2 Energy density

The effects of processing parameters on the characteristics of SLM 17-4PH materials have been investigated in several studies. The results indicate a strong correlation between energy density, porosity, and microstructure [86]. Various processing parameters have been established and utilised in experiments, further demonstrating the relationship between energy input, porosity levels, and mechanical properties [87]. Process parameters such as scanning speed, laser power, powder layer thickness, and hatch distance can be selected[8]. The combined effect of these parameters can be calculated through the heat input generated by the laser source, which can be quantified by the energy density parameter E, as shown in Equation (1):

$$E = \frac{\rho}{\nu . h . t} \left[\frac{\mathrm{J}}{mm^3}\right] \qquad (1)$$

Where ρ laser power (W) is, ν is laser speed (mm/s), h is hatching distance (μm), and t is layer thickness (μm).

Selecting laser power versus speed significantly influences porosity; high speed should be applied during high power to minimize porosity [88]. Laser speed, layer thickness, and hatch distance at a fixed laser power of 200 W have been studied in the [72]. The results indicate a noticeable loss of density with an increase in hatch distance at higher laser speeds (v ≥ 80 m/min). The highest density recorded was 7.858 g/cm³ (the theoretical density in this work was not specified), achieved using a laser speed of 30 m/min and a hatch distance of 110 mm, along with a layer thickness of 20 μm. Increasing the layer thickness to 40 μm reduced the density to 7.72 g/cm³. Additionally, increasing the scan speed from 10 to 30 m/min raised the density from 7.65 to 7.858 g/cm³, respectively, with a layer thickness of 20 μm. Different SLM parameters were employed in the [70]. The results showed that the highest hardness value observed was 319 HV, with an ultimate compressive strength of 1132 MPa, corresponding to 255 W laser power, a 45° build orientation, a 40 μm layer thickness, and a -6 mm defocus distance. The lowest value was 281 HV, with an ultimate compressive strength of 1076 MPa, corresponding to the same parameters except for a 35 μm layer thickness and a -1 mm defocus distance. This difference in HV was attributed to the volume fraction of martensite and austenite; higher martensite content leads to increased hardness.

2.3.3 Building orientation

The effect of build orientation (0°, 45°, 90°) on mechanical properties and porosity formation was investigated in the [71], using SLM parameters of a laser speed of 800 mm/s and a layer thickness of 30 μm at 200 W laser power, with the hatch distance set to 100 μm. The results indicated that tensile strength was highest at 0° at 958 MPa, surpassing the values at 45° and 90°, which were 743 and 614 MPa, respectively. Porosity analysis confirmed that at 90°, three types of porosities were present: gas-entrapped pores, keyhole pores, and specifically, the crescent type, which contained unmelted powders.

2.4 Heat treatment

Heat treatment is the postprocessing of a manufactured metal part with the intention to modify properties, such as strength, ductility, and hardness, by controlling the microstructure and achieving the desired phases, grain growth, and precipitation. For instance, after annealing a CoCrFeMnNi alloy, the strain increased by 5% [89]. In addition, ferrite dissolution reduced the hardness of 316 stainless steel by 25% when solution treated at 1050 °C [90]. Thus, many studies investigated different conditions for sintered parts produced from water- and gas-atomised 17-4PH using PSM, MIM, and FDM [23], [29], [91]. However, each experiment used a different atmosphere, hold time, heating rate, and cooling rate. Solution annealing, H900 (ageing at 482 °C), and H1100 (ageing at 552 °C) made up most of these conditions. The volume fraction of δ-ferrite increased after the solution heat treatment. Therefore, this condition is appropriate for a reasonable ductility requirement. An increase in strength and hardness and a decrease in ductility are noted after applying H900, which formed Cu precipitates (observed by optical microscope) and less δ-ferrite compared to the as-sintered parts. Thus, δ-ferrite impacts tensile strength and ductility[4]. Increasing the volume fraction of ferrite in low-carbon steel leads to a further rise in ductility and a loss in tensile strength due to the elasticity [92]. However, an accumulation of δ-ferrite and larger Cu precipitates occurred during H1100. Different solution temperatures (940 °C, 990 °C, 1040 °C, 1090 °C, and 1140 °C for two hours) followed by ageing at 480 °C for four hours have been applied for SLM 17-4PH parts[74]. The results indicate that the increasing solution heat treatment temperatures decreased the Ms (martensite transforming temperature), increased retained austenite, increased the δ-ferrite, and decreased the hardness. The highest hardness and strength were obtained at the following heat treatment condition: solutioning at 1040 °C for two hours and ageing at 480 °C for four hours. This was due to the

formation of a complete martensite structure. Furthermore, a study investigated the effect of applying different heat treatment conditions on enhancing the mechanical properties of laser powder bed fusion 17-4PH parts. The best results obtained after applying the following conditions: normalising (1200 °C, 4-hours) + solutioning (1060 °C, 1-hour) + ageing (482 °C, 4-hours) [93]. However, Table 3 summarises the mechanical properties of PSM 17-4PH parts as a result of the heat treatment conditions. The effect of heat treatment conditions on the 17-4PH additive manufactured (such as laser powder bed fusion and SLM) parts is also included in Table 3. However, these results indicate that applying ageing heat treatment enhances the strength and hardness properties of the 17-4PH parts regardless of the effect of the manufacturing conditions (especially PSM and SLM).

Furthermore, the atomisation medium has an effect on the final structure of the heat-treated 17-4PH parts. An elemental map was used to examine the black spots (not the big pores), which were distributed in the microstructure of the water-atomised MIM 17-4PH parts[29]. The results revealed the presence of SiO_2 due to the presence of Si near oxygen sites, in addition to Cu precipitates. After annealing, H900, and H1100 heat treatments, it can be deduced that the gas-atomised MIM 17-4PH parts had more δ-ferrite and less SiO_2 than the water-atomised parts.

Table 3. The mechanical properties of various stainless-steel parts produced by PSM are compared to those made using other processing methods.

17-4PH Method	Heat-Treatment	Hardness	Y.S., MPa	UTS, MPa	Ref.
PSM	Aging, 538 °C, 1-hour.	HV= 237	688	819	[25]
PSM	Annealing at 1040 °C + aging at 480 °C	HV10= 332	--	1100	[24]
PSM	As sintered	HRB= 89		869	[23]
	Solutioned at 1065 °C, 1.5-hours, in	HRB= 90		816	
	Aging at 482 °C, 2-hours	HRB= 98		1136	
LPBF	As-printed	--	--	1126 ± 2	[94]
	Aging at 670 °C for 4-hours	--	--	1563 ± 13	
LPBF	As-printed	--	535	~1090	[93]
	Normalizing at 1200 °C, Solutioned at1060 °C, 1-hour + aging at 482 °C, 4-hours	--	1264	~1390	
SLM	As-printed	HV0.5= 365	--	~ 1110	[74]
	Solutioned at 1040 °C, and aging at 480 °C for 4-hours.	HV0.5= 381 to 392	--	1180	
wrought	H1150 (620 C,4-hours)	HV1= 340	914 ±7	1017 ± 2	[95]
wrought	H925 (496 °C, 4-h)	--	~1206	~1380	[96]
	H1100 (594 °C, 4-h, air cooling)	--	~965	~1103	
wrought	H900	--		1500	[27]
wrought	aging 430 °C, 4-h	455		--	[97]
	aging 500°C, 4-h	--	1200	1300	
Cast	aging at 482 °C	--	1130	1255	[98]

2.5 Research aims and objective

Earlier studies aimed to enhance the sinter density of 17-4PH parts produced by PSM. The maximum green and sinter densities achieved were 80.67% and approximately 93%, respectively. The high porosity of PSM parts made from 17-4PH remains a significant concern. Because steels with poor density exhibit poor mechanical properties [3]. The existing literature reveals a lack of sufficient studies focused on enhancing the inadequate densification of PSM 17-4PH parts, as the high porosity of these pats remains the primary obstacle to their application. Additionally, the critical PSM parameters encompass cold pressing, sintering temperatures, and sintering durations, all of which significantly influence the density and the physical and mechanical properties of PSM 17-4PH parts. Therefore, this dissertation work presents a

thorough analysis of the aforementioned parameters. In addition, different furnaces with different heating resources (electrical and induction) are employed to produce PSM 17-4PH parts.

Additionally, literature has reported no studies comparing the physical-mechanical characteristics of various methods for producing 17-4PH parts. The market still favors PSM parts over newer technologies like SLM parts, primarily due to the cost-effectiveness of PSM stainless steel components. However, in terms of physical-mechanical properties, SLM 17-4PH parts are preferred over PSM 17-4PH parts because of the lower density of the latter. This study utilised a heat-treatment process as a necessary step prior to export for actual service conditions, aiming to compare the physical and mechanical properties of 17-4PH parts produced by various techniques, primarily PSM and SLM.

2.6 Scientific questions

The following points outline the scientific questions that could not be addressed previously according to the reported literature:

1) 760 MPa was the maximum cold pressing used to produce PSM 17-4PH parts. Applying a higher cold pressing than what was used in the literature needs to be investigated. The relationships between high cold pressing and the hardness of different stainless-steel powders also need to be established to validate the effect of high cold pressing. Additionally, gas-atomised powder had not been previously utilised in the production of PSM 17-4PH parts. There is an interesting scientific question regarding whether the use of gas-atomised powder instead of water-atomised powder is applicable.
2) The literature indicates that using a sintering temperature below 1220°C for producing PSM 17-4PH parts is not advisable due to the risk of incomplete sintering. At the same time, a lower sintering temperature decreases the shrinkage value, which is beneficial for the technical manufacturers as it preserves the product dimensions. Therefore, how can high cold pressing improve the application of the low sintering temperature of 1200°C in the production of stainless-steel PSM parts with satisfactory physical-mechanical properties?
3) The average smallest particle size of the 17-4PH powder reported in the literature is 45 µm. Therefore, clarifying how a reduction in particle size affects the porosity of the PSM 17-4PH parts appears to address a gap. Furthermore, the literature indicates that there

has been no prior use of 17-4PH powder from the 3D printing process to produce PSM 17-4PH parts. Consequently, an open question remains regarding the recyclability of this powder.

4) No study has yet examined the impact of using induction heating sources in the sintering process of 17-4PH parts, along with their densification and mechanical properties. Therefore, how does the induction heating source reduce the required sintering time and enhance the physical-mechanical characteristics of INDS 17-4PH samples?
5) Avoiding scan voids is a critical issue due to its direct connection to SLM machine-type standards. This problem affects the density reduction (and lower mechanical properties) of SLM 17-4PH samples. How can we assess various parameters (energy density, scanning strategy, and fixed contour value) during 3D printing using the SLM method to eliminate actual porosity (subsurface pores)? Which approach can achieve the highest density and improve strength properties?
6) Comparing the physical-mechanical properties of 17-4PH samples produced by various methods poses a significant challenge and has not been previously explored. However, applying a heat-treatment condition (H900) can aid in the comparison process. Moreover, heat treatment is a primary procedure for the stainless-steel part before its deployment. Consequently, how would the implementation of H900 influence the physical-mechanical properties of 17-4PH produced using various techniques: conventional sintering, induction sintering, and additive manufacturing (via SLM)? Furthermore, is the comparative approach relevant?

3. CHAPTER 3: Materials and methods

3.1 Stainless-steel powders used in this research work

The following list presents the stainless-steel materials utilised in this dissertation work:

1- Original powder was the as-received Oerlikon gas-atomised 17-4PH powder, exhibiting an apparent density of 4.0 g/cm³. This powder had a particle size distribution ranging from 15 to 45 µm. The 17-4PH grade is classified as a martensitic stainless-steel powder.

2- The recycled 17-4PH powder was collected from the chamber of an XY-type selective laser melting (SLM) machine. It was reused for multiple printings (approximately 10 times) of 3D 17-4PH components.

3.2 Characterization methods for raw materials

SEM and EDS analyses were performed using ZEISS (EVO MA10) equipment. These analyses aimed to assess the morphology and composition of original and recycled 17-4PH powders and to investigate the microstructure of the particles' sectional surfaces.

The chemical composition of both the original and recycled powders was analysed using ICP-OES. This analysis was performed because predicting carbon content through EDS analysis proved to be challenging.

3.3 Manufacturing tools and equipment

An INSTRON 5982, capable of applying a maximum load of 10 tonnes, was utilised to provide the required cold pressing for producing green samples of stainless-steel powders. The cold pressing machine and the die for the green samples production are illustrated in Figure 5.

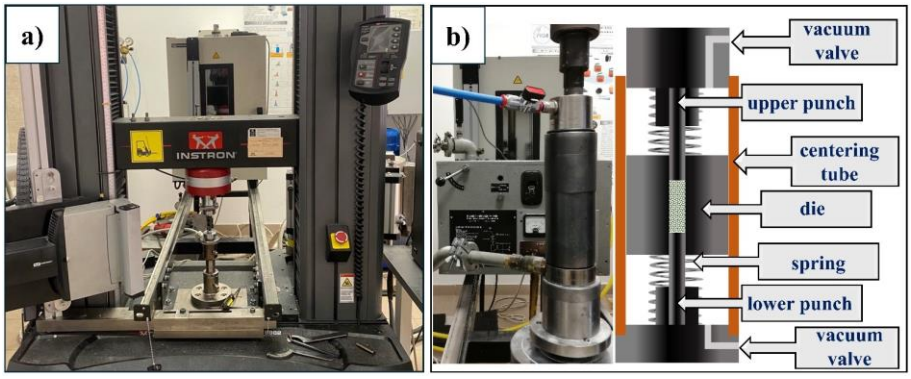

Figure 5. Depicts the a) universal tensile machine, and b) the die used for green samples

The conventional sintering at low temperatures (up to 1200 °C) was conducted in a vertical tube sintering furnace (model: INSTRON, S.F.-16). Conversely, a ThermConsept furnace was

employed to produce heat-treated 17-4PH samples at the conventional sintering temperature of 1300 °C. This type of furnace is designed to achieve a maximum temperature of 1600 °C.
The employed induction sintering system is illustrated in Figure 6. An Iew GmbH induction furnace was utilised, applying approximately 10% of the maximum 0.5 kW of electric power at a frequency of 100 kHz.

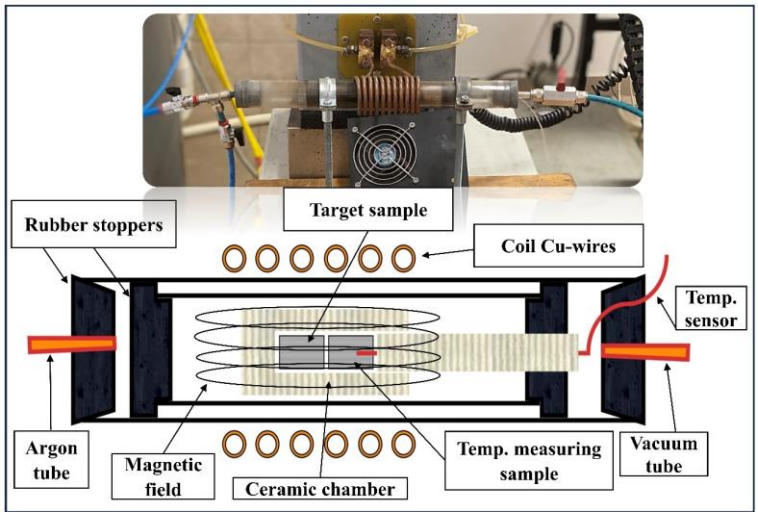

Figure 6. The induction sintering system (the set up was made by Dr. Tamas Miko).

A Creator SLM machine was utilized for printing the SLM 17-4PH samples. This machine employs a Yb (fiber) laser with a power of 250 W. The laser wavelength is 1070 nm, with a detail accuracy of x=80 µm, y=80 µm, and z=20 µm. The platform dimensions are 100 mm in diameter and 110 mm in height. The printing mechanism is described in section 2.3. However, Figure 7 illustrates the Creator SLM machine along with its chamber and provides an example of printing 3D 17-4PH samples.

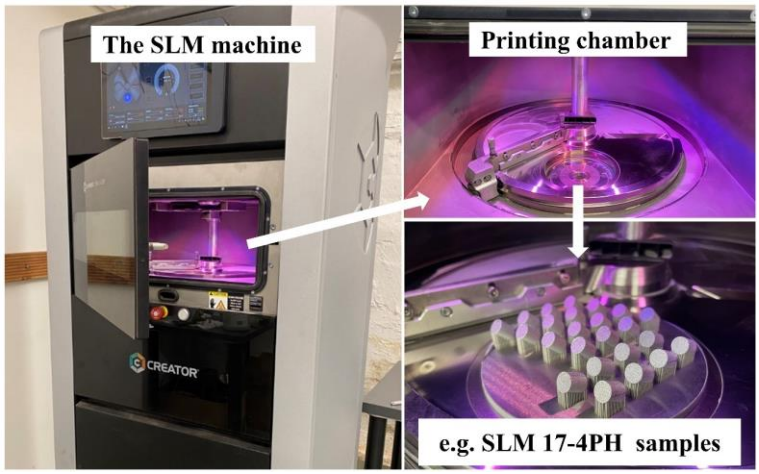

Figure 7. The creator SLM machine for printing SLM 17-4PH samples

3.4 Preparation procedures

3.4.1 Preparation samples for different cold pressing and low conventional temperatures

The original 17-4PH powder was sieved to a smaller particle size of 15–32 µm using XY sieving equipment. The reduction in particle size was performed to enhance the density and, consequently, the mechanical properties of stainless-steel powdered materials, as noted in a recently published review paper [13]. Cylindrical samples with diameters of 8.3 mm and heights of 7–8 mm (3 g was used as a powder charge) were prepared through a range of cold pressing (700 to 1600 MPa), various sintering times (1 to 7 hours), and different sintering temperatures (600 to 1200 °C) in these investigations. The manufacturing procedures of the DCTT samples are illustrated in Figure 8. However, the surface of the die wall was lubricated with graphite (KONTAKT CHEMIE 33) to reduce friction during compaction and ejection. Cold pressing was performed under vacuum to minimise gas adhesion in the closed pores. The vacuum level was 10^{-3} mbar during cold pressing and sintering. The furnace environment plays a critical role in managing oxide production. The presence of oxygen in stainless steel products is due to the strong affinity of carbon for oxygen. As a result, using vacuum and argon sintering atmospheres effectively eliminated oxides through reduction processes and reduced porosity as well [25]. The heating rate, sintering temperature, dwelling time, and cooling rate were 10 °C/min, 1200 °C, 60 min, 10 °C/min, respectively. For verification, three samples were produced and evaluated in parallel for each manufactured condition.

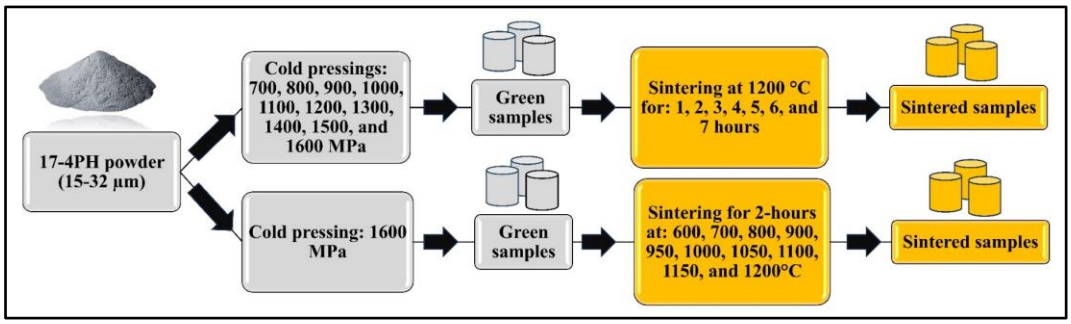

Figure 8. The manufacturing procedures for DCTT 17-4PH samples.

These broad ranges of values for cold pressing, sintering times, and sintering temperatures were selected to ensure thorough and comprehensive analyses. Moreover, extending the sintering time to seven hours has been previously employed to enhance the density of an austenitic stainless-steel powdered material [53]. Furthermore, the seven hours of sintering in this study account for 14% of the total sintering time for the stainless-steel MIM parts, which can take up to 50 hours [4], [13].

3.4.2 Preparation recycled 17-4PH samples with different powder particle size

Both O and R 17-4PH powders were sieved (using an XY sieving equipment) into three distinct groups: 15–32, 32–45, and 45–63 µm. The diagram illustrating the manufacturing steps is shown in Figure 9. However, the dimensions and manufacturing procedures for the original and recycled 17-4PH samples were similar to those outlined in section (3.4.1).

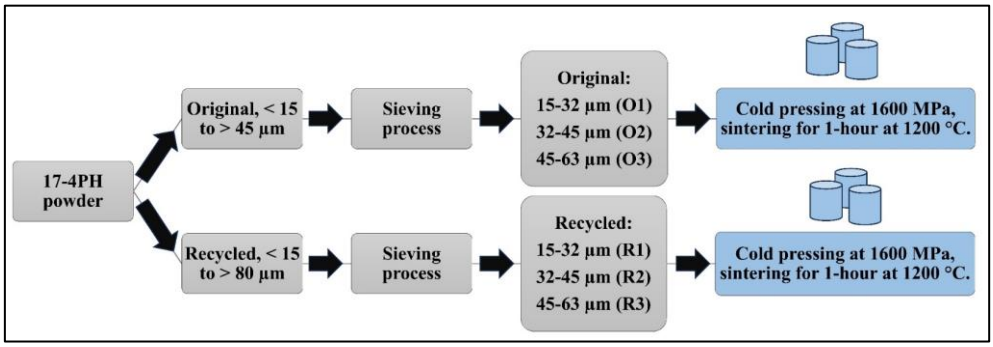

Figure 9. Illustrates the original and recycled 17-4PH samples manufacturing steps

3.4.3 Preparation procedures of induction sintered original 17-4PH samples

The investigated powder was the original 17-4PH, exhibiting a particle size distribution ranging from <15 to >45 µm. Cylindrical samples, approximately 8.3 mm in diameter and 10.3 mm in height, were prepared. The cold pressing procedures for producing green samples were similar

to those described in section (3.4.1), except that the green samples were held for 2 minutes before releasing the load. INDS was employed at various sintering temperatures (1200 and 1300 °C) and sintering durations (15 to 120 min). The manufacturing procedures are detailed in Figure 10.

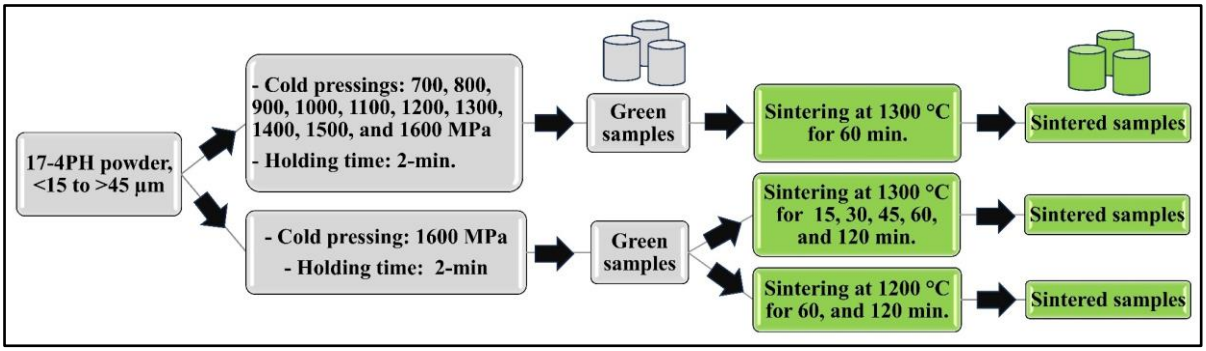

Figure 10. Manufacturing procedures of INDS 17-4PH samples.

The description of the sintering process was as follows: inserting the green samples into a ceramic tube chamber; placing the ceramic tube inside a heat-resistant glass tube; turning on the vacuum for five minutes (to remove the air from the furnace glass chamber); turning off the vacuum and turning on the argon gas to fill the glass chamber (a balloon was used to ensure the presence of argon during the sintering process); applying different sintering temperatures and times. Furthermore, vacuum and argon sintering atmospheres were effective for 17-4PH parts to remove oxygen and consequently reduce porosity [13]. Finally, the heating rate and cooling rate were 100 and 60 °C/min, respectively.

3.4.4 Manufacturing procedures of SLM original 17-4PH samples

The employed powder was the recycled 17-4PH. This powder was utilised multiple times to print 3D samples, ranging from 1 to 10 iterations. It was sieved before each new printing process with a mesh size of 140 to eliminate welded larger powder particles. The manufacturing method employed is SLM. The SLM process comprises two distinct manufacturing setups designated as 1SLM and 2SLM, which are detailed in Table 4.

Two different SLM setups were employed, including two energy density configurations and two scan strategies: normal and zigzag, with a 45-degree rotation for each subsequent printing layer. The unconnected zigzag scanning strategy was utilised, indicating that the forward laser path halts at the end before reversing and starting anew. The normal and zigzag strategies are illustrated in Figure 11. By rotating each layer individually, it is possible to minimize overlap

between layers and vary the thermal gradient as much as possible [99]. This, in turn, helps further reduce residual stress. However, the selection of these three SLM setups was based on a thorough analysis of the literature to achieve optimal densification alongside mechanical properties. Nevertheless, cylindrical samples with an approximate diameter of 8 mm and height of 10 mm were manufactured for both two setups.

Table 4. Represents the SLM method designed setups.

Samples code / Parameters	1SLM	2SLM
Laser Power, W	107	168
Laser Speed S/mm	1200	1000
Layer thickness, µm	25	35
Hatch distance	100	
Energy Density, J/mm^2	36	48
Scan Strategy	Normal with fixed 45°	Zigzag with 45° rotation
Contour	2	
Sample Orientation	45°	
Space between contour and hatch	0	
Beam diameter	40 µm	
Shield gas	nitrogen	

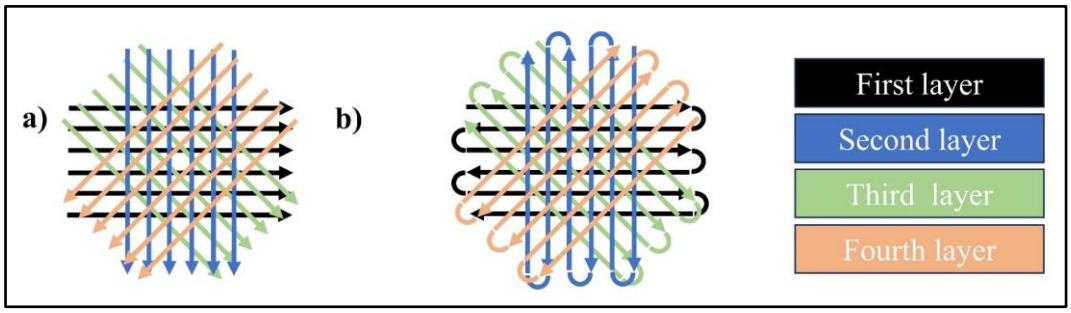

Figure 11. Examples of the 45° rotating of a) normal, and b) zigzag scanning strategies.

3.4.5 Heat-treatment procedures for different-methods 17-4PH samples

The H900 treatment was applied to the 17-4PH samples produced using conventional sintering, induction sintering (cold pressed at 1600 MPa, held under cold pressing for 2 minutes, and sintered at 1300 °C for 60 minutes), and selective laser melting methods (sample code 2SLM). The selection of samples for the H900 application was based on the highest achieved density and strength (see sections 4.5 and 4.6).

However, the aim was to compare the physical-mechanical properties of these different manufacturing techniques. This heat-treatment condition was implemented to enhance the strength of the 17-4PH materials. The H900 procedure was previously detailed in[100]. This procedure involves solution heat treatment (annealing) at 1038 °C for 30 minutes in an argon atmosphere, followed by quenching in water. The annealed samples were then aged at 480 °C for 60 minutes in an argon atmosphere. The heating rate during the annealing and aging treatments was 10 °C/min.

For the conventional sintering samples, new PSM samples were manufactured at a conventional sintering temperature of 1300 °C, indicated by CPCS 17-4PH samples. The manufacturing procedure for these samples was similar to that outlined in section (3.4.1), except that the conventional sintering process was conducted using a ThermConsept furnace. Additionally, the sintering procedure involved encapsulating the cold-pressed samples into a stainless-steel tube, which was subsequently filled with argon gas. The tube was then sealed by welding and inserted into the sintering furnace along with the samples. The heating rate was set at 3 min/°C, while the cooling rate was 10 min/°C. The samples were left in the furnace to cool completely. Figure 12 illustrates the stainless-steel tube containing the sintered CPCS 17-4PH samples. However, the heat-treated 17-4PH samples produced by conventional sintering, induction sintering, and selective laser melting methods are coded as shown in Table 5.

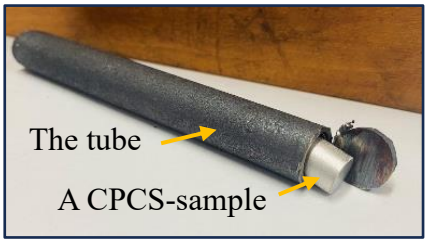

Figure 12. Extracting the sintered 17-4PH samples from a stainless-steel tube

Table 5. Coding of the heat treated 17-4PH samples produced by PSM, INDS, and SLM methods.

Method	Conventional sintering	Induction sintering	Selective laser melting
Code	HT-CPCS	HT-INDS	HT-SLM

3.5 Characterization of manufactured samples

Due to the vast number of produced samples, it is extremely challenging to study all of them. This research focuses on specific sample conditions. The investigations selected sample results

that encompass both the majority of ideal and poor outcomes. This research aims to perform a comprehensive comparison of the produced samples.

3.5.1 Physical characteristics investigations

Green densification measurements were conducted using the dimensional method; the theoretical densities were 7.75 g/cm^3 for 17-4PH. Sintering densification was measured using the Archimedes method according to ASTM standard B962-13 [86].

Furthermore, regression analysis using Excel was conducted on the DCTT 17-4PH samples data. The analyses encompass linear and polynomial regression data utilised to evaluate the alignment of the estimated densification model with the actual outcomes. The evaluations were performed to forecast the impact of traditional powder metallurgy parameters on the densification characteristics of 17-4PH materials for future studies as well.

To understand the thermal behaviour of the original PSM 17-4PH samples, a DSC test was carried out. This test was performed using an NETZSCH (STA 449 F3 Jupiter) thermal analysis equipment from room temperature to 1200 °C, held for 10 minutes at 1200 °C, and then cooled back to room temperature.

To understand the thermal behavior of the original PSM 17-4PH samples, a DSC test was conducted. This test was performed using NETZSCH (STA 449 F3 Jupiter) thermal analysis equipment from room temperature to 1200 °C, held for 10 minutes at 1200 °C, and then cooled back to room temperature.

The phase composition of PSM 17-4PH was characterized by XRD using a D8 Advance diffractometer (Bruker, Germany) in Bragg-Brentano geometry. The XRD diffractograms were obtained using CuKα radiation (k = 1.5418 Å) over a scanning range of 2θ from 20 to 120 degrees, with a resolution of 0.007 per step and a step time of 14 seconds (equivalent for a scintillation detector). However, EBSD analysis was employed as an alternative to XRD analysis. The EBSD analysis was conducted using an SEM machine, Helios G4 PFIB CXe with Thermo Scientific equipment, utilising the EDS tool from the HIKARI SERIES, Model No: 9424.079.60360STBC.

The cross-sections of the manufactured samples were metallographically polished by Schmitz Metallography (Germany). A ZEISS-AXIO imager was utilized for optical microscopic analysis. Additionally, ImageJ software was employed for analysing cross-sectioned microstructures, including measurements of grain size, porosity, and pore morphology. The

SEM and EDS analyses were conducted using ZEISS (EVO MA10) and Helios G4 PFIB CXe-thermoscientific equipment. The Helios G4 PFIB CXe-thermoscientific, equipped with an AMETEK EDS model: -0.09/242478, was also utilised for the FIB-SEM analysis. These analyses were used to examine the microstructures. They were performed on the longitudinal cross-sections of the samples after etching for to 20 seconds. Fry's reagent (10 g $CuCl_2$ + 60 ml H_2O + 80 ml HCl + 50 ml C_2H_5OH) was used for etching 17-4PH samples.

3.5.2 Mechanical characteristics investigations

The Vickers hardness of the cross-sectioned 17-4PH samples was measured using a Vickers hardness tester (Georg Reicherter, Germany). HV tests were conducted with a 10 kg load, and the average HV of three sintered samples, using nine different indenters for each, was calculated, excluding the highest and lowest values. Furthermore, the cross-sectional HV measurements were compared with surface HV measurements for selected 17-4PH samples.

To assess the mechanical properties of the manufactured samples in this research, the compressive strength was examined using the same cold pressing machine (the universal tensile testing equipment) at room temperature, with a maximum load of 10 tons. This analysis was conducted on samples of DCTT 17-4PH, original and recycled PSM, INDS 17-4PH, and SLM 17-4PH.

4. CHAPTER 4: Results and discussion

4.1 Raw powders analyses

These results include analyses of both original and recycled 17-4PH powders used in this dissertation, covering SEM, EDS, sieve fraction, and chemical compositions.

4.1.1 SEM, EDS, and sieving fraction analyses

The morphologies and size distributions of the original and recycled powder particles are presented in Figure 13. Both the original and recycled powder particles exhibit spherical morphologies, although the recycled powder displays welded particles due to the heating effect that fused the particles together during the SLM printing processes. Consequently, the recycled powder has larger percentages of large particle size distributions in the 63–80 µm and over 80 µm ranges compared to the original powder.

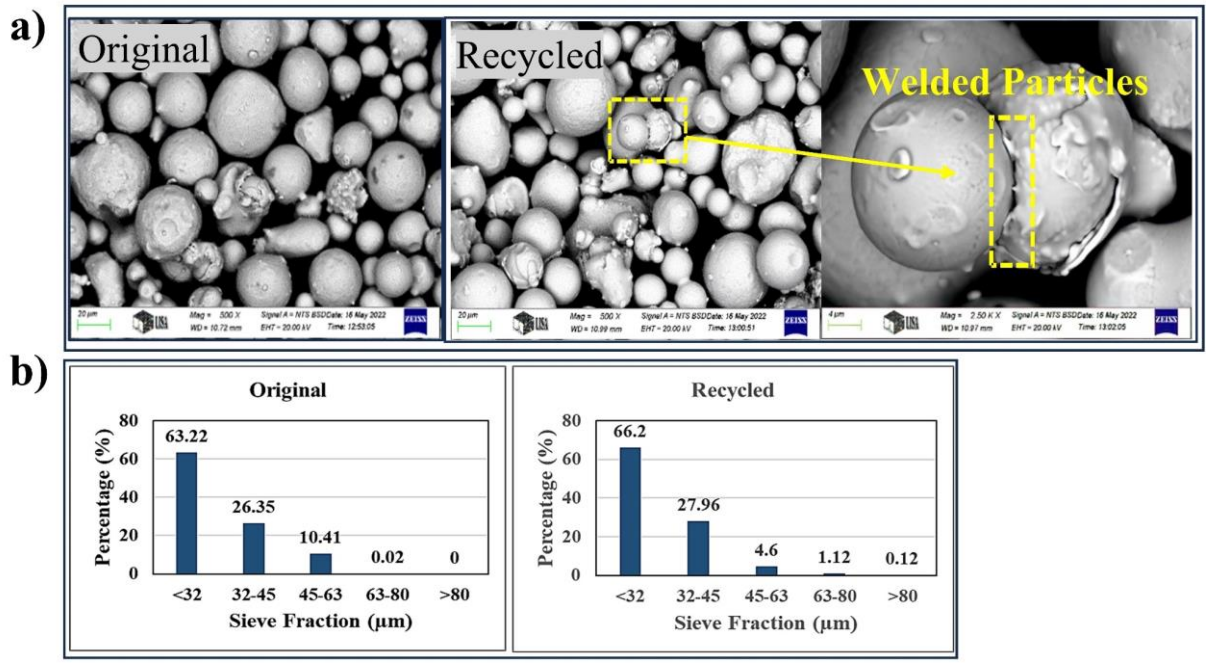

Figure 13. Represents a) the SEM morphology, and b) the sieve fractions results of both original and recycled 17-4PH powders.

The SEM morphologies of the etched original and recycled cut 17-4PH particle powders are displayed in Figure 14. This confirms that both powders exhibit similar morphologies. The elevated temperatures associated with the SLM printing processes affect the powder particle morphologies, resulting in 17-4PH powder particles with distorted grains.

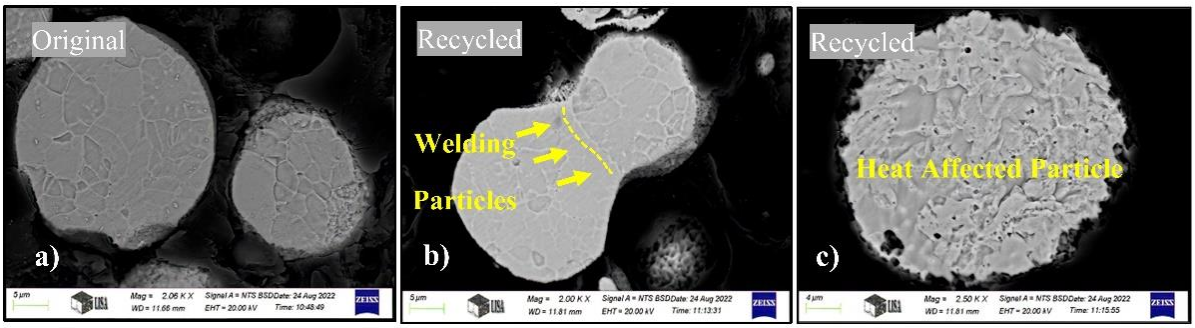

Figure 14. The SEM images showing the morphology of different etched particles of a) original, b) welded recycled-particles, and c) distorted recycled particles powders.

4.1.2 Chemical composition analysis of 17-4PH powders

The results of the ICP-OES are presented in Table 6. The results indicate a very low C % of the original 17-4PH powder. Additionally, it indicates that the recycled powder has a comparable chemical composition to that of the original powder. Furthermore, the carbon content of the original powder was 0.01 wt.%, which is lower than that of the recycled powder (0.02 wt.%). The source of this carbon (residual carbon) increment content mostly as contaminants after several reusing times for 3D printing processes.

Table 6. The ICP-OES of the original and recycled 17-4PH powders.

Element, Wt.%	C	Cr	Cu	Ni	Nb	Ta	Fe
Original 17-4PH powder	0.01	17.1	3.03	4.46	0.27	< 0,01	Bal.
Recycled 17-4PH powder	0.02	17.4	3.18	4.73	0.29	< 0,01	Bal.

4.2 Results of optimisation conventional sintering conditions

The current dissertation will comprehensively examine the essential PSM parameters, encompassing a wide range of cold pressing pressures, as well as different sintering temperatures and times. The objective is to attain optimal densification characteristics while ensuring acceptable strength properties. A maximum cold pressing pressure of 1600 MPa will be applied to improve the relative green density. Furthermore, a maximum sintering temperature of 1200 °C will be utilised due to its cost-effectiveness and capacity to achieve minimal shrinkage, as preferred by manufacturers.

4.2.1 Dimensional and Archimedes density measurements

The results of the relative green densities under various cold pressings of DCTT 17-4PH samples are shown in Figure 15. It is evident that the relative green density increased from 80.20 ± 0.28 to 91.76 ± 0.18 % as the cold pressing rose from 800 MPa to 1600 MPa, respectively. P. K.

Samal et al. utilised 760 MPa, which was the highest cold pressing reported in the literature, yielding a relative green density of 80.67 % for PSM 17-4PH [23]. An increase in cold pressing results in a higher green density of steel parts [13], [33], [36]. However, the DCTT 17-4PH samples were crushed at a cold pressing of 700 MPa Two factors contributed to the failure: the absence of a binder such as wax and the application of pressure that was comparatively lower (700 MPa) than what was required to induce sufficient plastic deformation and enhance the contact areas of the compacted particles in this high-hardness powder. The use of a binder was avoided to minimise the impact of organic compounds on the powder's chemical composition during the sintering process.

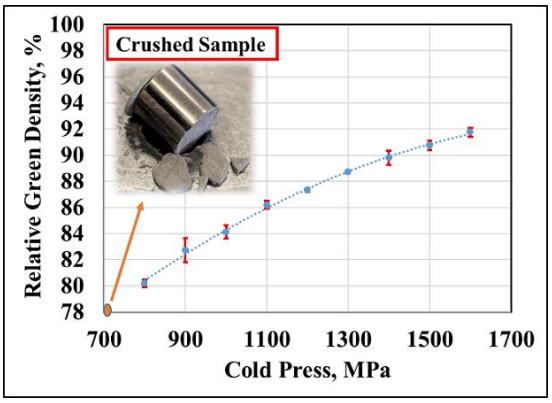

Figure 15. Various cold pressing versus relative green density of DCTT 17-4PH samples.

The results of the combined effects of cold pressing and sintering temperatures are illustrated in Figure 16. The actual and estimated findings indicate a proportional relationship between relative green and relative sinter densities. The linear regression equation (estimated model) shows that the intercept (relative sinter density) can be approximately equal to 93 when the sintering time is zero. Additionally, the slope between relative sinter density and sintering time is little, suggesting that sintering time has a slow influence on relative sinter density at a sintering temperature of 1200 °C. Moreover, the R^2 value, which calculates here the proportion of variation between relative sinter density and sintering time, is 0.98, very close to 1. This indicates that this estimation model effectively represents the actual relationship between relative sinter density and sintering time. However, the proportional relationship between relative green and sinter densities can be explained by the fact that increased cold pressing resulted in higher green densities and, consequently, elevated sinter densities in the DCTT 17-4PH samples. After two hours of sintering, the relative sinter density rose from 88.01 ± 0.45 to 95.65 ± 0.38 % as cold pressing increased from 800 to 1600 MPa, respectively. Furthermore,

extending the sintering time to seven hours resulted in a higher relative sinter density of 98.07 ± 0.4 % for DCTT 17-4PH samples cold pressed at 1600 MPa. Thus, the gaps between the relative sinter densities at two hours of sintering were larger than those observed after seven hours. Consequently, the relative sinter density of the DCTT 17-4PH samples analysed in this study (98 %) is significantly greater than the maximum value reported in previously published research, which was around 93 % [13]. The extended sintering time of seven hours facilitated the completion of the diffusion process, leading to an increase in the sinter densities of the DCTT 17-4PH samples.

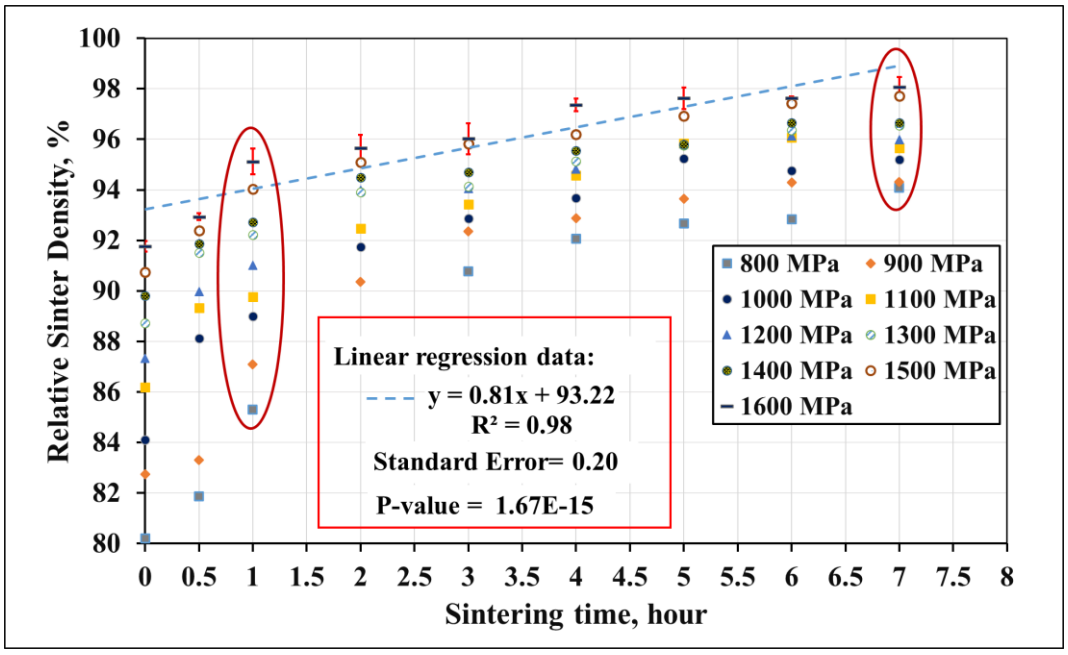

Figure 16. The impact of cold pressing and sintering time on the relative sinter densities of DCTT 17-4PH samples.

The impact of sintering temperatures on DCTT 17-4PH samples, which were cold pressed at 1600 MPa and sintered for two hours, is depicted in Figure 17. It demonstrates a semi-parabolic relationship between sintering temperature and relative sinter density. Consequently, the polynomial regression data yield a well-fitting equation with an R^2 value of 0.99. This indicates that the estimation model accurately represents the relationship between relative sinter density and relatively low sintering temperatures. However, the relative sinter densities increased from

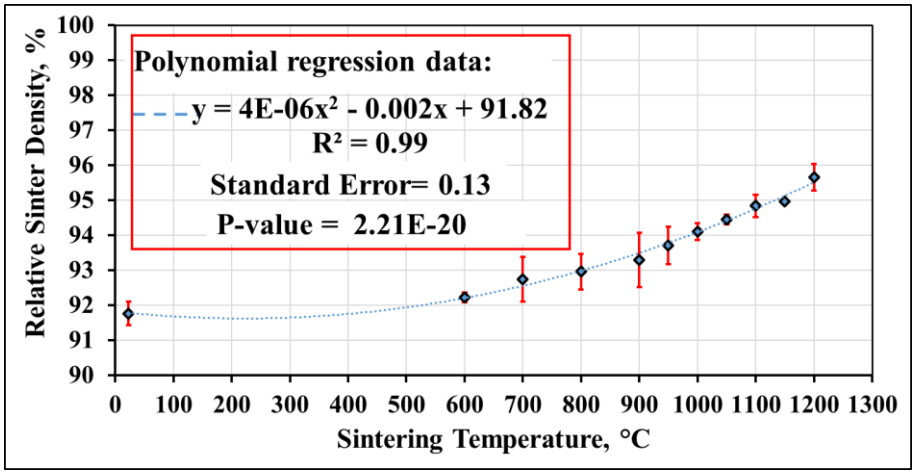

Figure 17. The effect of sintering temperature on the relative sinter densities of DCTT 17-4PH samples that were cold pressed at 1600 MPa and sintered for two hours.

92.22 ± 0.13 to 95.65 ± 0.44 % as sintering temperatures rose from 600 to 1200 °C. There are three basic steps during sintering: decreasing pores and bonding between particles, necking, and grain growth [13]. As sintering temperature and/or sintering time increase, these steps will occur freely to completion. In other words, the diffusion process will be sufficient after the grain growth step. Additionally, the phase transformation of the 17-4PH materials, which will be discussed in detail later, also affects density improvement. For example, the formation of δ - ferrite at elevated sintering temperatures [13]. As a result, increasing the sintering time or temperature enhances the densities of the PSM 17-4PH parts [13], [24], [25].

Employing a relatively low sintering temperature of 1200 °C to achieve a relative sinter density of 98% can be regarded as a significant accomplishment in the field of PSM 17-4PH materials when compared to existing literature. The highest relative sinter density for PSM 17-4PH materials was approximately 94% using a high sinter temperature of 1340 °C, as noted in a recently published review paper [13]. Furthermore, it is evident that the cost of a low-temperature furnace is less than that of higher temperatures, resulting in a reduction in the production cost of the final PSM 17-4PH part. Additionally, utilising a low sintering temperature reduces the volume shrinkage of the PSM 17-4PH parts. This enables the manufactured parts to maintain their shapes prior to sintering, thereby eliminating the need to increase powder weight for shrinkage loss and reducing post-processing costs. However, the impact of using a low sintering temperature will be discussed in detail later.

4.2.2 DCS and X-ray analyses

The thermal behaviour results of the DCTT 17-4PH samples are presented in Figure 18. The heating and cooling sections of the DSC curves are shown in red and black colours, respectively. The first exothermic arrest (490.5 °C) indicates the presence of Cu-precipitates in the matrix of the 17-4PH samples. The thermal endothermic arrest at 637.7 °C is due to the ferromagnetic to paramagnetic transformation of the martensite upon reaching the Curie temperature. However, the Curie temperatures in wrought and additively manufactured 17-4PH samples were 650 and 615 °C, respectively; this difference is attributed to the chemical composition and the effect of residual stresses[101]. The second endothermic thermal arrest is due to the formation of γ-phase, commencing at 908.4 °C. Upon cooling from 1200 °C, the exothermic martensitic phase transformation began at 117.9 °C and was completed before reaching room temperature. According to the phase diagram of the 17-4PH alloy, austenite transforms to martensite at 132 °C until the martensitic transformation is complete at 32 °C [13], [101]. Moreover, the peak of the Cu-precipitates is more pronounced due to the disorderly distribution of Cu in the matrix [102].

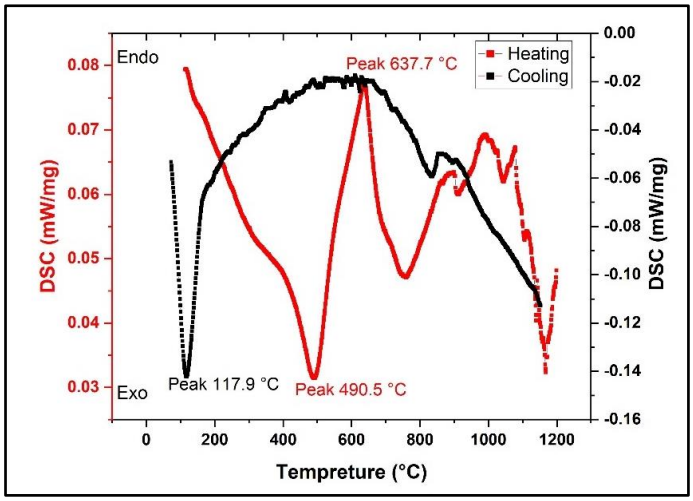

Figure 18. The DSC results of the thermal behavior of a DCTT 17-4PH sample cold pressed at 1600 MPa, and sintered at 1200 °C for two hours.

XRD and FIB-SEM analyses results are presented in Fig. 9. The diffractograms displayed BCC and FCC crystal structures, as shown in Figure 19 (a). The BCC structures correspond to the ferrite phase (α), while the FCC structures correspond to the γ-phase. Unfortunately, the XRD was unable to detect the body-centred tetragonal crystal structure (BCT), which corresponds to the martensitic phase (ά), due to the low carbon content of these materials. This low carbon content results in a very small distortion (c/a ratio) of the transformation lattice from BCC to

BCT structure, making it difficult to measure [103]. Additionally, several studies have indicated that it is impractical to distinguish between the BCT and BCC structures because of the extremely low carbon concentration in the 17-4PH powder [17], [104]. This implies that the BCT crystal structure, corresponding to the ά-phase, was very similar to the BCC crystal structure, which corresponds to the α-phase. The low carbon concentration results in a minimal distortion (c/a ratio) of the transformation lattice from BCC to BCT structure, making it difficult to measure [101]. Generally, the microstructure of the sintered 17-4PH materials consists of α, ά, and γ phases. The α phase forms in PSM 17-4PH materials at sintering temperatures below 1220 °C [13]. Furthermore, the ά phase was identified in the microstructure of the 17-4PH material sintered at a relatively low temperature of 1150 °C [51]. Therefore, it can be concluded that the ά and α phases are closely related in the microstructure of the DCTT 17-4PH samples. However, the FIB-SEM observation revealed two regions: bright and dark, corresponding to the α-region and ά/γ-region, respectively, as shown in Figure 19 (b). This is because the brighter areas in the SEM images typically indicate materials with higher atomic numbers or denser structures due to increased electron scattering; BCC crystal structures have lower atomic numbers than FCC crystal structures. Nevertheless, the formation potential of α, ά, and γ phases and their volume fractions depend on the chemical composition of the 17-4PH powder, the manufacturing atmosphere, the residual carbon, and the cooling rate[13], [105]. Furthermore, Figure 19 (c) presents the volume fraction of the α/ά and γ phases in the 17-4PH powder and its DCTT samples. It can be observed that the γ amounts are 4.95 % and 5.76 % for the 17-4PH powder and the DCTT 17-4PH samples sintered at 1200 °C for two hours, respectively. This indicates that the γ amount increased by approximately 1 % after sintering at 1200 °C for two hours. This increase is attributed to the two hours sintering and the γ formation temperature, which is located at 908.4 °C, as indicated by the DSC results above. The increased holding time facilitated the formation of more austenite in dual-phase steel [106]. Additionally, according to the DSC results, the ά begins to form at 117.9 °C upon cooling. Due to the relatively low cooling rate, not all of the formed γ had sufficient time to transform into the ά phase; therefore, the γ increased slightly compared to the 17-4PH powder (before sintering). Conversely, the γ amount dropped to 0.12 % in the DCTT 17-4PH sample sintered at 1200 °C for seven hours. The reasons behind this phenomenon are the elevated sintering temperature and the longer sintering time.

These factors promote the formation of δ-ferrite. It was noted that the γ transformed to δ-ferrite at a sintering temperature of around 1260 °C for 17-4PH materials with 0.04 wt.% of C [9], [13].

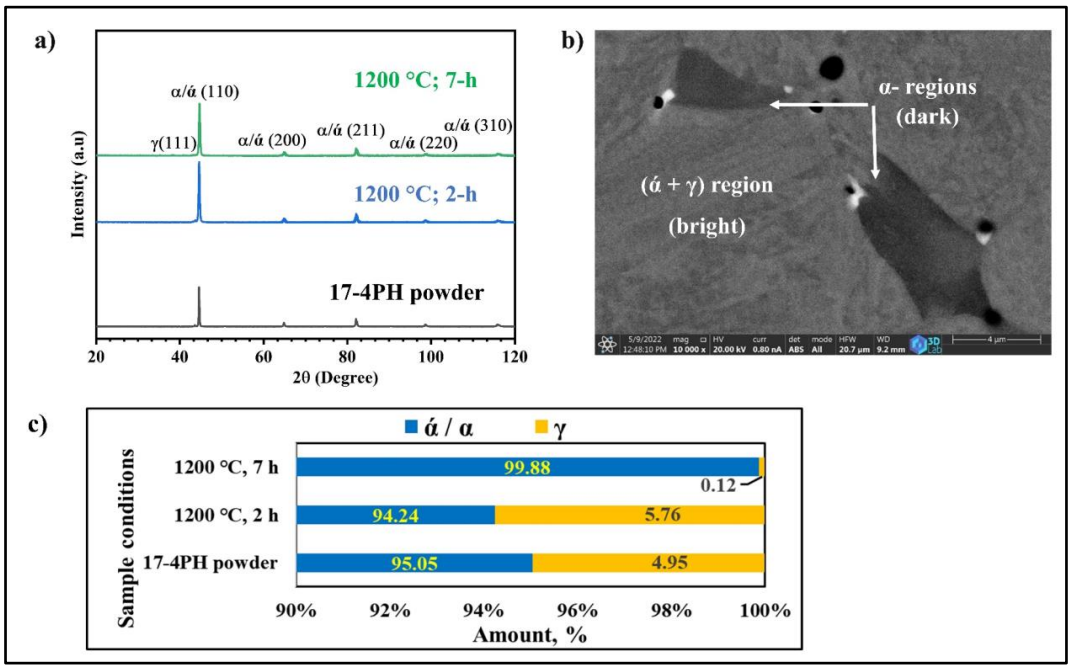

Figure 19. Illustrates a) the XRD diffractograms, b) the FIB-SEM image, and c) the phase amounts of DCTT 17-4PH samples. Note: The FIB-SEM image corresponds to a DCTT sample sintered at 1200 °C for two hours.

This temperature decreased significantly with a reduction in carbon content (the C in this study is 0.01 wt.%, table 1). Unfortunately, the DSC results did not reveal the δ formation due to the short duration of only 10 minutes. Meanwhile, the δ-ferrite formation is clearly visible in the microstructures of the DCTT 17-4PH samples sintered at 1200 °C, which will be discussed later. However, the relatively long sintering time allows for an extended diffusion process that might enable the complete transformation of γ to δ-ferrite at the elevated sintering temperature of 1200 °C. Consequently, the δ-ferrite transformed back to the γ-phase upon cooling and then to martensite, according to the phase transformation diagram of the 17-4PH materials [13]. Additionally, the amount of δ-ferrite did not fully transform to γ because the sintering time of seven hours is much longer than the cooling time (two hours, based on the cooling rate of 10 °C/min). Therefore, the γ decreased significantly while the α/ά increased. Moreover, the increase of α/ά in the case of seven hours compared to the two hours of sintering primarily pertains to the α. This increased the density of the seven-hour samples because BCC (α) demonstrates a faster atomic diffusion (densification) rate compared to FCC (γ) crystal structures [103].

4.2.3 ImageJ porosity analysis

The effect of cold pressing on reducing porosity is shown in Figure 20. The results demonstrate a decrease in porosity from 5.65 % to 1.13 % as cold pressing increases from 800 to 1600 MPa, respectively, after seven hours of sintering at 1200 °C.

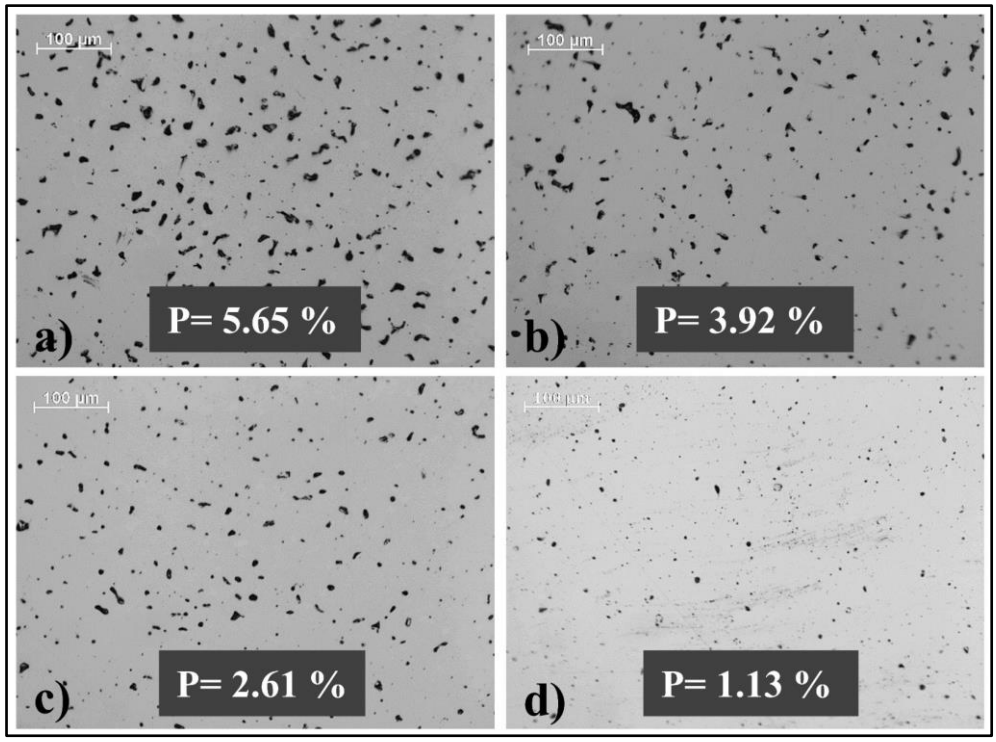

Figure 20. The impact of cold pressing on the optical microscopic ImageJ porosity of DCTT 17-4PH samples cold pressed at a) 800 MPa, b) 1000 MPa, c) 1200 MPa, and d) 1600 MPa after seven hours of sintering at 1200 °C.

4.2.4 Volume shrinkage measurements

The volume shrinkage results of DCTT 17-4PH samples are presented in Figure 21. It shows decreased shrinkage with increasing cold pressing and sintering times. The volume shrinkage was12.99% and decreased to 3.29% for samples cold pressed at 800 and 1600 MPa, respectively, and sintered for two hours. This occurs due to improved relative green density (or a decrease in porosity) with increasing cold pressing, which leads to enhanced relative green density. The volume shrinkage decreases as the difference between relative green and relative sinter densities diminishes [13], [103]. As a result, the DCTT 17-4PH samples retain their shapes after sintering. However, when the green samples are manufactured at the same cold pressing (1600 MPa), increasing the sintering time to seven hours results in an increase in volume shrinkage to 5.53 % instead of 3.29 % for two hours of sintering. This is due to a higher relative sinter density

compared to the relative sinter density after two hours of sintering. This occurs because of the appearance of the δ phase, which transforms from the γ phase (the γ amount dropped to 0.12 after seven hours of sintering), according to the XRD results. An increase in the δ phase leads to a rise in the density of PSM 17-4PH materials [13]. More shrinkage will occur during the crystal structure transformation from FCC (γ) to BCC (δ).

The 17-4PH sample shrank more as the ferrite content increased[103]. Decreasing porosity with increasing sintering time, due to the completion of the diffusion process, is another reason for the increased volume shrinkage; the dimensions of the DCTT 17-4PH samples will decrease with reduced porosity. However, the highest relative green and relative sinter densities reported in the literature for PSM 17-4PH samples were approximately 80 % and 93 %, respectively [13]. This significant difference between the green and sintered densities resulted in a much higher volume shrinkage, around 12 %. The density of the green samples before sintering influences the shrinkage ratio of the sintered parts. Increased green density reduces the shrinkage of sintered samples [13], [24], [30]. Therefore, applying high cold pressing and relatively low sintering temperatures during the production of stainless-steel materials is preferable to minimise shrinkage. This approach allows the samples to maintain their shape throughout the technological manufacturing cycle[13], [24]. For instance, gear-components created through pressing and sintering demand exceptional dimensional precision [13]. Furthermore, the tooling necessitates considerable dimensional accuracy, as indicated in [107]. Shrinkage affects sample geometry, precision, cost, and process efficiency [108].

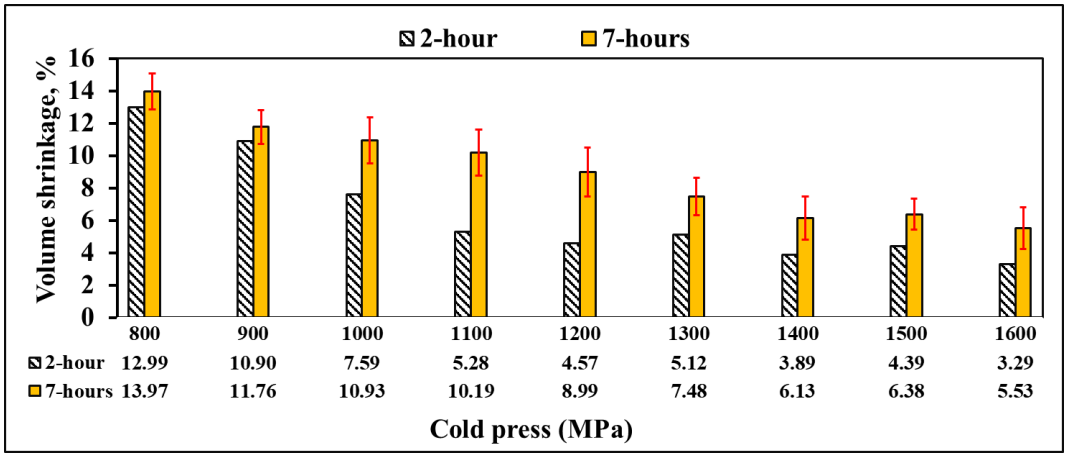

Figure 21.Volume shrinkage of selected DCTT 17-4PH samples sintered at 1200 °C for different times.

4.2.5 SEM, EDS, and FIB-SEM analyses

The SEM microstructures of DCTT 17-4PH samples are shown in Figure 22. The results indicate that most of the black regions are pores, some of oxides (e.g. MnO and SiO2). The pores are larger in the samples sintered at 1000 and 1100 °C, as seen in Figure 22 (a and b). These sintering temperatures did not complete the bonding of adjacent particles, which is considered the first stage of sintering. This was due to an insufficient sintering process. Increasing the sintering temperature to 1200 °C (Figure 22 (c)) resulted in larger grain sizes, indicating the adhesion stage between the solid and porous phases. This led to fewer pores and higher density compared to both DCTT 17-4PH samples sintered at 1000 and 1100 °C, as confirmed by the densification results above. This was due to the appearance of α grains alongside the γ grains as a result of the phase transformation of the 17-4PH materials according to the XRD results above. However, extending the sintering time from two to seven hours, a prolonged diffusion process, at a fixed sintering temperature of 1200 °C resulted in very few pores and nearly doubled grain size compared to the two-hour sintering. Additionally, the ά-morphologies appear as thin plates across all samples, regardless of the sintering conditions. The martensite type in the Fe-C alloys is referred to as ά [109]. The ά can be found in various morphologies depending on the sintering temperatures and cooling rates (e.g., lathe and thin plate martensitic structures). However, there are two distinct intensity regions, the (ά + γ)-region and the α-region, which can be easily observed. There is no indication of the burning microstructure after seven hours of sintering. Additionally, the ά-morphology and the α-regions were clearly visible in the samples sintered for seven hours (Figure 22 (d)) compared to that sintered for two hours (Figure 22 (c)). This phenomenon is corroborated by the XRD results, which show an increase in BCC crystal structures attributed to the α-phase, along with a significant decrease in the FCC crystal structure of the samples sintered at 1200 °C for seven hours. This indicates that the FCC transformed into the BCC crystal structure, resulting in greater shrinkage. This finding confirms the higher shrinkage in DCTT 17-4PH samples sintered at 1200 °C for seven hours compared to those sintered for two hours. However, the grains exhibited stronger interactions during the seven-hour sintering process compared to the two-hour process. This strong interaction leads to smoother grain boundaries in the case of seven hours of sintering compared to those of two hours (Figure 22 (e and f), respectively). However, the EDS findings indicate that the ά+ γ-region contains higher Ni and lower Cr levels compared to the α-regions. This is due to Cr and

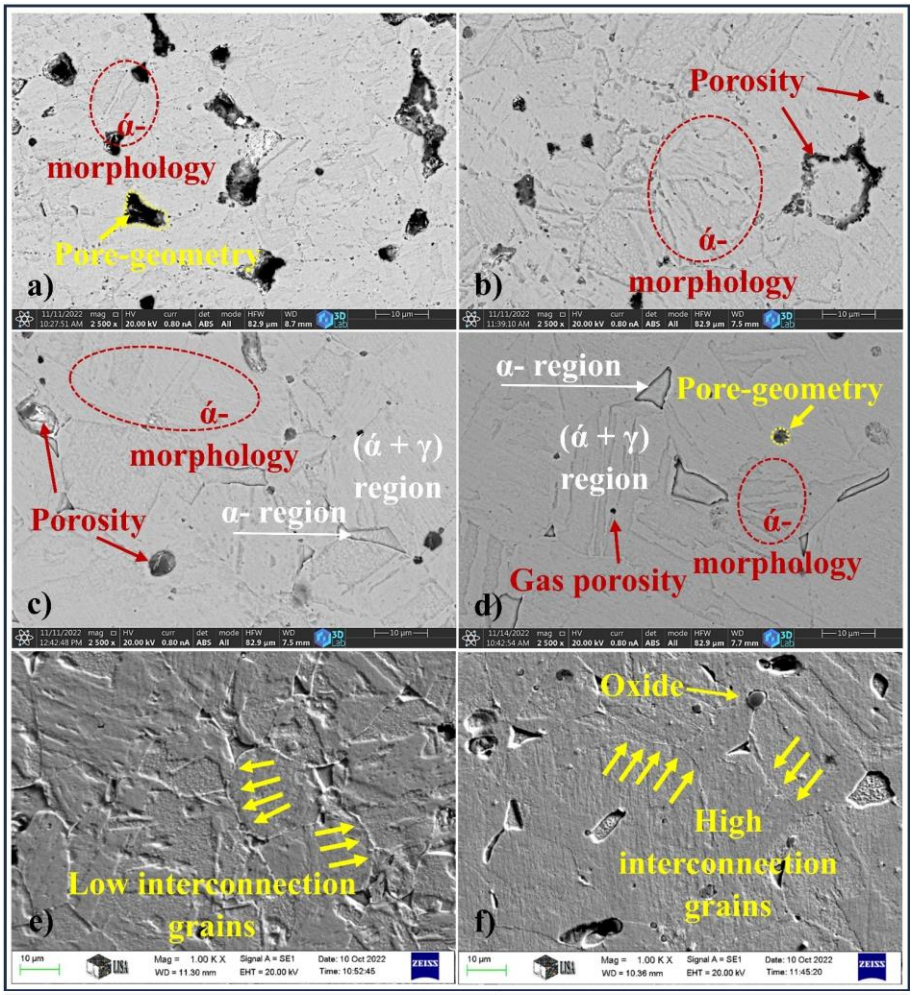

g)

(ά + γ)-region		α-region	
Element	Weight %	Element	Weight %
SiK	0.61	SiK	0.72
NbL	9.74	NbL	9.90
CrK	16.13	CrK	21.68
MnK	0.23	MnK	0.33
FeK	65.55	FeK	63.00
NiK	3.92	NiK	2.52
CuK	3.80	CuK	1.84

h)

(ά + γ)-region		α-region	
Element	Weight %	Element	Weight %
SiK	0.65	SiK	0.75
NbL	10.52	NbL	11.43
CrK	15.80	CrK	21.48
MnK	0.42	MnK	0.00
FeK	64.39	FeK	62.90
NiK	4.30	NiK	2.16
CuK	3.91	CuK	1.27

Figure 22. The SEM images of DCTT 17-4PH samples cold-pressed at 1600 MPa and sintered under various conditions: a) 1000 °C for 2 h; b) 1100 °C for 2 h; c) and e) 1200 °C for 2 h; d) and f) 1200 °C for 7 h. The EDS results for the specified regions in c) and d) are shown in g) and h), respectively.

Ni being stabilising elements in the α and γ phases, respectively, of stainless-steel materials [110]. Ni enhances γ stability by reducing the α and ά transformation temperatures of the materials [110], [111]. However, extending the sintering time to seven hours did not affect the chemical compositions of the DCTT 17-4PH samples that were evaporated. For instance, the

EDS spectra of Cu, Cr, and Ni contents in the DCTT 17-4PH samples (sintered for two and seven hours) exhibit similar levels to the chemical composition analyses of the received 17-4PH powder (Table 6).

Furthermore, increasing the sintering time from two to seven hours resulted in the grain coarsening stage of sintering according to Figure 23. It was noted that the mean grain sizes were around 20 and more than 38 µm for sintering times of two and seven hours, respectively. Ultimately, the seven hours of sintering led to a notable reduction in porosity, thereby increasing the density.

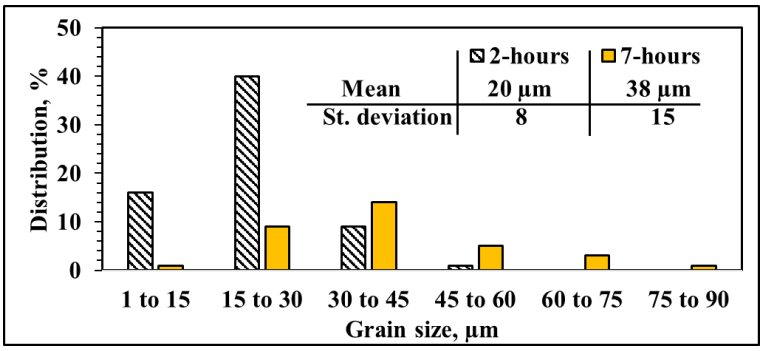

Figure 23. Grain size distributions by ImageJ analysis of DCTT 17-4PH samples cold pressed at 1600 MPa, sintered at 1200 °C, and for different times.

The elemental mapping results for the selected DCTT 17-4PH samples obtained from FIB-SEM processing are shown in Figure 24. The results visually illustrate the variations between the two distinct areas (α-region and ά + γ-region), primarily in the distribution of Cr and Ni content. It also indicates the sites of Cu alongside with the α-region. Furthermore, it is evident that the α-region is larger and more pronounced in the DCTT samples sintered for seven hours compared to those sintered for two hours. The mean concentrations of Cr, Ni, and Cu across all microstructures were 25%, 4%, and 4%, respectively.

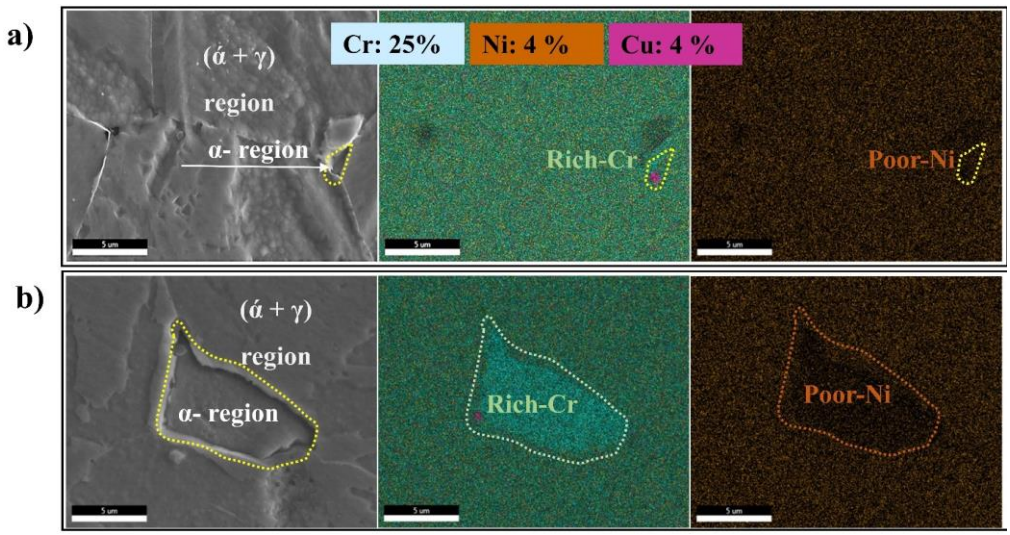

Figure 24. Displays FIB-SEM elemental maps of DCTT 17-4PH samples produced at a) two hours and b) seven hours of sintering.

4.2.6 Vickers hardness test

The influence of various sintering conditions on the Vickers hardness of the selected DCTT 17-4PH samples is illustrated in Figure 25. The results indicate a marginal increase in hardness with extended sintering time from two to seven hours, rising from 316 ± 9 to 321 ± 10 HV, respectively, for samples cold pressed at 1600 MPa and sintered at 1200 °C. In contrast, increasing cold pressing from 800 to 1600 MPa shows a significant increase, from 163 ± 12 to 316 ± 9 HV. This improvement is attributed to reduced porosity, which is more pronounced with increased cold pressing than with the effect of prolonged sintering time. The hardness of stainless-steel materials increases as porosity decreases [3], [25], [112]. For instance, it was noted that the hardness of PSM 17-4PH parts with a low relative density of 92.45 % was 180 HV (derived from a Rockwell hardness measurement of 89 HRB)[113]. The hardness increased to 208 HV (converted from a Rockwell hardness measurement of 65 HRA) with an increase in relative density to 93.47 % [25], [113]. Clearly, the HV is influenced more by decreasing porosity than by phase transformation. However, reducing the amount of γ and increasing the amount of α should lower the HV values after seven hours of sintering, according to the XRD results. Generally, the hardness of the γ-phase is greater than that of the α phase in stainless-steel materials [13]. Nevertheless, the HV of the DCTT 17-4PH samples increased slightly after seven hours compared to the two-hour sintering duration. This is due to the effect of decreased porosity.

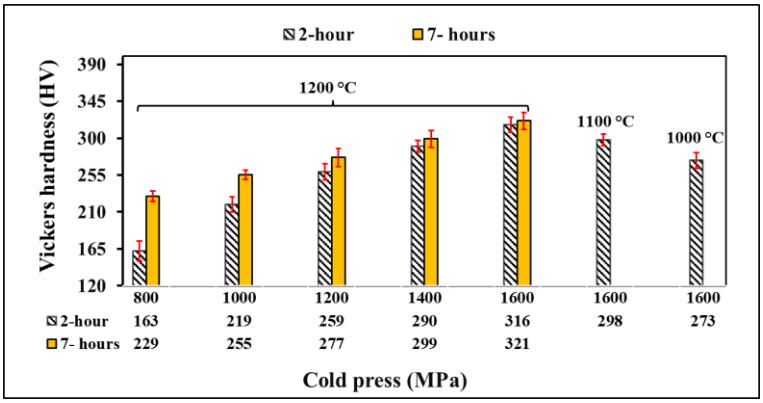

Figure 25. Vickers hardness of selected DCTT 17-4PH samples cold pressed at 1600 MPa and sintered at 1200 °C.

4.2.7 Compressive strength test

The compressive stress-strain tests of selected DCTT 17-4PH samples are presented in Figure 26 (a). Regardless of the production conditions, the curves exhibit similar behaviour. These results indicate an increase in compressive strength properties with longer sintering times and higher temperatures, primarily due to a reduction in porosity. The highest compressive strength was observed after seven hours of sintering at 1200 °C, while the lowest occurred after two hours at 1000 °C. The enhanced compressive yield strength results, shown in Figure 26 (b), illustrate this effect. The measurements were recorded with a 0.2 % offset. The compressive yield strength rose from 868 ± 5 to 923 ± 5 MPa as sintering temperatures increased from 1000 to 1200 °C for two hours. Extending the sintering time to seven hours further improved the compressive yield strength to 953 ± 10 MPa due to a significant reduction in porosity and more uniform pore geometry. For instance, PSM produced parts of chromium alloy steel with enhanced tensile strength attributed to regular pore geometries and low porosity at elevated sintering temperatures [30]. As previously mentioned, extending the sintering time to seven hours resulted in a doubling of the grain size. An increase in grain size typically decreases the yield strength of stainless-steel materials by reducing grain boundaries, which impede fracture propagation (the grain boundaries serve as barriers to dislocation movements) [114]. However, in this dissertation work, the reduction in pores had a more positive impact on the improvement of compressive strength properties than the effect of grain size growth. Additionally, the high interaction between grains (smooth grain boundaries) after seven hours of sintering may contribute to the minimal improvement in strength properties compared to samples sintered for

only two hours. The reduction of the γ-phase after seven hours of sintering did not significantly affect strength properties.

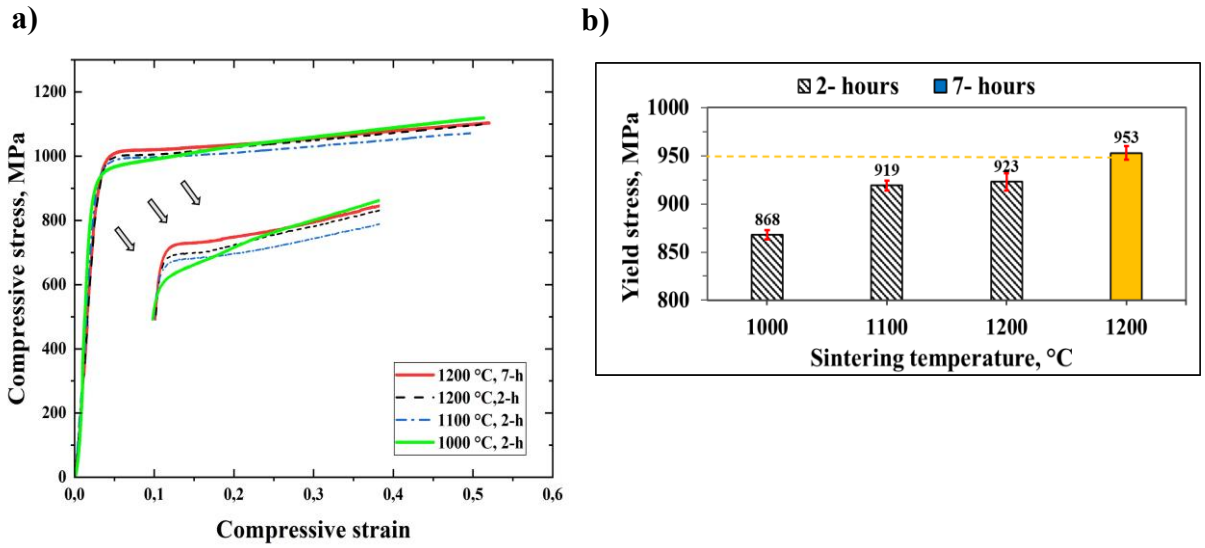

Figure 26. Shows a) the compressive stress-strain curves and b) the compressive yield strength of selected DCTT 17-4PH samples that were cold pressed at 1600 MPa and sintered under the indicated conditions.

However, the optimal compressive yield strength that can be achieved is approximately 953 ± 10 MPa after seven hours of sintering at 1200 °C. This value is significantly higher than those reported in previous studies, which utilised much higher sintering temperatures than the present study. However, due to the absence of compressive tests in the literature, a rough prediction of the compressive yield strength will be made based on the tensile yield strength in this research. The compressive yield strength is greater than the tensile yield strength of stainless-steel materials. According to [70], the compressive yield strength of the 17-4PH parts manufactured by SLM surpassed the tensile yield strength by 25 %. For instance, the tensile yield strength was below 470 MPa for 17-4PH parts (cold pressed at 600 MPa, sintered at 1340 °C for one hour) with a relative density of approximately 92% [24]. Furthermore, the maximum tensile yield strength was 688 MPa for PSM 17-4PH parts cold pressed at 600 MPa, sintered at 1340 °C for 45 minutes, and aged at 538 °C with a relative density of around 93 %[25]. The two previous studies indicated that the compressive yield strength ranged from 588 to 860 MPa, depending on the 25 % calculation method. Therefore, the current work achieved a 10% higher compressive strength compared to the maximum reported in the literature. This achievement was due to higher sinter density. Although, according to the available literature, 1260 °C was the lowest

sintering temperature employed to produce PSM 17-4PH parts, which had poor density and strength. While this work demonstrated the employing of even lower sintering temperature (1200 °C) compared to the available literature to produce PSM 17-4PH parts with improved density and strength.

4.2.8 Summary

This dissertation was conducted to address scientific data gaps related to the insufficient sintering of PSM 17-4PH parts. It examined the effects of cold pressing, sintering time, and temperature on the properties of the DCTT 17-4PH samples. The measurement of densification was conducted using both dimensional and Archimedes methods. Optical, SEM, and EDS analyses were conducted. The measurement of Vickers hardness and compressive strength have also been conducted. The relative green density increased by approximately 13 % as the cold pressing rose from 800 to 1600 MPa, attributed to decreased porosity. A proportional relationship was identified between relative sinter density and relative green density; the reduction in porosity led to larger contact areas between compacted powder particles, enhancing the diffusion process and increasing relative sinter density. Extending the sintering time to seven hours at 1200 °C raised the relative sinter density by about 4 % due to reduced porosity and an increase in the δ-ferrite amount, which supports the densification properties of stainless-steel materials. The maximum relative sinter density achieved was 98.07 ± 0.4 %, which is approximately 5 % higher than reported in the literature. A linear regression model aligned with the actual results concerning the effect of sintering time on relative sinter density. A semi-parabolic relationship was found between sintering temperature and relative sinter density. Therefore, a polynomial regression model was developed to describe the relationship between sintering temperature and relative sinter density. Due to low sintering temperatures of 1000 °C for two hours, microstructure analyses of DCTT 17-4PH samples revealed a significant presence of pores. Increasing the sintering temperature to 1100 °C resulted in smaller pores, although the pore geometry remained irregular. Furthermore, at 1200 °C, α-regions emerged, with slight grain growth and a more regular pore geometry. Sintering at 1200 °C for seven hours led to the lowest porosity, but the grain size doubled from 40 µm (at 1200 °C for two hours) to over 80 µm, with highly interacted grains (smooth boundaries), and non-evaporated chemical elements. However, all DCTT 17-4PH samples sintered at 1200 °C (for both two and seven hours) exhibited similar microstructures characterised by ά-morphologies, with two distinct regions observed: the α-

region and the (γ+ά)-region. The EDS analyses showed differing amounts of Cr and Ni in these regions. The α-region contained a 25 % higher chromium weight percentage and a 50 % lower nickel weight percentage compared with the (γ+ά)-region. This supports the distinction between these regions, as Cr is considered a ferrite stabiliser, while Ni is regarded as an austenite stabilizer. However, sintering for seven hours reduced the γ amount to 0.12 % compared to 5.76 % for DCTT 17-4PH sintered for two hours. This reduction occurred due to the extended sintering time of seven hours, which transformed most of the γ into δ. The very short cooling time, relative to the holding time, did not allow the entire δ amount to convert back to γ before transforming into ά. Consequently, the α/ά ratio increased after seven hours compared to two hours of sintering, with the increment in the α/ά ratio attributed to the increased α amount. The α-regions appeared larger and more distinct after seven hours of sintering compared to those observed after two hours. This work reduced the volume shrinkage from 12.99 % to 3.29 % for DCTT 17-4PH samples cold pressed at 800 and 1600 MPa (sintered for two hours at 1200 °C), respectively, due to decreased porosity and a minimal difference between relative sinter and relative green densities. However, it increased again to 5.53 % when the sintering time was extended to seven hours. This occurred due to the emergence of δ as a replacement for γ, according to the XRD analysis. This allowed for more shrinkage during the crystal structure transformation from FCC (γ) to BCC (δ-ferrite). Increasing cold pressing from 800 to 1600 MPa (at 1200 °C for two hours) achieved the highest Vickers hardness, increasing by 41 %, primarily due to a reduction in porosity. Vickers hardness rose by approximately 2 % with an increase in sintering time from two to seven hours, mainly attributed to the decrease in porosity and the more regular pore geometry, which measured around 321. This value is 40 % higher than what is reported in the literature. Consequently, the yield strength increased by about 4 % when the sintering time was extended from two to seven hours at 1200 °C, representing a 10 % increase compared to the literature (which sintered at significantly higher temperatures). Extending the sintering time to seven hours doubled the grain size but reduced porosity, thereby enhancing the material's strength properties. However, the increased grain size and reduced γ content are two factors that can diminish Vickers hardness and strength after seven hours. Nevertheless, Vickers hardness and strength showed slight improvement compared to the values for the DCTT 17-4PH samples sintered for two hours, due to the effects of decreased porosity, more regular pore

shapes, and enhanced grain interaction. The phase transformation after seven hours had a minimal impact on Vickers hardness and strength properties.

4.3 Results of 17-4PH powder with different particle sizes

This dissertation work analyses the effect of another PSM parameter such as decreasing powder particle size on improving the density of PSM 17-4PH parts. In addition, it investigates the possibility of producing PSM samples with satisfactory mechanical properties utilising recycled 17-4PH powder.

4.3.1 Dimensional and Archimedes density measurements

The densification results of original and recycled samples are presented in Figure 27. The relative green densities increased from 90.88 ± 0.30 to 91.76 ± 0.18 % as the particle size of the original powder decreased from 45–63 µm (O3)) to 15–32 µm (O1). After sintering for one hour at 1200 °C, the relative sinter densities of the original samples were 94.17 ± 0.29 and 95.12 ± 0.44 % for O3 and O1, respectively. On the other hand, the density of the recycled samples decreased by less than 1% relative to the original samples in both the green and sinter values. Furthermore, the green and sinter densities of both original and recycled samples increased by approximately 1% with decreasing powder particle size. Reducing particle size enhances the contact area between compacted particles, thereby reducing porosity and accelerating the diffusion process during sintering, which in turn increases density.

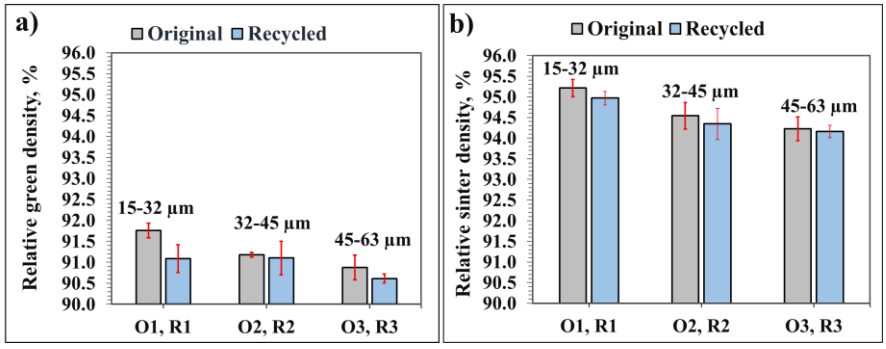

Figure 27. The effect of different particle size on a) relative green density, and relative sinter density of original and recycled samples.

4.3.2 ImageJ porosity and optical microstructure analyses

The results of the pore area and circularity, analysed using ImageJ for both unetched original and recycled samples, are presented in Figure 28. The findings indicate a slight increase in pore area with larger particle sizes for the original samples (O3), rising from approximately 14 to

around 25 µm as the particle size distribution increased from 15–32 (O1) to 45–63 µm (O3), respectively. In contrast, the pore area for recycled samples increased from about 30 to around 60 µm. Thus, the pore area of the recycled samples reached double the values compared to the original samples. This may be attributed to a higher content of gas pores in the recycled powder, originating from the 3D printing process. These pores tend to merge during sintering, resulting in larger pores. However, the average pore circularity showed a slight increase with decreasing particle size, rising from 0.76 to 0.87 as the particle size distribution decreased from 45–63 (O3) to 15–32 µm (O1). For the recycled samples, it increased from 0.77 to 0.88. Although there is a minimal increase in the circularity of the recycled samples compared to the original samples, the reduction in particle size distribution has no significant effect on the pores' circularity in both original and recycled samples. The pores of the recycled 17-4PH samples exhibited slightly higher circularity compared to the original SLM 17-4PH samples [17].

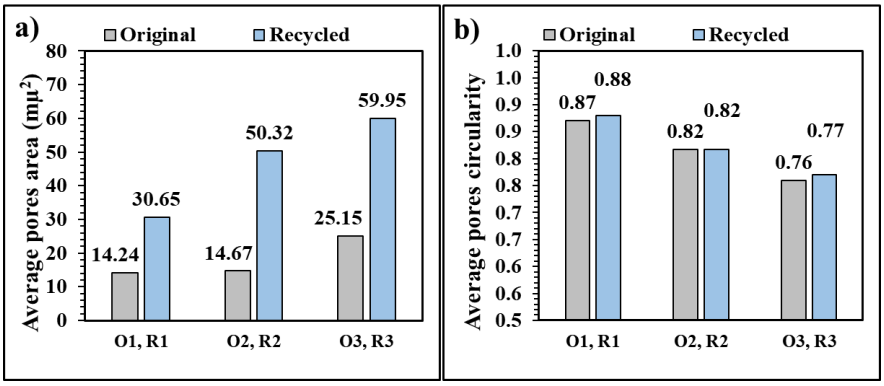

Figure 28. Represents a) average pores area, and b) pores circularity by ImageJ of unetched original and recycled samples.

The optical microstructure observations of original and recycled samples are presented in Figure 29. No noticeable differences were found between the microstructures of the original and recycled samples. It is easily observed that the grain size is relatively lower for Figure 29 (a and c) compared to Figure 29 (b and d) microstructures. Additionally, the grain size is almost similar

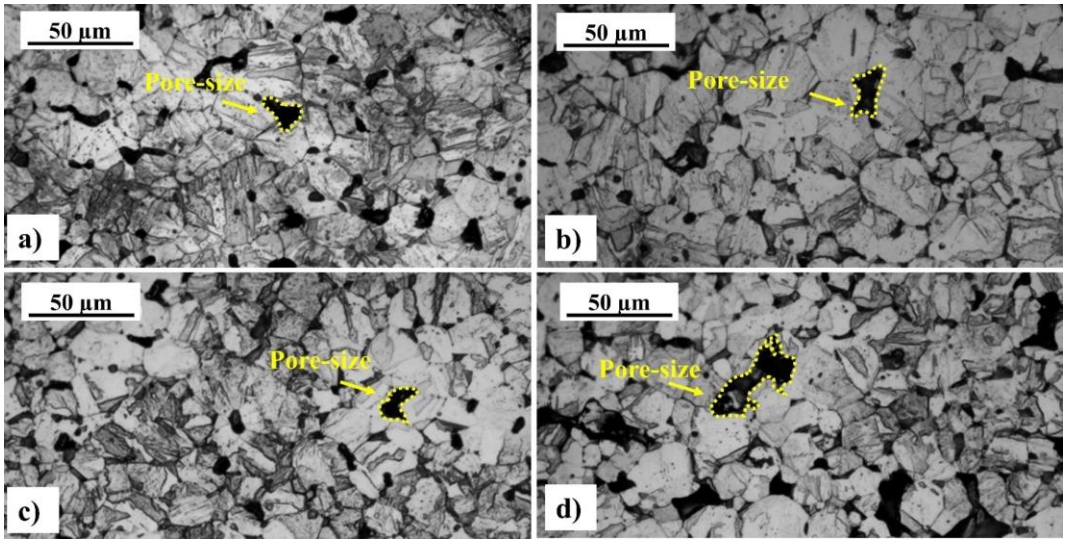

Figure 29. The optical microstructure of cross-sectioned of etched of a) O1, b) O3, c) R1, and d) R3 samples.

across each particle size distribution for both sample types. The microstructure observations highlight differences in pore area and circularity, as discussed previously. It is evident that the pore size in the recycled samples is larger than that in the original samples (yellow rows), particularly for samples manufactured from the particle size distribution of 45–63 µm (Figure 29 (b and d)). The pore geometry is more regular in the Figure 29 (a and c) compared to Figure 29 (b and d) microstructures, regardless of the sample type. However, the presence of welded particles in the recycled powder did not significantly affect the pore size. This is due to the sieving process that the recycled powder underwent for specific particle size distributions. The enlargement of pore size can be achieved by increasing both the size of the powder particles and the irregularity of their shapes, as it was stated by M. Higashi et al. [13], [115]. Additionally, a decrease in particle size resulted in more regular pores and higher densification in pressed and sintered 17-4PH materials [25].

4.3.3 SEM images and X-ray analyses

Backscattered-SEM and XRD analyses were conducted to gain a deeper understanding of the microstructures of both original and recycled samples. The Backscatter-SEM results are shown in Figure 30. The results revealed two distinct regions (dark and bright), regardless of the sample type (these results align closely with the microstructural findings presented in section 4.2). The dark region is labelled as number 1 and the bright region as number 2. However, the XRD analysis indicated similar phases for the 17-4PH before and after sintering (both powders and

sintered samples), which consisted of α/ά and γ peaks. It was impractical to differentiate between the BCT and BCC structures due to the extremely low carbon content of the 17-4PH powder, as previously discussed in section 4.2.1. However, the two regions (1 and 2) revealed by the SEM analysis correspond to the α-region and the ά/γ-region, respectively.

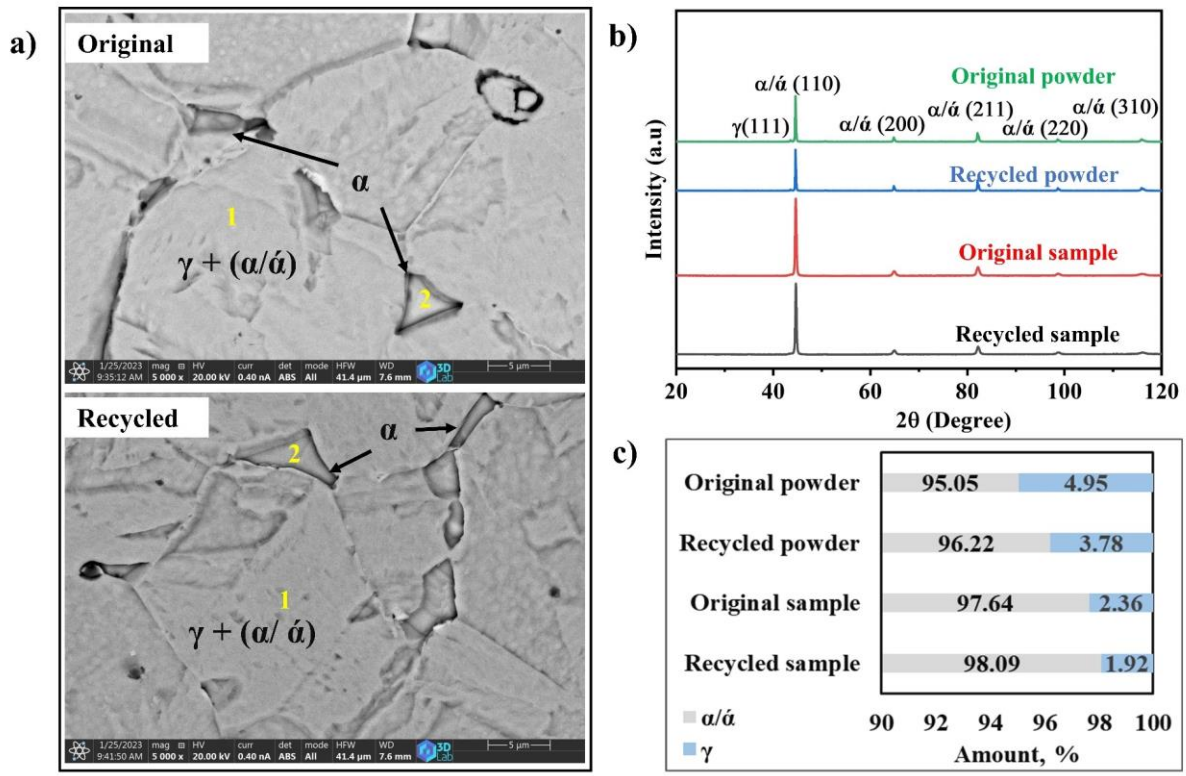

Figure 30. Phases approved by a) Backscattered-SEM images, b) XRD pattern, and c) XRD phases volume fraction of original and recycled samples.

Figure 30 (c) presents the volume fraction of the α/ά and γ phases before and after sintering. It shows that the α/ά ratio rose after sintering for both the original and recycled samples. It increased from 95.05 to 97.64% for the original powder and samples and from 96.22 to 98.09% for the recycled powder and samples. The reason for this increment in α/ά content was the appearance of α-islands after sintering at 1200 °C, which were not present in the initial powders. In other words, the initial particles exclusively possess austenitic and martensitic structures. Therefore, based on this information, it can be concluded that the rise in the α/ά ratio following sintering can be attributed to the increase in α-content. Additionally, across all particle size distributions, the volume fraction of α/ά in the recycled samples was slightly higher than that of the original samples. This increase was due to a marginally higher carbon content in the recycled powder compared to the original powder, as previously indicated in the chemical composition

analysis, which elevated the ά content. For example, ά content increased with carbon content in high-strength steel materials [116].

4.3.4 Compressive strength test

The compressive stress-strain tests of selected original and recycled samples are presented in Figure 31. All stress-strain curves exhibit similar behavior. The results improved with a reduction in powder particle size; the compressive yield strengths for original samples with particle size distributions of 45–63, 32–45, and 15–32 µm were 873, 888, and 917 MPa, respectively. The recycled samples with particle size distributions of 45–63, 32–45, and 15–32 µm showed compressive yield strengths of 890, 895, and 923 MPa, respectively. However, the compressive yield strength of all the recycled samples increased by approximately 2% compared to the original samples. Although the recycled samples had a larger pore area than the original samples, the higher carbon content in the recycled powder, compared to the original powder, may have contributed to this increase. Higher grain boundaries resulting from the small particle size of powders have another impact on enhancing the strength properties of both original and recycled samples. Additionally, recycled samples exhibited a slightly higher pore circularity compared to that of original samples, which improved the mechanical properties of stainless-steel parts [3], [53], [105], [114]. However, the optimum compressive yield strength was 923 MPa for the recycled sample with the lowest particle size distribution of 15–32 µm.

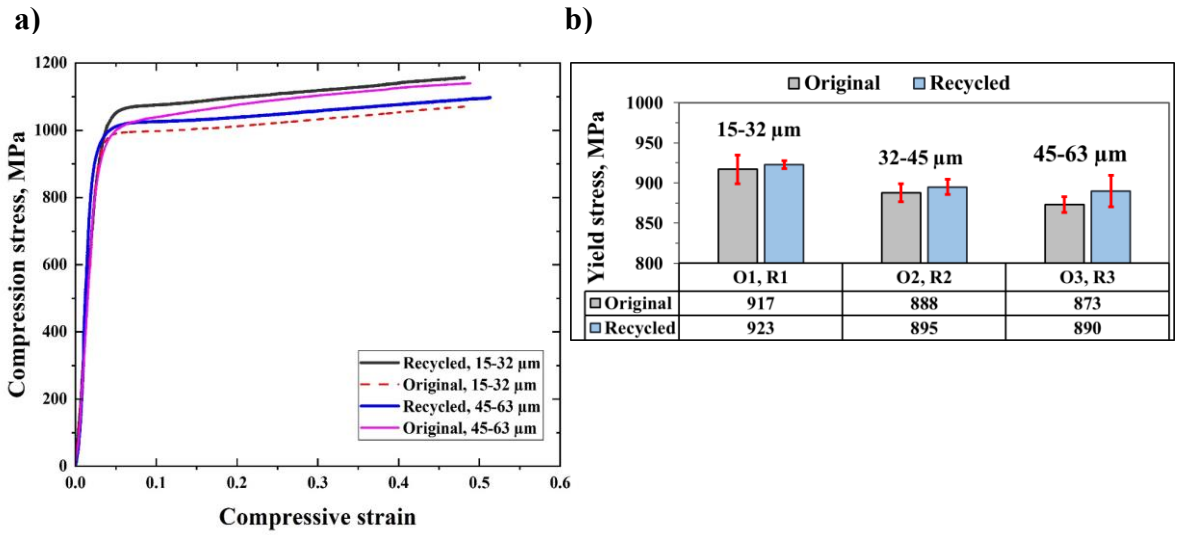

Figure 31. Represents a) compression stress-strain curves, and b) the compressive yield strength of original and recycled 17-4PH samples

4.3.5 Summary

This study was conducted to investigate the feasibility of recycling 17-4PH powder alongside the original powder for the production of PSM samples. Furthermore, the study examined the impact of particle size distribution on the properties of the produced original and recycled 17-4PH samples. Dimensional and Archimedes density measurements were carried out. Microstructural observations were performed using optical, SEM, and XRD analyses. Compressive strength tests were conducted to evaluate the mechanical properties of both original and recycled samples. Both the original and recycled samples demonstrated similar relative green and sinter densities. Both results showed a 10% and approximately 3% increase in relative green and sinter density, respectively, compared to the reported literature, attributed to the application of high cold pressing. The effect of reducing powder particle size was around 1%. The recycled samples displayed a larger pore area (approximately double) compared to the original samples, due to the high content of entrapped gases in the recycled powder, which was linked to the multiple iterations of the 3D-printing process. Reducing powder particle size decreased the pore area to about half for both original and recycled samples. The difference in pore circularity between the original and recycled samples is minimal and can be disregarded. The recycled samples showed a slightly higher martensite content than the original samples, attributed to the influence of carbon content, which was slightly greater in the recycled samples than in the original samples; however, this difference is considered insignificant. The stress-strain curves for both the original and recycled samples displayed similar behavior. The compressive yield strength increased by about 4% when the particle size was reduced from 45–63 to 15–32 μm, due to the decreased pore area and the higher grain boundaries present in the smaller particle size powders (15–32 μm). Based on the test results, it can be concluded that steel powder of type 17-4PH from the 3D printing process is recyclable, and the powder metallurgical product made using it has appropriate mechanical properties.

4.4 Results of optimisation induction sintering conditions

The lengthy sintering time associated with electrical furnace sintering can be significantly reduced by employing an induction furnace. The aim of this dissertation is to optimise the induction sintering process to achieve the best physical-mechanical properties of INDS 17-4PH parts. This will be done using the same range of cold pressing pressures and varying sintering times that are shorter than those used in electrical furnace sintering, as detailed in section 4.2.

4.4.1 Dimensional and Archimedes density measurements

The results of the green and sinter relative densities of 17-4PH samples under different cold pressing and 2.0 min of holding time are presented in Figure 32. It can be seen that the relative green density increased from 80.14 ± 0.29 to 92.88 ± 0.47% with increasing cold pressing from 700 MPa to 1600 MPa, respectively. To compare with earlier work, for example, P. K. Samal et al. used 760 MPa during cold compaction of 17-4PH samples, which resulted in relative green density of 80.67% [37]. Additionally, increasing cold pressing leads to an increase in the green density of steel parts [13], [36], [95]. However, the samples were crushed at a cold pressing of 700 MPa in earlier published work [117]. The absence of any binder such as wax and the relatively low load required to induce enough plastic deformation for this hard powder were the causes of that failure. Binder was avoided to dim the side effects of the organic compounds on the chemical compositions of this powder during the sintering process. However, maintaining the samples under cold pressing before releasing the load enhances the densification of green compacts of 17-4PH at 700 MPa. Furthermore, the increasing cold pressing has little influence on enhancing the relative sinter densities, the Archimedes relative sinter densities increased from 95.92 ± 0.15 to 98.79 ± 0.40% for different range of cold pressing between 700 to 1600 MPa, respectively, with holding time of 2.0 min and sintered at 1300 °C for 1-hour. Briefly, the impact of cold pressing on increasing relative sinter densities is around 3%, when the cold pressing is increased from 700 to 1600 MPa. In the context of conventional sintering, the relative sinter density of stainless-steel powdered materials increased as the relative green densities increased [13]. On the other hand, induction sintering provides similar densification results compared to conventional sintering, but in a significantly shorter time [118].

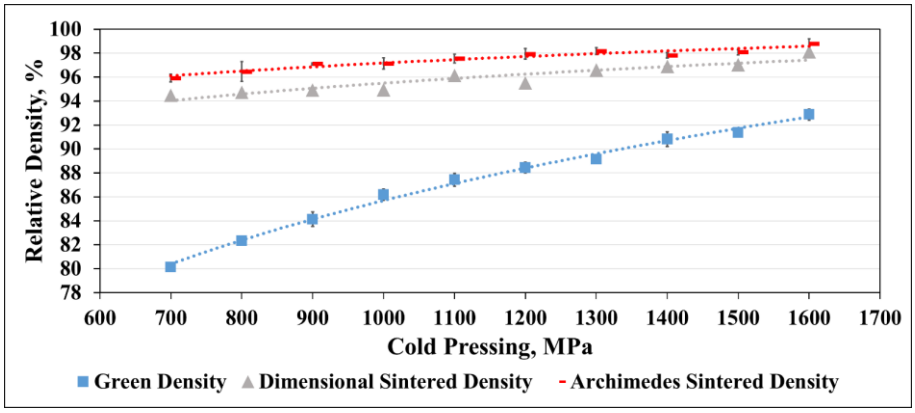

Figure 32. The effect of cold pressing on green and sintered densification of 17-4PH samples with holding time of 2.0 min and sintered at 1300 °C for 60-min.

The results of sintering time and temperatures effects are shown in Figure 33. They showed comparable relative sinter densities values for sintering time between 15−60 min (Figure 33 (a). Increasing sintering time from 15 to 120 min kept the relative sinter densities between around

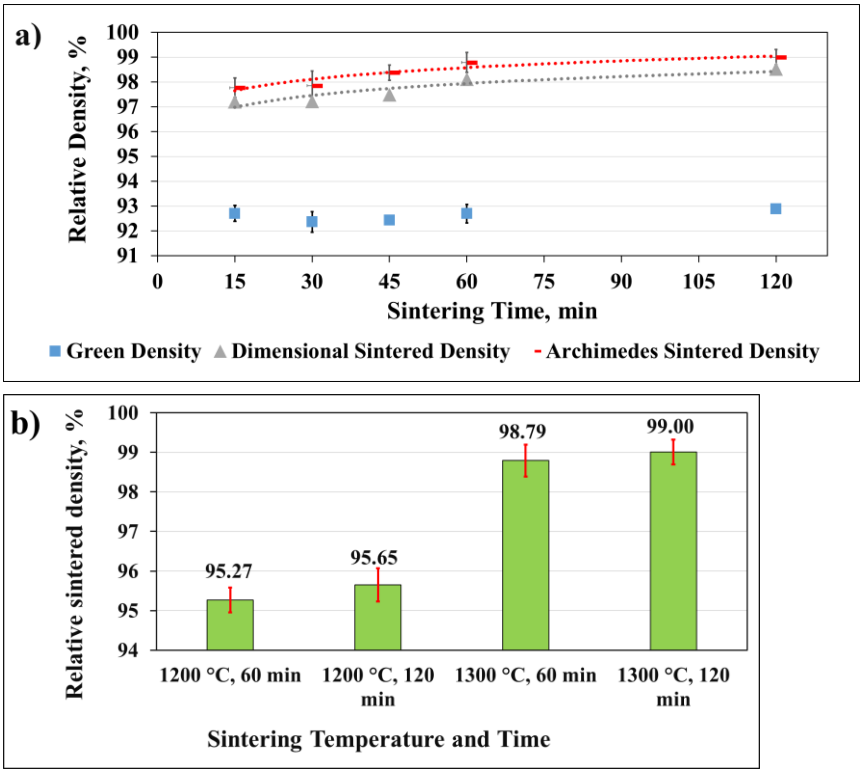

Figure 33. The effect of (a) sintering time (the samples sintered at 1300°C), and (b) sintering temperature and time of 17-4PH samples produced under cold pressing of 1600 MPa.

98−99%. The effect of raising temperature from 1200 to 1300 °C led to improve the relative sinter densities from 95.27 ± 0.31 to 98.79 ± 0.40% for one hour of sintering (Figure 33 (b). It can be noted also that increasing sintering time from one two hours did not results in a significant improvement of densification. However, increasing the sintering time or temperature improved the densification properties of a PSM 17-4PH part [24], [25].

4.4.2 Volume shrinkage

The sintering temperature has much higher influence than sintering time during induction sintering on volumetric shrinkage (the difference between samples volumes after and before sintering) of 17-4PH samples, as shown in Figure 34. The volumetric shrinkage increased from 8.10 ± 0.03 to 9.32 ± 0.91% with increasing sintering temperature from 1200 to 1300 °C for one hour of sintering, respectively. On the other hand, it increased to 15.09 ± 2.2% with increasing

sintering time from 60 to 120 min at 1300 °C. The cause behind these behaviors will be explained in the EBSD analysis's result. Generally, low shrinkage value is desired of commercial production. Because this allows the samples to keep their shape throughout the technological manufacturing cycle [13], [33], [117]. But 9−15% is relatively low and can be acceptable with such results of improving sintered densification at 1300°C. Microwave sintering at 1200 °C resulted in the lowest shrinkage volume of 8.19% of 17-4PH samples manufactured by metal injection molding technology [97], [119]. The shrinkage was more than 14% for 17-4PH samples manufactured by additive extrusion method using a tube furnace in a single thermal cycle at 1360 °C for 5 hours (a conventional sintering furnace) [10].

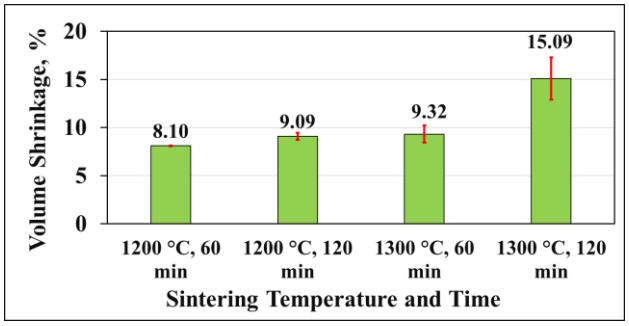

Figure 34. The effect of sintering temperature and time on volumetric shrinkage of 17-4PH samples, cold pressed at 1600 MPa

4.4.3 ImageJ porosity and optical microscope analyses

The results of ImageJ porosity analysis of selective positions on the unetched cross-sectional optical photos of 17-4PH samples manufactured at different cold pressing, and sintering temperature and time are presented in Figure 35. It can be noticed that the porosity decreased more than 4% with increasing cold pressing from 700 to 1600 MPa at sintering temperature of 1300 °C, and sintered for 60 min, Figure 35 (a and d). This happens due to the influence of increasing surface area of direct conducted particles, which consider the initiating of sintering processes by neck growth between contacted particles [13], [44]. Therefore, high compacted samples lead to high sintered density. Moreover, raising the sintering temperature from 1200 to 1300 °C decreased the porosity more than 2% with samples produced under cold pressing of 1600 MPa and sintered for 120 min, Figure 35 (e and f). These results confirmed by the densification results. Additionally, the porosity decreased by around 1% with increasing sintering time from 15 to 60 minutes, Figure 35 (c and d). But there was no noticeable difference between the density of samples sintered at one and two hours, Figure 35 (d and f). While

increasing sintering time from 1 to 7 hours decreased the porosity to around 2%, at 1600 MPa of cold pressing and 1200 °C of electrical (conventional) sintering temperature, see section 4.2. However, when compared to conventional sintering procedures, induction sintering's impact on sintering activation can significantly reduce sintering time[45].

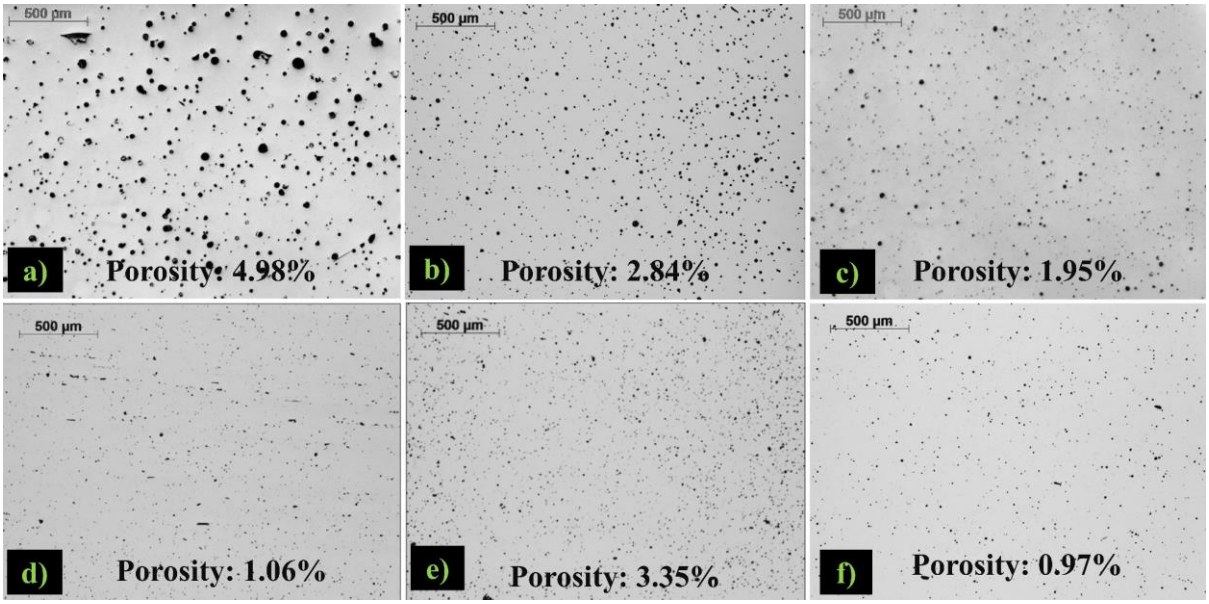

Figure 35. The ImageJ porosity 17-4PH optical microstructures manufactured at a) 1300 °C for 60 min at 700 MPa, b) 1300 °C for 60 min at 1000 MPa, c) 1300 °C for 15 min at 1600 MPa, d) 1300 °C for 60 min at 1600 MPa, e) 1200 °C for 120 min at 1600 MPa, and f) 1300 °C for 120 min at 1600 MPa

The results of optical microstructural analysis of etched cross-sectional 17-4PH samples are presented in Figure 36. The sintered 17-4PH microstructure consist of generally, dark areas which represent the ferrite and the bright areas refer to the austenite and (depend on the sintering conditions) martensite phases [13]. More details will be discussed in the section of EBSD analyses (section 4.4.4). However, it can be noticed that increasing cold pressing from 1000 to 1600 MPa and sintering temperature from 1200 to 1300 °C decreased the porosity significantly and changed the pores shapes from irregularity to more regular. These outcomes confirmed the densification results. Additionally, increasing sintering time from 60 to 120 minutes cause over coarsening of grain size. This effect has been approved by the grain size measurements using EBSD analyses in Figure 37. Additionally, the samples sintered for 15 minutes showed almost longitudinal grains shapes. It might happen due to insufficient time for completing sintering process. In addition, the eddy currents have different cycling direction which might cause

different growth direction along with limited sintering time, which resulted in amorphous elongated grain growing directions. However, sintering at 1200 °C shows triangle regions between grains due to incomplete of sintering.

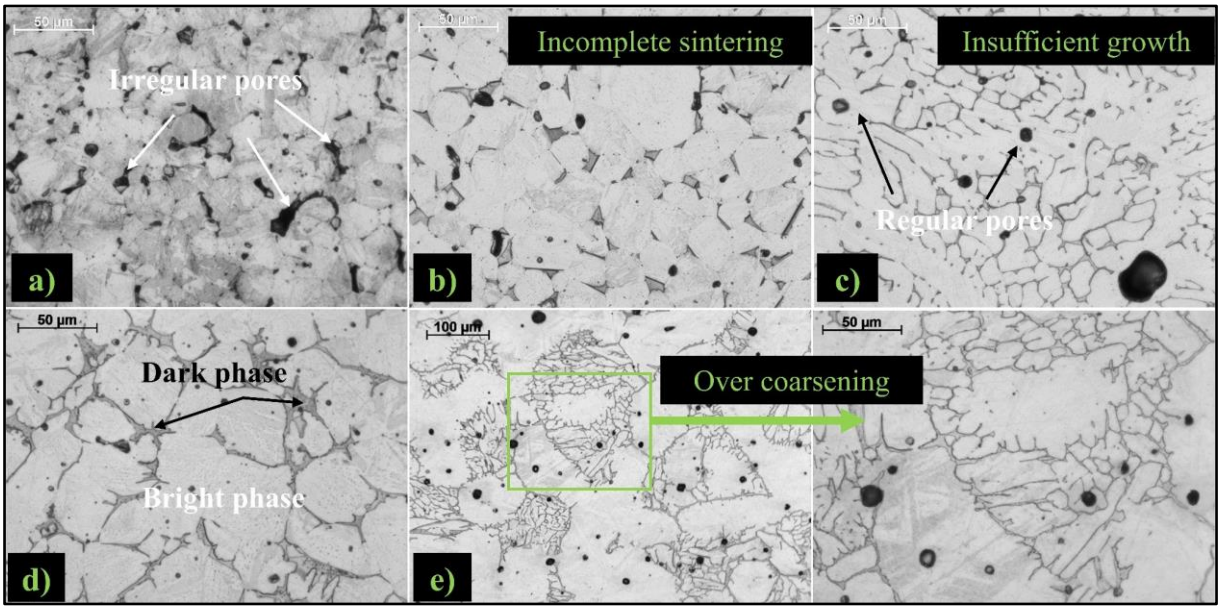

Figure 36. Represents etched optical photos of the 17-4PH samples manufactured at a) 1000 MPa, 1300 °C, 60-min, b) 1600 MPa, 1200 °C, 120-min, c) 1600 MPa, 1300 °C, 15-min, d) 1600 MPa, 1300 °C, 60-min, and e) 1600 MPa, 1300 °C, 120-min.

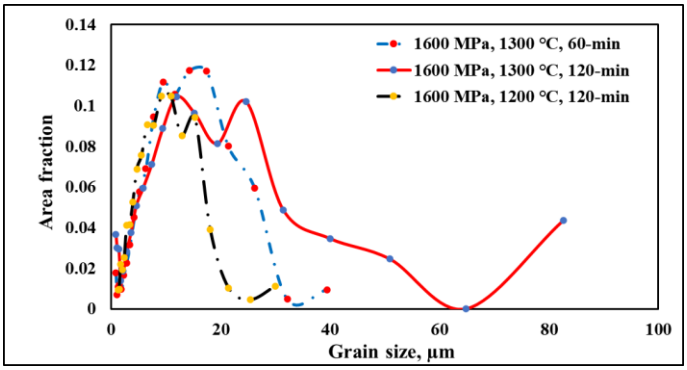

Figure 37. Represents the grain size measurements etched optical of the 17-4PH samples manufactured at indicated conditions using EBSD analyses.

4.4.4 SEM, EDS, and EBSD analyses

The results of the SEM and EDS analyses are presented in Figure 38. They show outcomes similar to those mentioned in the optical microstructure analyses. Additionally, ά-morphologies have been observed in the main grains at both sintering temperatures of 1200 °C and 1300 °C. However, the SEM and EDS results exhibited microstructures and chemical compositions close

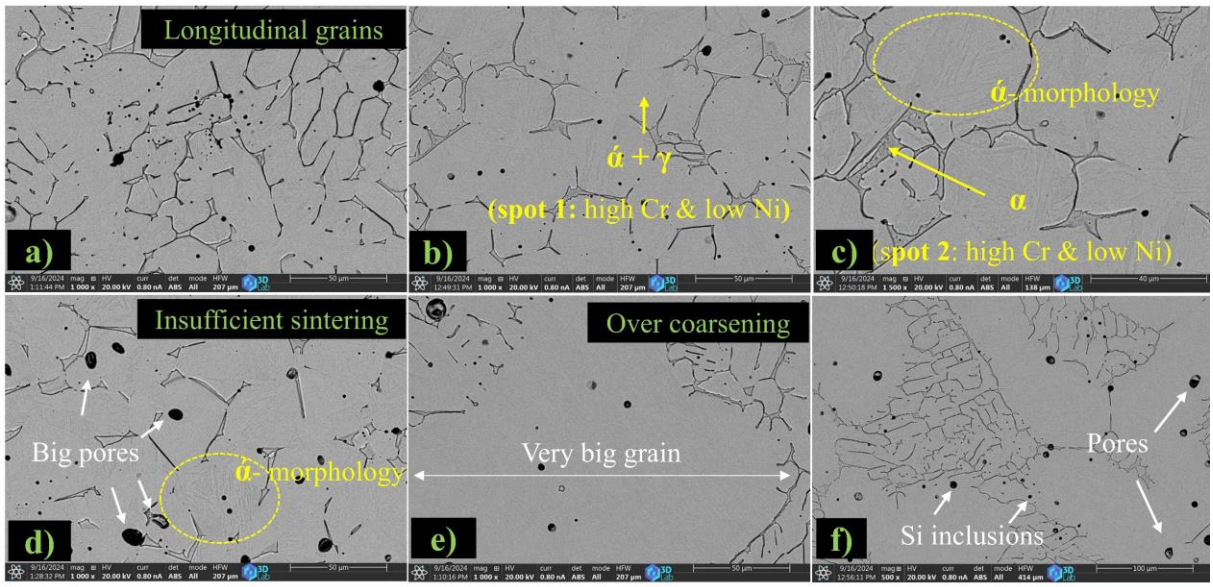

g)

Element by EDS	O K	SiK	MoL	CrK	FeK	NiK	CuK
Weight % (spot 1)	1.37	0.37	0.16	15.95	74.18	4.25	3.71
Weight % (spot 2)	1.43	0.44	0.23	22.34	70.57	2.45	2.54

h)

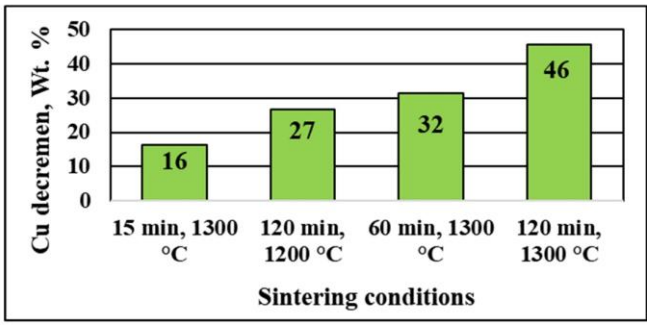

Figure 38. The SEM images and EDS analyses of INDS 17-4PH samples cold pressed at 1600 MPa and sintered at a) 1300 °C, 15 min., b and c) 1300 °C, 60-min (different magnifications), d) 1200 °C, 120-min, e and f) 1300 °C, 120-min (different magnifications). The EDS analyses of the spots in (c and b) are presented in (g). EDS Cu-decrement is presented in (h).

to those found previously in section 4.2. Two distinct regions can be identified: a bright phase (spot 1) and a dark phase (spot 2) across all samples, regardless of the sintering conditions. These spots reveal noticeable differences in the Cr and Ni contents in the bright phase region compared to the dark phase region. The high Cr spot corresponds to the α-region, while the high Ni spot corresponds to the ά+γ-region.

However, Cu was not evaporated during induction sintering, as reported in plasma sintering, due to the pressure of the sintering atmosphere [4]. The Cu wt.% decreased by approximately 32% in spot 2 (α-region) compared to spot 1 (ά+γ-region) at 1300 °C for 60 minutes. This was

attributed to the diffusion process, which allowed the Cu atoms to diffuse during δ-ferrite formation. This decrement ratio decreased with a reduction in sintering time (15 minutes at 1300 °C) to 16%, and to 27% with a decrease in sintering temperature to 1200 °C for 120 minutes. Conversely, it increased to 46% with an increase in sintering time to 120 minutes at 1300 °C.

The results of EBSD phase analyses are presented in Figure 39. These results revealed the presence of BCC and FCC structures. These structures refer to formation of ά + α and γ, respectively. The IQ and the phase map show clearly the ferrite distributions in grain boundaries and along with austenite grains (Figure 39 (a)). Additionally, these images show the distribution of γ in a mixed way with ά. Unfortunately, these analyses could not find the BCT structures, which are ά-phase, due to low carbon content of the 17-4PH powder as previously mentioned. However, the ά-morphology was approved using SEM analyses above. However, the EBSD results confirmed the increase of FCC (γ) with rising sintering temperature and time (Figure 39 (b)). The amount of γ-phase increased with longer sintering time. The γ-phase amounts were 5%, 6%, and 13% for the INDS samples sintered for 15, 60, and 120 minutes, respectively, at 1300 °C. Maintaining a long sintering time of 120 minutes while reducing the sintering temperature to 1200 °C also resulted in a large γ-phase amount of 12%. This can be explained as follows: the formation of δ-ferrite begins along γ grain boundaries at temperatures around 1260 °C [9]. This indicates that increasing the sintering temperature to 1300 °C facilitates the formation of more δ-ferrite. Consequently, extending the sintering time at elevated temperatures promotes the formation of both γ and δ-ferrite due to diffusion phenomena. As a result, the δ-ferrite transforms back to the γ-phase upon cooling, and then to α, which begins to form at 117.9 °C during cooling, according to the DCS results in section 4.2.2. Due to the absence of rapid cooling, there will be a large amount of α-phase and a specific quantity of untransformed γ-phase. The amount of untransformed γ-phase is, after cooling, highly proportional to the sintering conditions of time and temperature. This explains the previous results regarding the increments in shrinkage with increasing sintering temperature and time, as it correlates with the increase in BCC to FCC transformation upon cooling. This also clarifies the earlier findings of increased density in INDS 17-4PH samples, which were enhanced by δ-ferrite.

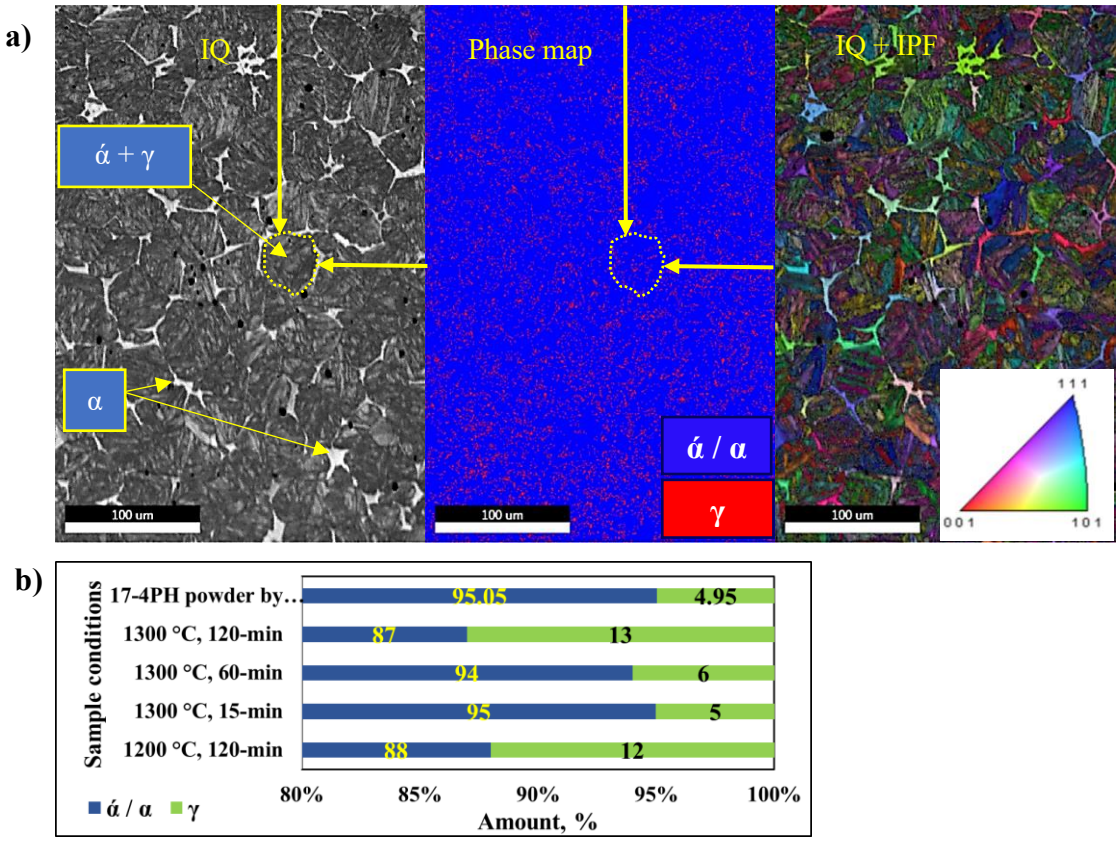

Figure 39. EBSD analysis results of (a) the IQ image and IPF map, and (b) the phases percentages of 17-4PH sample for cold pressed at 1600 MPa and sintered for 60 min.

4.4.5 Vickers hardness test

The effects of different manufacturing conditions on Vickers hardness are represented in Figure 40. Increasing cold pressing from 1000 to 1600 MPa increased the HV from 300 ± 24 to 344 ± 6, respectively. This happens, basically, due to decreasing of porosity. Additionally, the hardness raised from 299 ± 13 to 312 ± 15 HV with increasing sintering temperature from 1200 to 1300 °C (for two hours of sintering), respectively. Moreover, increasing sintering time from 15 to 60 minutes (at 1300 °C), raised the hardness from 313 ± 14 to 344 ± 6 HV due to decrease in porosity and high content of austenite, which considered as an alternate of ferrite-microconstituents. Finally, the highest HV was 344 ± 6 for samples manufactured at 1600 MPa of cold pressing, two minutes of holding time, and sintered at 1300 °C for 60 minutes. This hardness value dropped to 312 ± 15 HV with increasing sintering time from 60 to 120 minutes due to grain coarsening and high content of martensite to austenite transformation. It's obvious that austenite has lower hardness than martensite.

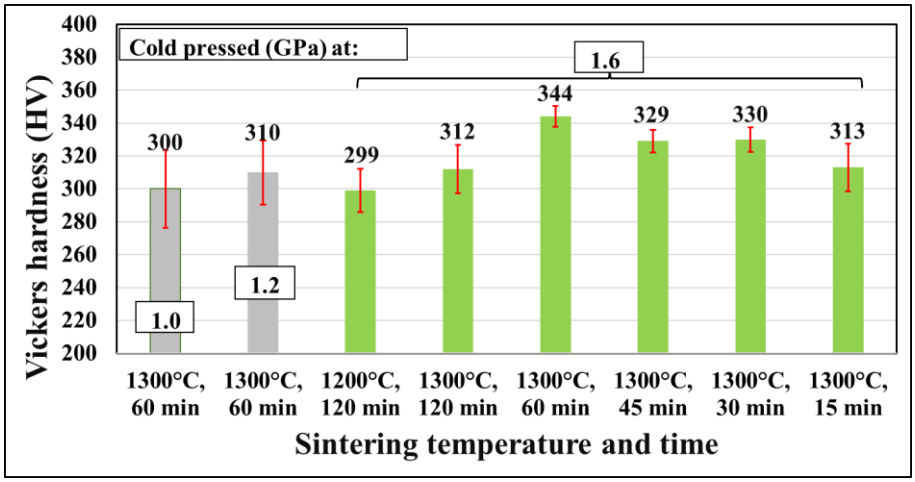

Figure 40. Represents the effect of sintering temperature and time on hardness of 17-4PH samples, held for 2.0 min under different cold pressing.

4.4.6 Compressive strength test

The stress-strain curves of compression tests of selected 17-4PH samples are presented in Figure 41(a). The curves behave similarly, except the enhancing due to increasing cold pressing and sintering temperature and time. This enhancement can be seen clearly in the yield strength results, which are depicted in Figure 41 (b). Increasing cold pressing from 1000 to 1600 MPa enhanced the compressive yield strength from 902 ± 49 to 1003 ± 11 MPa (around 8%), respectively, for samples sintered at 1300 °C for 60 minutes. Raising sintering temperature from 1200 to 1300 °C increased the compressive yield strength around 942 ± 25 to 961 ± 16 MPa (around 2%). Additionally, it increased from 935 ± 20 to 1003 ± 11 (around 4%) with extending sintering time from 15 to 60 minutes. Moreover, the compressive yield strength decreased to 961 ± 16 MPa with further increasing sintering time to 120 minutes due to grain coarsening and austenite increments compared to the martensite. This also was approved by the EBSD phase results, which showed almost similar content of austenite in both samples sintered at 1200 °C and 1300 °C for 120 minutes. The little increment of compressive yield strength in samples sintered at 1300 °C compared with that sample sintered at 1200 °C is a result of decreasing porosity ratio in the first case sample. However, the optimal compressive yield strength that could reached is around 943 MPa after seven hours of conventional sintering at 1200 °C (the sample was cold pressed at 1600 MPa), as found in section 4.2.7.

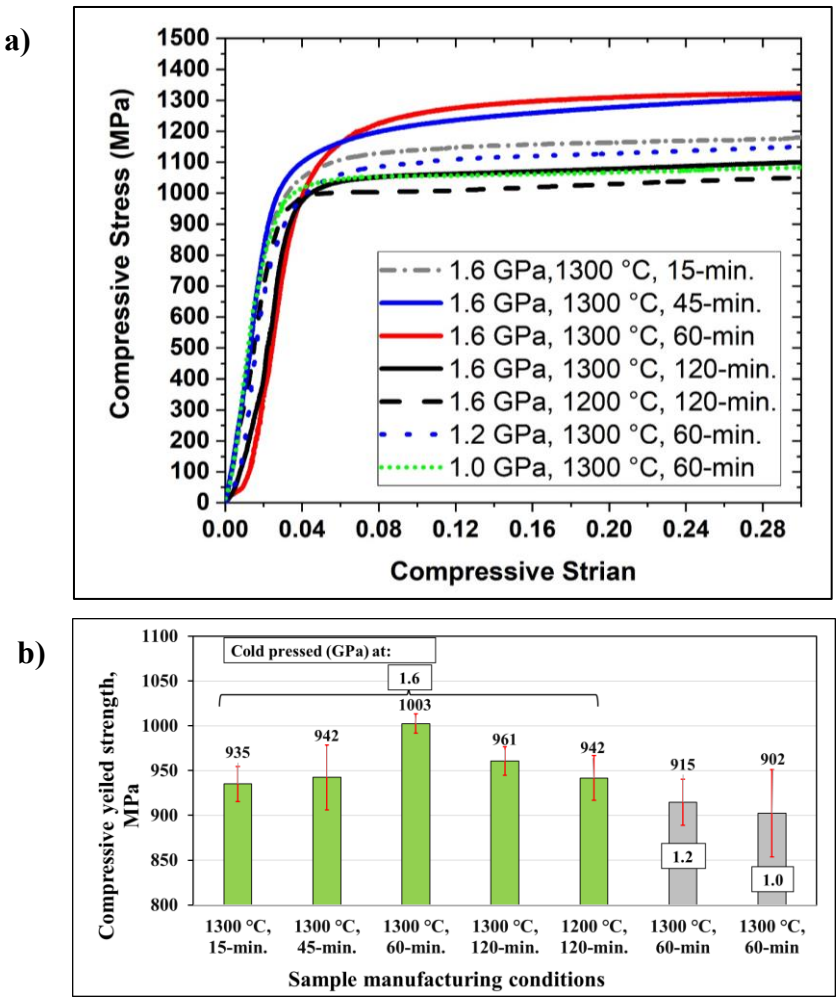

Figure 41. Represents a) the compressive stress-strain behaviors, and b) the compressive yield strength of 17-4PH samples manufactured at indicated conditions, using 2-min of holding time.

4.4.7 Summary

The report examines the impact of the compaction process and induction sintering on the characteristics of 17-4PH. The tests focused on analysing the effects of various cold pressing and sintering factors, such as cold pressing, sintering time, and sintering temperatures. The measurement of densification was conducted using both dimensional and Archimedes methods. The porosity results were validated using ImageJ analysis. The measurement of Vickers hardness has also been conducted. An evaluation of the strength characteristics was conducted by a compression test. Increasing cold pressing from 700 to 1600 MPa had a lower effect on improving sinter densities compared to the sintering temperature. According to the ImageJ and densification results, the cold pressing has the biggest effect on induction sinter density compared with sintering temperature and time (4%), sintering temperature 1200 to 1300 (2%),

and there was no noticeable difference between the density of samples sintered at one and two hours. While increasing sintering temperature from 1200 to 1300°C raised the sinter density around 2.5%, for 17-4PH samples cold pressed at 1600 MPa, held for 2 min, and sintered for 120 min. Sintering at 1200 °C leads to incomplete of sintering and high porosity. While sintering at 1300 C for 60 minutes is the best option for sufficient sintering process and regular pores. Extending sintering time to 120 minutes led to grain growth and low mechanical properties (the HV10 decreased to of 312, and compressive yield strength to 961 MPa). Increasing sintering time from 15 to 120 min had a little effect on improving sintered densification with around 2 % for 17-4PH samples cold pressed at 1600 MPa and sintered at 1300°C. The unique combination of full density and high mechanical properties, of 17-4PH sample has been made by applying 1600 MPa of cold pressing, 2 min of holding time, and1300°C for 60 min. With density of 98.79 ± 0.4 %, HV10 of 344, and compressive yield strength of 1003 MPa. The Cu did not evaporate during induction sintering; however, it diffused alongside the formation of δ-ferrite. The Cu-content in the α-region increased with rising sintering temperature and times. The EBSD results approved the increment of FCC (γ-phase) with increasing both sintering temperature and time. The amount of untransformed γ-phase after cooling is closely related to its amount during heating, owing to the sintering conditions of time and temperature.

4.5 Results of optimisation SLM conditions

The goal of this dissertation work is to evaluate the SLM process for the production of optimised SLM 17-4PH parts. To thereafter (in section 4.6) compare the physical-mechanical properties of the 17-4PH parts produced through both conventional and induction sintering methods using a heat-treatment condition. It is fascinating to examine 17-4PH parts produced by various metallurgical processes; specifically, the SLM melting mechanism differs significantly from the sintering mechanism.

4.5.1 Optical microstructures and PP results

The unetched optical microstructure results of scan voids (subsurface voids) formation on the longitudinal sectional surfaces of different SLM samples are presented in Figure 42. The scan voids are clearly visible in the 1SLM sample on only two sides, indicating they are not present on the other two sides of the cut section of the sample. These voids disappeared particularly in the case of the 2SLM sample. This indicates that both the scanning strategy and enhanced energy density have a greater impact on the elimination of subsurface void formation. However, various

studies have attributed this effect to other factors. For instance, the scan voids were identified as a result of adding a closing contour, which is considered unavoidable (a machine-specific parameter) [100]. Another reason these voids were significantly observed is due to the increased

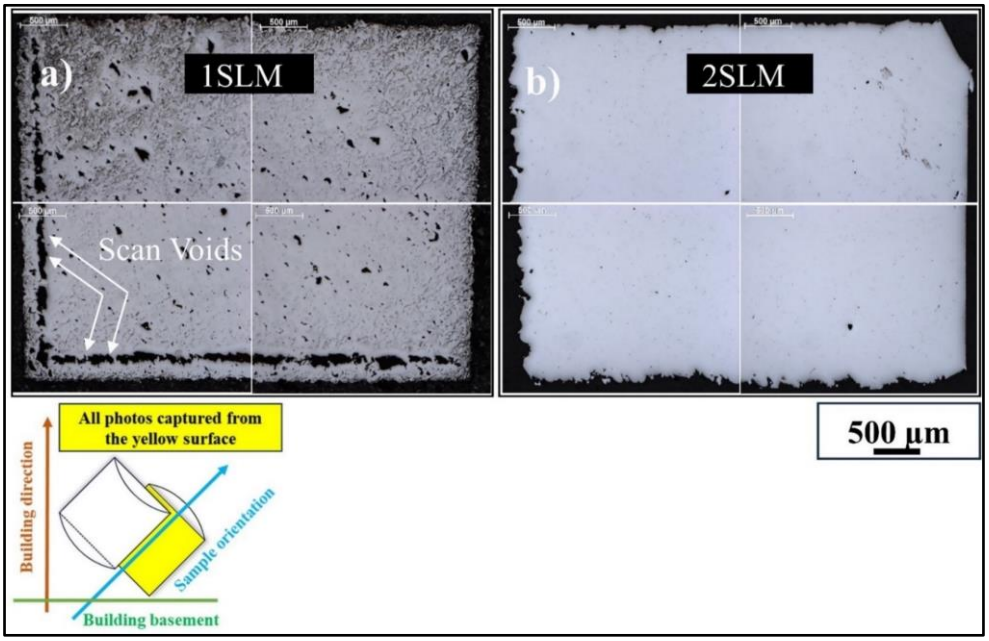

Figure 42. Illustrates the effect of the scan strategy on the formation of scan voids on the sectional surfaces of a) 1SLM, b) 2SLM, and c) 3SLM samples.

space between hatch scan tracks and contour tracks, from 0.03 to 0.10 mm [88]. Both are valid reasons if the voids are present on all four sides, not just two sides, of the cut section of the 1SLM sample. Therefore, these reasons are insufficient to explain void formation in the current dissertation work because the contour value and space were set to 2 and 0, respectively, meaning the contour was added and the space was reduced to 0 in both 1SLM and 2SLM samples. Furthermore, the formation of scan voids near the contours may, in some cases, be attributed to the mitigation strategy, where the laser spot slows before turning around, causing an increase in power density that results in keyhole pore formation at the end of scan tracks [120]. This reason is closely related to the formation of scan voids in this desertion work. This desertion work could be mitigated by selecting an appropriate scanning strategy and specifying suitable parameters for optimal energy density, a complex process that depended on a comprehensive literature analysis. The zigzag scanning strategy frequently alters the scanning direction. This helps distribute the input heat across different starting and ending sides of each printed layer, which

reduces the multiple overlaps in the same region caused by the normal scanning strategy. Overlapping in the same area can lead to increased gas entrapment and void formation.

However, the results of scan voids formation on the top surfaces of 1SLM and 2SLM samples are shown in Figure 43. No scan voids are observed on the top of the 2SLM sample, while the scan voids are clearly visible on the top of the 1SLM sample. Furthermore, due to the rotation of each printing layer and the sample orientation at 45 degrees, the scan voids are distributed longitudinally on the subsides and quarterly on the top surface. i.e., if there was no rotation after each scan layer, the scan voids will be shown on one side of the printed sample. Thus, the rotation mitigated the effect of high input energy per volume but the scan voids still shown on one side will show the scan angle. This indicates that these voids result from a significant energy input per scan volume, originating from the intersections of laser scans of accumulated printed layers.

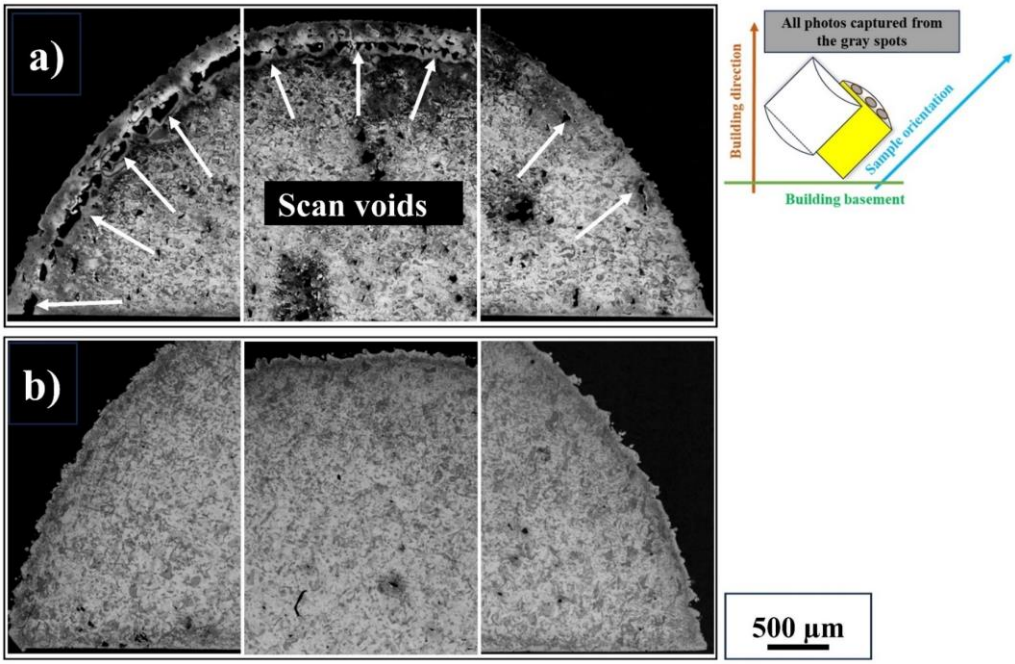

Figure 43. The effect of the scan strategy on the formation of scan voids on the top surfaces of a) 1SLM and b) 2SLM samples

However, the PP frequency results of the 1SLM and 2SLM samples microstructures are shown in Figure 44. The parameters of the 1SLM setup led to the formation of completely irregular and large pores, exhibiting a PP of 700 µm. In contrast, the optimised parameters reduced the PP and produced more regular pore shapes in the 2SLM samples, with a maximum PP of

approximately 120 µm. The types of pores and the reasons behind their formation will be detailed later.

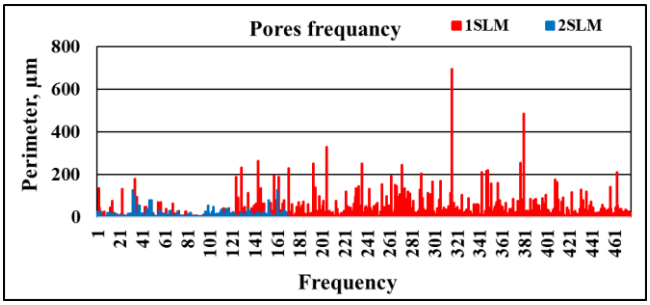

Figure 44. Shows the PP frequency of different SLM 17-4PH samples.

The optical microstructures of the longitudinal-sectioned SLM samples are shown in Figure 45. The microstructure of the 1SLM contained more pores (excluding the influence of subsurface voids) compared to the 2SLM sample. This was attributed to the lower energy densities applied per volume of the printing layer during the printing process of the 1SLM samples. This led to insufficient melting (unmelted particles), resulting in the formation of large pores with irregular geometries. A study indicates that reducing the energy density below the ideal limit can increase the overall porosity of 3D printed stainless-steel materials [121]. However, no significant keyhole pores or pores from insufficient melting were observed in the microstructure of the 2SLM samples, which was due to a very adequate input energy density. Additionally, the pores became more rounded and smaller, indicating some gas-entrapped pores with spherical geometries. Moreover, the prominent keyhole pores in the microstructure of the 1SLM sample are a result of the scanning strategy. Zigzag scanning strategy provides double the time consumed by the normal scanning strategy before reaching the starting spots (i.e., the normal scan strategy always starts from one side to the other, while the zigzag scan strategy alternates sides after each hatching-line) during laser printing. This reduces the input energy on a specific spot and prevents double melting in that area, which decreases porosity. However, keyhole mode porosity occurs when the energy density is excessively high, creating a vapor depression in the deep melt pool with high liquid flow velocity, which closes in on itself and traps vapors as the melt pool advances. Furthermore, all three types of pores (irregular pores due to unmelted particles, gas-entrapped pores with spherical geometry, and keyhole pores) were previously mentioned in[71], [88], [122].

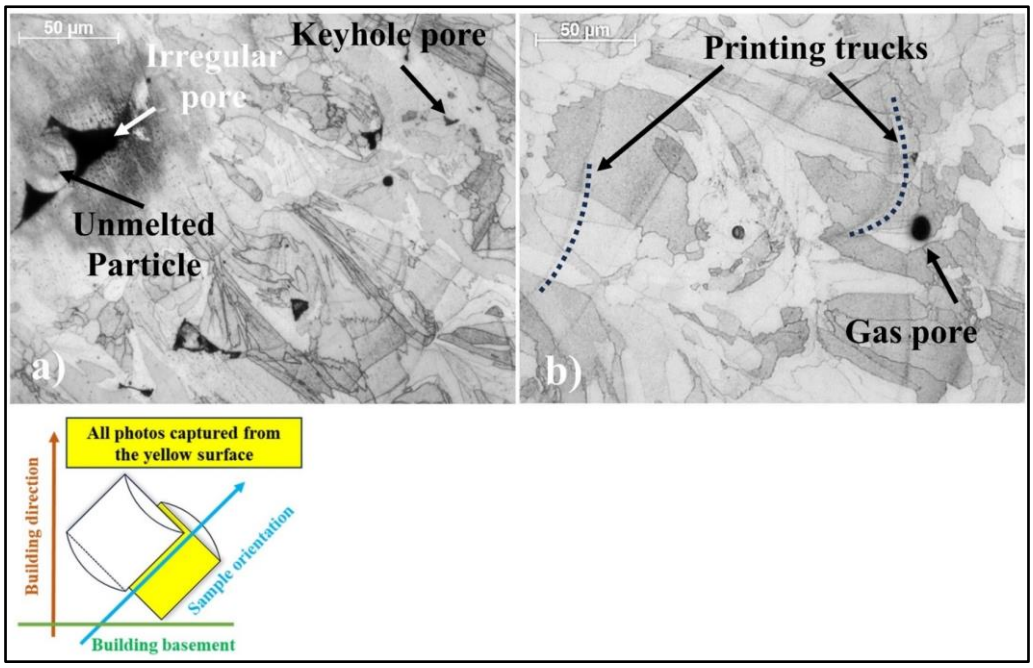

Figure 45. The optical microstructures of the cross-sectioned of a) 1SLM and b) 2SLM samples

Additionally, upon examination of the optical microstructures of the SLM samples, it is evident that the dark phase is observed to be combined with the lighter phases in a longitudinal manner. This phenomenon may arise from the melting mechanism and rapid cooling rate during the SLM process, which does not allow sufficient time for diffusion to occur as it does in the sintering process. It can be assumed that diffusion is negligible in the 17-4PH parts produced through additive manufacturing [123]. However, no evident grain boundary was observed, as the components were not solidified from a bulk liquid metal, which contrasts with the typical nucleation and growth process. Furthermore, the etching material attacked the melt pool boundary more, as shown in the microstructure. These findings are supported by previous work [71]. Additionally, it can be noted that the grain growth direction followed the heating source from the laser printing tracks, as found in[70], [71], [122].

4.5.2 Archimedes density measurements

The results of the relative density of both 1SLM and 2SLM samples are presented in Table 7. The relative densities for 1SLM and 2SLM increased from 94.82±0.37 to 98.85±0.10, respectively. The enhanced relative density in 2SLM sample was due to changing the scanning strategy from normal to zigzag and selecting appropriate energy density. Nevertheless, the effects of processing parameters on the characteristics of the SLM process have been

investigated in several papers. The results have shown a close connection between energy density, porosity, and microstructure[86].

Table 7. Shows the relative density of different SLM 17-4PH samples.

SLM sample	Relative density
1SLM	94.82 ± 0.37
2SLM	98.85 ± 0.10

4.5.3 EBSD, SEM, and EDS analyses

The results of the EBSD phase analysis for a 2SLM sample aligned with the build direction is shown in Figure 46 (a). It revealed the presence of BCC and FCC structures, which correspond to the formation of ά/α and γ, respectively. Due to the low carbon content of the 17-4PH material, identifying the BCT structures was challenging (see section 4.4.4). However, the content percentages of γ and ά/α were 1% and 99%, respectively. It was reported that the brief melting time and rapid cooling rates during the SLM process resulted in the formation of supersaturated

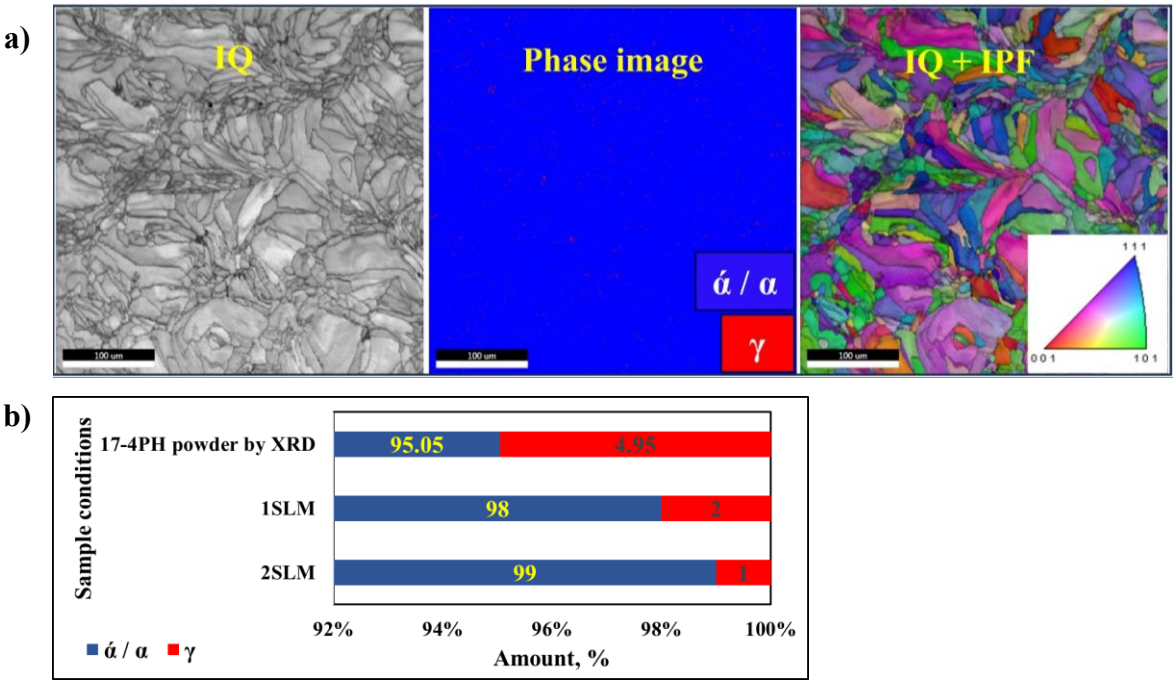

Figure 46. Represents a) EBSD analysis of the 2SLM, and b) the phases amount in different SLM 17-4PH samples

δ-ferrite and ά [75], [121]. Another study found that the microstructure of as-manufactured additive-manufactured 17-4PH parts consists of BCC (ά/α) crystal structure cells (or dendrite cores), surrounded by outer dendrite shells primarily composed of FCC (γ) crystal structures,

along with some remaining BCC crystal structures [123]. These findings are corroborated by the IQ image and the IPF map of this dissertation's results. Additionally, the IQ image and the IPF map did not display any distinct α-phase distribution areas due to the rapid cooling rate during the SLM process. Nonetheless, the ά morphologies were confirmed through the SEM results. Additionally, the amounts of different phases in all SLM samples are presented in Figure 46 (b). These results indicate a slight increase (1%) in the γ phase of the 1SLM sample compared to both the 2SLM sample.

The results of the SEM and EDS analyses of the 2SLM sample are shown in Figure 47. The entire microstructure displays a single scattered color region. This suggests the absence of distinct phases with varying atomic numbers. These findings are corroborated by the EBSD results, which revealed minimal γ and a substantial amount of δ-supersaturated and ά-phase. Additionally, no grain boundaries were observed, consistent with the optical microstructure results. However, the SE mode displayed the morphologies of melting pool boundaries, with parallel longitudinal neighboring dark and bright grains, as well as ά-morphologies. According to the EDS results, there are generally no significant differences in the wt.% of chemical elements between the dark and bright phases. The Cr, Ni, and Cu contents show nearly identical wt.% in both the bright and dark phases. This suggests that the dark and bright phases observed via the SE mode do not represent different phases with distinct crystal structures. These results are further validated by the EBSD findings, which confirmed that most of the microstructure of the SLM samples consists solely of a BCC crystal structure (ά/α phase). However, the ά-morphology was identified as a grain and needle-like structure without defined boundaries[70].

a)

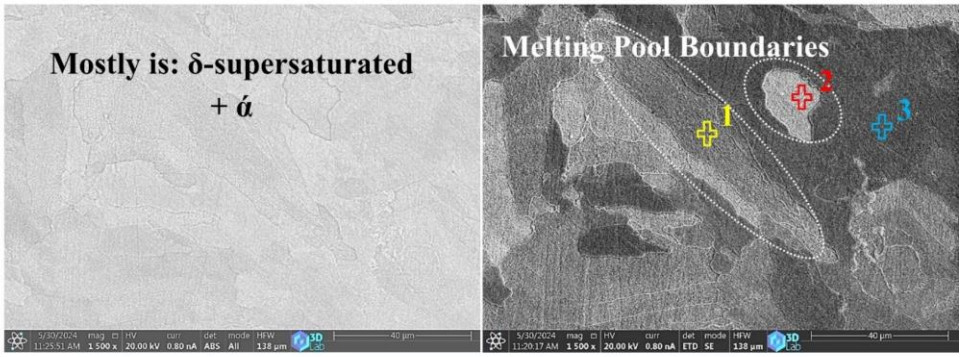

b)

Spot 1		Spot 2		Spot 3	
Element	Weight %	Element	Weight %	Element	Weight %
O K	1.16	O K	1.40	O K	1.17
SiK	0.53	SiK	0.58	SiK	0.57
MoL	0.25	MoL	0.18	MoL	0.37
CrK	16.84	CrK	16.73	CrK	16.85
FeK	73.57	FeK	73.13	FeK	73.32
NiK	3.97	NiK	4.16	NiK	4.07
CuK	3.68	CuK	3.81	CuK	3.65

Figure 47. The a) SEM (backscatter mode on the right, SE mode on the left), and b) EDS analyses of the 2SLM sample.

4.5.4 Vickers hardness test

The Vickers hardness results of both 1SLM and 2SLM samples are illustrated in Figure 48. It is evident that the variation among the different measuring positions (i.e., top surface, cross-section, and bottom surface) of 1SLM and 2SLM samples ranges from 5 to 10 HV. Consequently, due to the low HV deviation, the following discussion will concentrate on the cross-section results. The HV values recorded were 279 and 296 for 1SLM and 2SLM samples, respectively. There was a 6% increase in the HV result of the 2SLM compared to the 1SLM samples, attributed to reduced porosity. This increase did not come from the phases change, since the amount of ά/α and γ phases are similar in both 1SLM and 2SLM samples according to the EBSD results. The slight increase in the γ amount in 1SLM may have had a minimal effect on decreasing HV compared to the 2SLM samples. However, the results align with those reported in the literature. For instance, a study on the impact of varying laser power during the printing of SLM 17-4PH parts using a hexagonal scanning strategy with a layer thickness of 30 was conducted [85]. The findings indicated that the HV values were 276, 283, and 280 for different laser power printing parameters of 37.5 W, 38.5 W, and 39 W, respectively, indicating no significant differences. Shehata et al. measured microhardness values of 315 HV and 306 HV for tensile samples built horizontally and at a 45° angle to the build direction, respectively[124]. Additionally, the supersaturated δ-ferrite phase exhibits hardness values

comparable to the ά-phase of the 17-4PH 3D printed parts, according[75], [121]. This fact may have been the reason behind the similar HV deviation results of each individual SLM sample. Moreover, the ά-phase in the 17-4PH alloy has a very low carbon content and is therefore not as strong as martensitic phases in steels with higher carbon contents[121].

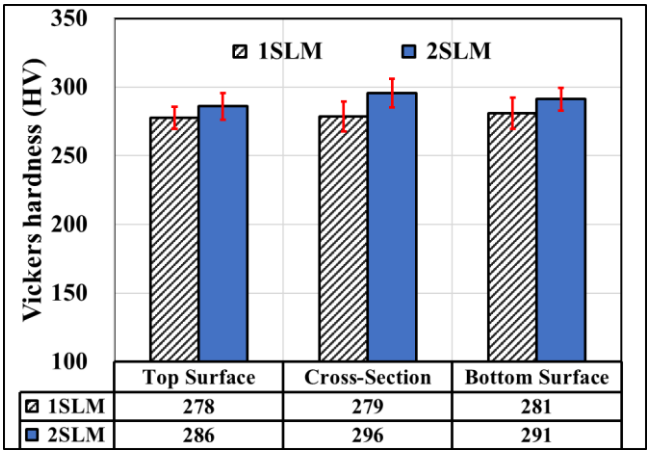

Figure 48. Shows the Vickers hardness of different SLM 17-4PH samples.

4.5.5 Compressive strength test

The results of compressive stress-strain tests and yield strength are presented in Figure 49 and in table 8, respectively. The curves for 1SLM and 2SLM samples exhibited similar behaviors. The compressive yield strength increased by approximately 14% after raising the energy density and altering the scanning strategy to zigzag (from 717 ± 14 to 818 ± 2 MPa from 1SLM to 2SLM, respectively). This improvement was primarily due to the elimination of porosity in the 2SLM samples compared to the 1SLM sample. However, it was noted that the compressive yield strength is 25% higher than the tensile yield strength of the SLM 17-4PH parts [70]. Manufactured SLM parts of 17-4PH material have a yield strength of 620 ± 30 MPa in the as-built condition [85]. This indicates that the compressive yield strength is equal to 775 MPa, according to the 25% rule. Furthermore, the compressive yield strength of the as-built SLM 17-4PH part was 625 MPa[125]. However, the tensile yield strength of SLM 17-4PH reached 712 ± 6 MPa with a relative density range of 96 - 98.46%, which corresponds to 890 ± 6 MPa as a compressive yield strength [100].

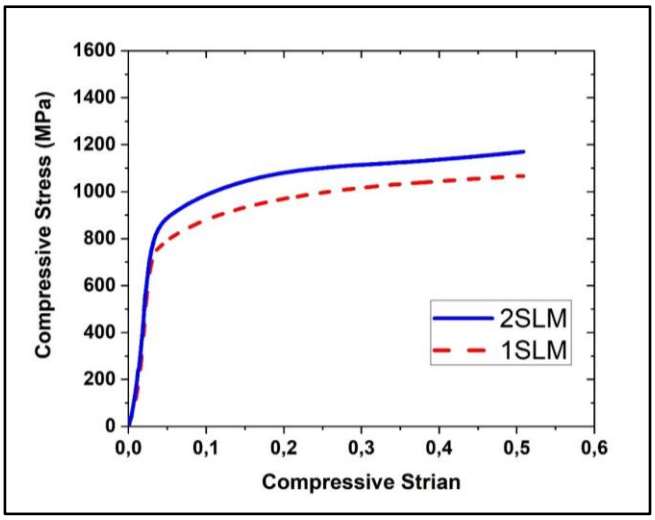

Figure 49. The compressive stress-strain curves of different SLM samples.

Table 8. The compressive strength of different SLM samples.

SLM sample	Compressive strength, MPa
1SLM	717± 14
2SLM	818 ± 2

4.5.6 Summary

The study investigates the effects of two distinct SLM processing setups. Densification was measured using the Archimedes method. The PP results were validated through ImageJ analysis. Optical, SEM, and EDS analyses were performed. Additionally, Vickers hardness measurements were conducted. Strength characteristics were evaluated through a compression test. The zigzag scanning strategy and the selection of appropriate energy density were the reasons for eliminating scan voids without altering the contour values and reducing the space between hatch scan tracks and contour tracks, as recommended by the literature. This strategy reduced the laser power density at the start of scan tracks compared to the normal scanning method. Raising the energy density from 36 to 48 J/mm² led to an 83% decrease in maximum PP. The relative density increased by 5% when employing the zigzag scanning strategy alongside increased energy density. The unmelted particle pores were observed in the optical microstructure of the 1SLM sample due to low energy density. These pores disappeared after increasing the energy density in the 2SLM sample. Keyhole pores were identified in the microstructure of 1SLM as a result of high energy density caused by the normal scanning strategy. Therefore, both energy density and scanning strategy must be selected carefully. However, the optical microstructures of all SLM samples contained melting pool boundaries instead of grain boundaries. This led to the columnar lath comprising dark and bright phases

intermingled with each other. The EBSD analysis confirmed the presence of BCC crystal structures (99%), corresponding to ά and α, along with 1% of FCC crystal structures (γ). However, the SEM analyses validated the presence of ά-morphologies. The backscatter image showed no differences in the concentrations of the dark and bright areas, as indicated by both the optical microstructures and the SE mode images. This suggests that the entire microstructure predominantly consists of one crystal structure. Furthermore, the EDS analyses revealed no significant differences in the weight percentages of chemical elements between the dark and bright phases, and they are comparable to those of the initial 17-4PH powder. This indicates that no significant diffusion process occurred and no evaporation took place either. There was a 6% increase in the HV values of the 2SLM samples compared to the 1SLM samples, attributed to the effects of altering the scan strategy and the appropriate energy density, which reduced porosity and consequently enhanced hardness. However, in comparison to the literature, this work achieved an improvement in the HV value of over 5%. The combination of a zigzag scanning strategy and the appropriate energy density resulted in an enhancement of the compressive yield strength of 818 MPa.

4.6 Results of application of H900 on different-methods 17-4PH samples

Generally, steel-manufactured parts undergo heat treatment before being used in their field of application. Thus, this dissertation work employed the H900 heat treatment condition, which is considered the best condition for achieving the approved strength properties of 17-4PH materials. Additionally, it used to compare the microstructural-mechanical properties of 17-4PH parts produced through both conventional and induction sintering methods against SLM 17-4PH parts. Nevertheless, the results of the manufactured CPCS samples, which were sintered at 1300 °C instead of 1200 °C (section 4.2), are included for comparison with the INDS samples.

4.6.1 Density and SEM results of CPCS sample

The results of the dimensional and Archimedes densities of the CPCS samples are presented in Table 9. The relative green and sinter densities are 91.51 ± 0.9% and 96.49 ± 0.05%, respectively. Compared to the previous densification results (section 4.2.1), it is evident that increasing the sintering temperature from 1200 °C to 1300 °C raised the relative sinter density by approximately 2% for a similar sintering time of one hour.

Table 9. represents the dimensional and Archimedes densities of the CPCS 17-4PH samples.

Relative green density	91.51±0.9%
Relative sinter density	96.49±0.05%

The SEM microstructure image is presented in Figure 50. It reveals numerous pores due to an insufficient sintering process. The SEM image clearly illustrates the ά-morphology. Furthermore, it depicts a dark region corresponding to the α-phase, while the bright region represents the γ + ά-phases, as indicated by the XRD analyses in section 4.2.2.

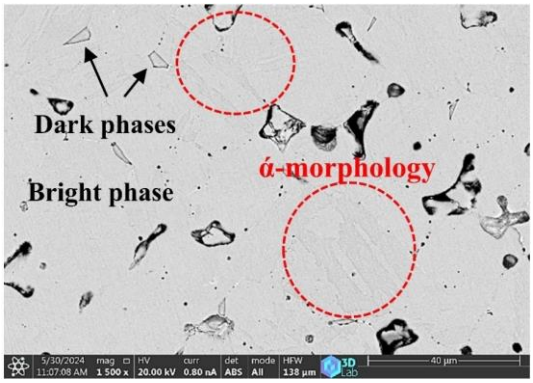

Figure 50. The SEM image of CPCS 17-4PH sample.

4.6.2 EBSD and SEM analyses of the HT samples

The EBSD results of the heat-treated 17-4PH samples are presented in Figure 51. They show comparable contents of FCC (γ) and BCC (ά/α) crystal structures for both HT-CPCS and HT-INDS samples. The amount of γ increased in the HT-SLM sample to 11% compared to 8% in the HT-CPCS and 7% in the HT-INDS. This increase may be attributed to the higher amount of retained austenite resulting from the increased carbon content in the recycled 17-4PH powder. The IQ and phase map clearly illustrate, particularly for the HT-CPCS and HT-INDS samples, the α-distributions between grain boundaries and alongside γ-grains. Additionally, these images depict the distribution of γ in a mixed manner with ά. However, there was no distinct α-phase in the HT-SLM sample. This is due to the fact that the microstructure of the 2SLM sample consisted of supersaturated δ-ferrite and ά prior to the heat treatment process (see section 4.5.3). Consequently, the maximum temperature employed in this heat treatment is significantly far from the melting temperature of the 17-4PH materials; thus, it cannot be expected that this heat treatment would completely alter the microstructure. Therefore, the α-distributions between grain boundaries can still be observed in the microstructures of the HT-CPCS and HT-INDS

samples, as they were present before the heat treatment application. For instance, it was noted that the microstructure of an AM 17-4PH part consisted of Cu-rich supersaturated martensite after solution treatment at 1040 °C for 1 hour, followed by quenching to room temperature [126]. Meanwhile, aging at 482 °C for 1 hour induced the precipitation of Cu-rich precipitates on the nanoscale. Another study found a predominant martensitic structure with 15% retained austenite in the microstructure of an AM 17-4PH that was solution heat treated only[123].

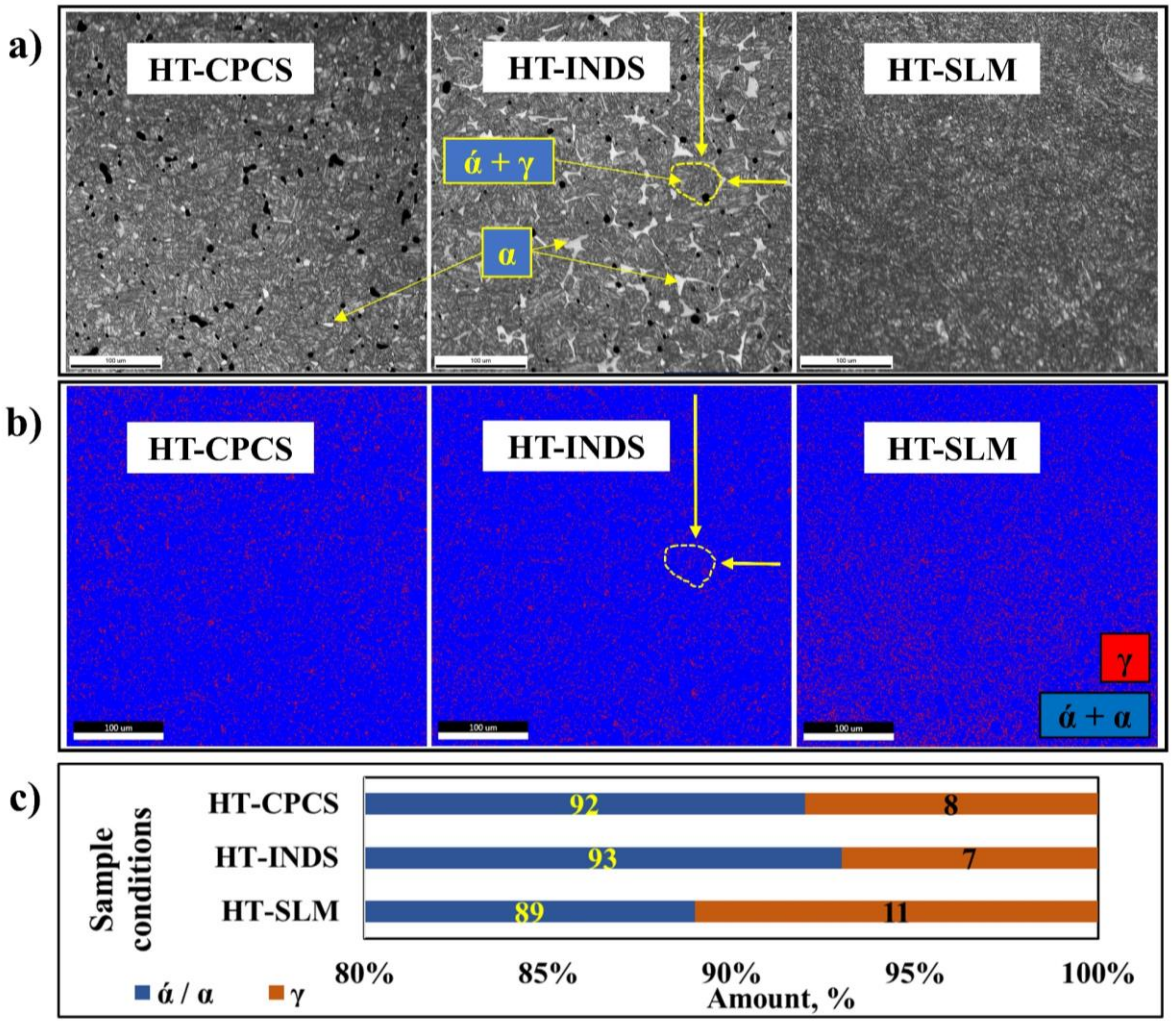

Figure 51. Showes a) the IQ+IPF images, b) the phases distributions, and c) the phases percentages of heat-treated 17-4PH samples.

Additionally, the EBSD grain size measurements are presented in Figure 52. These measurements indicate a slight decrease in the grain size of the HT-SLM sample compared to both the HT-CPCS and HT-INDS samples due to the refining process. The tops of the area fractions intersect with their grain sizes of approximately 5 µm, 6 m, and 10 m for HT-SLM,

HT-CPCS, and HT-INDS samples**.** The solution treatment at high temperatures facilitates the formation of grains/cells with boundaries, although the presence of a melting pool replaces the grain boundaries in the as-printed SLM 17-4PH samples (section 4.5). For instance, no traces of the melting pool were found in the microstructure of AM 17-4PH parts after the H900 condition [126]. However, the HT-INDS exhibited the highest grain size distribution among the other samples. This was due to the large grain size distribution of this sample prior to the heat treatment process. The maximum grain size of the INDS sample before heat treatment reached 40 microns (see section 4.4.3), whereas the CPCS sample exhibited a lower value due to an inadequate sintering process.

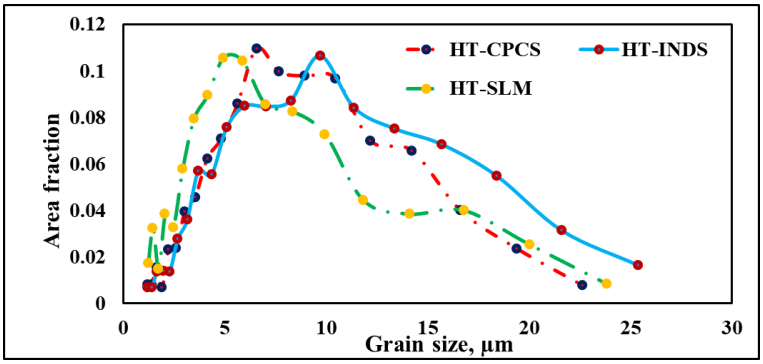

Figure 52. Grain size measurements of all heat-treated 17-4PH samples via EBSD analysis.

The SEM results of the all heat-treated 17-4PH samples are presented in Figure 53. The microstructure of HT-CPCS and HT-INDS samples exhibits similar α-regions between grain boundaries, retaining some features from their initial state before heat treatment. It can be clearly seen that the α-regions of the HT-INDS are larger than those of HT-CPCS. The HT-SLM microstructure exhibits no separate α-phase and a refined microstructure due to the application of heat treatment, which is similar to the microstructure of 17-4PH wrought materials according to [121]. These findings are confirmed by the EBSD results above. However, the HT-SLM microstructure showed no trace of a melting pool due to a solution treatment [123].

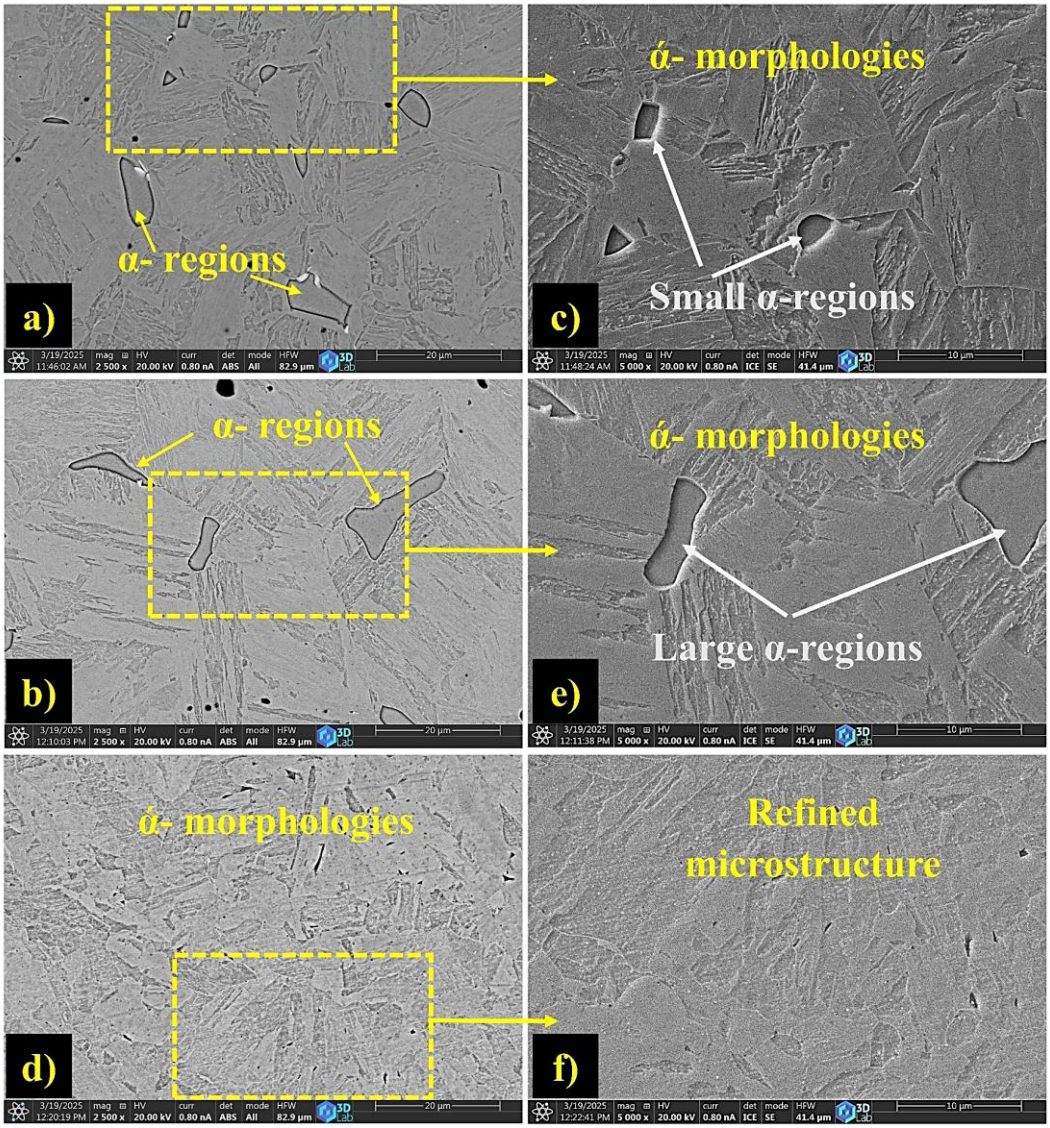

Figure 53. The SEM images of a) HT-CPCS, b) HT-INDS, and d) HT-SLM samples. c), e), and f) refer for the SE mode and higher magnifications of a), b), and c), recpectively.

4.6.3 HV and strength measurements of the HT samples

The effects of heat treatment conditions on the HV of the 17-4PH samples are illustrated in Figure 54. It is evident that the variation among the different measuring positions (i.e., top surface, cross-section, and bottom surface) is less than 5 HV. Therefore, the following discussion will focus on the cross-section results. The HV results indicate that the HT-SLM has a higher HV of 448 compared to the HT-CPCS (395) and HT-INDS (397) samples. This is primarily due to the porosity effects of the initial sample statuses (CPCS, INDS, and 2SLM) before heat treatment. It is common for heat treatment to have no noticeable effect on density. Thus, the CPCS sample exhibited the lowest density (96.49%) compared to both the INDS (98.79%) and

SLM (98.85%) samples (see sections: 4.4 and 4.5), with porosity increasing as density decreases. Additionally, the α-regions reduced the HV values of the HT-CPCS and HT-INDS samples compared to that of HT-SLM. According to the SEM results, the α-regions are larger in the case of HT-INDS compared to HT-CPCS samples. This may decrease the HV of the HT-INDS relative to that of HT-SLM, despite their comparable densification values.

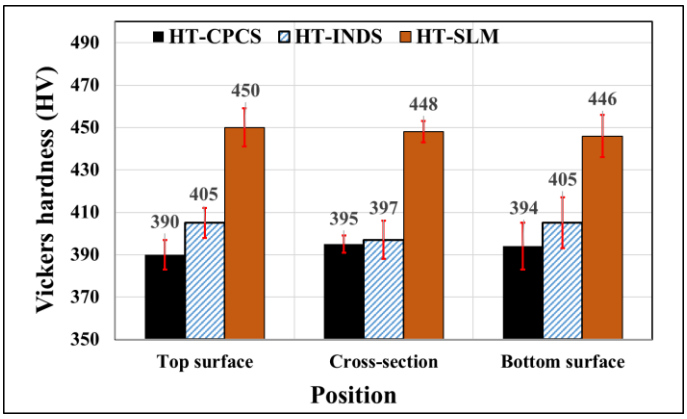

Figure 54. Represents Vickers hardness of all heat-treated 17-4PH samples

The results of compressive stress-strain tests are presented in Figure 55. The curves of all heat-treated 17-4PH samples exhibited similar behaviors. The compressive yield strengths results were 1195, 1218, and 1442 MPa for HT-CPCS, HT-INDS, and HT-SLM, respectively. This difference can be explained by three phenomena as follows: densification properties discussed in the above HV results; grain size; α-phase distributions; and residual carbon. It is common that heat treatment has no noticeable effect on density, as discussed previously. The grain size of the HT-SLM sample was the smallest compared to both HT-CPCS and HT-INDS samples, according to the EBSD results. A small grain size increases the number of grain boundaries, which act as obstacles for crack propagation. Furthermore, the presence of the α-phase between grains in both HT-CPCS and HT-INDS samples is clearly visible in separate regions. The α-phase has lower strength compared to the γ-phase and ά-phase, respectively [113]. These α-phase regions are absent in the microstructure of the HT-SLM sample. Therefore, this could be a primary reason for the significantly higher strength of the HT-SLM samples compared to the others. Additionally, the slightly higher carbon content of the recycled 17-4PH powder contributes to the increased strength of the HT-SLM sample, due to the increased ά-content as described in section 4.3. However, compared to the literature, after proper heat treatment, SLM parts of 17-4PH material have a yield strength of around 1100 MPa [85]. The compressive yield

strength is equal to 1375 MPa, according to the 25% rule in section 4.5.5, with a relative density of 99.85%. When applying H900 to SLM 17-4PH parts with a relatively low-density range of 96-98.46%, a tensile yield strength of 1190 MPa was achieved, which may correspond to a compressive yield strength of 1487 MPa [100]. However, this dissertation work produced both extremely high density and high strength HT-SLM 17-4PH samples. The refined microstructure, high density, and residual carbon contribute to the higher strength of the HT-SLM sample compared to that of the HT-CPCS and INDS samples.

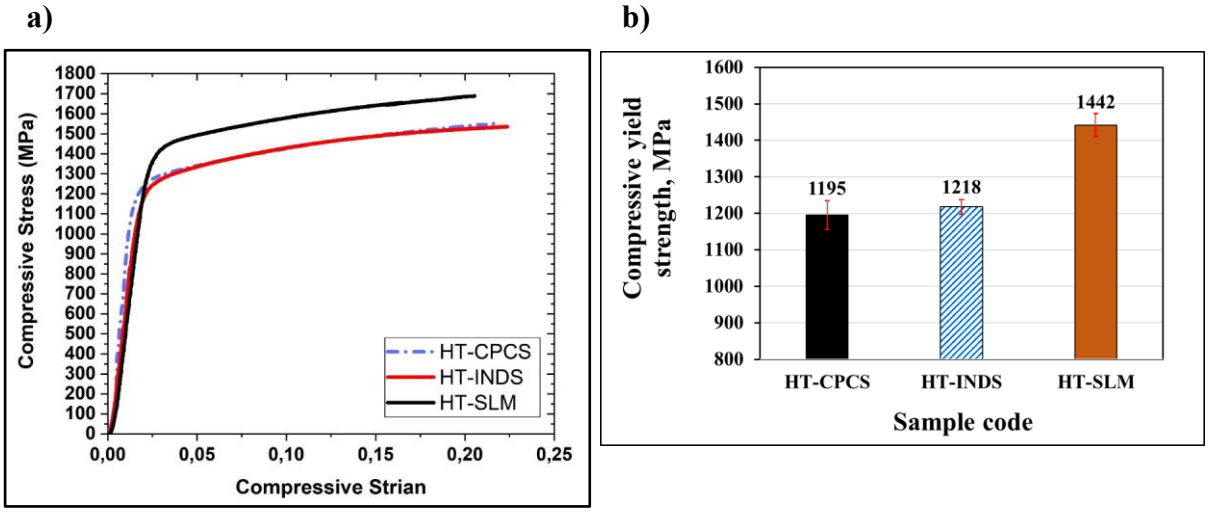

Figure 55. Represents a) the stress-strain curves, b) the strength all heat-treated 17-4PH samples

4.6.4 Summary

This dissertation work investigates the effects of applying H900 on 17-4PH samples produced by conventional and induction sintering (HT-CPCS, HT-INDS samples) and SLM (HT-SLM sample) methods. The SPCS sample was manufactured using conventional sintering at 1300 °C for 60 minutes. Densification was measured using dimensional and Archimedes methods. SEM analysis was performed. Additionally, EBSD analysis, Vickers hardness tests, and compression tests were conducted on the heat-treated samples only. Low density was observed in the CPCS manufactured sample. Additionally, numerous pores resulted from an insufficient sintering process, leading to the formation of small α-regions between grain boundaries. The SEM analysis revealed the presence of ά-morphologies.

However, the conclusions regarding heat-treated 17-4PH samples can be summarized as follows. The γ-amount increased by approximately 3% in the HT-SLM compared to both HT-CPCS and HT-INDS samples, attributed to the higher amount of retained austenite resulting

from the increased carbon content in the recycled 17-4PH powder. The IQ and phase map reveal α-regions between grain boundaries alongside γ-grains in both the HT-CPCS and HT-INDS samples. These images illustrate the distribution of γ in a mixed manner with α for all heat-treated samples. In contrast, there was no distinct α-phase in the HT-SLM sample. However, the SEM results of the heat treatment microstructures for all samples displayed clear α-morphologies. These findings indicate a refined microstructure and no evidence of a melting pool in the HT-SLM. The EBSD grain size measurements indicated a slight decrease in the grain size of the HT-SLM sample compared to both the HT-CPCS and HT-INDS samples due to the refining process. The tops of the area fractions intersect with their grain sizes of approximately 5 µm, 6 m, and 10 m for HT-SLM, HT-CPCS, and HT-INDS samples. Furthermore, the high density, refined microstructure, and absence of α-regions in the HT-SLM contributed to its increased hardness and strength compared to the HT-CPCS and HT-INDS samples. Additionally, the slightly higher carbon content of the recycled 17-4PH powder can also be linked to these enhancements. However, this research of the current dissertation work produced both extremely high density and high strength HT-SLM 17-4PH samples. The refined microstructure, high density, and residual carbon contribute to the higher strength of the HT-SLM sample compared to that of the HT-CPCS and INDS samples.

4.7 Claims

All claims are based on a series of experiments conducted with original and recycled 17-4PH powders. These experiments employed various techniques such as PSM, INDS, and SLM. Additionally, the critical parameters for each method were included in these experiments, such as different cold pressing and sintering temperatures and times for both PSM and INDS methods, as well as energy density and scanning strategies for the SLM method. However, the claims below are based on assessed characteristics from densification measurements, microstructural analyses, and tests of mechanical properties.

Claim 1. Achieving high relative green (~ 92%) and sinter density (~ 98%) and minimal volume shrinkage of PSM 17-4PH materials (5.53%)

a.1 The relative green density increased from 80.20 ± 0.28 to 91.76 ± 0.18 % as the application of cold pressing rose from 800 MPa to 1600 MPa, see Figures C1.1 and C1.2. The application of 1600 MPa improved the relative green density by approximately 11% compared to the reported literature.

b.1 Seven hours of sintering time at electric sintering temperatures of 1200 °C improved the relative sinter density of the DCTT 17-4PH samples to approximately 98% (see Figure C1.2), which is 4% higher than what is reported in the literature with significantly higher sintering temperatures. It is important to note that 1260 °C was the minimum sintering temperature mentioned in the literature. The DCTT samples demonstrated a lower volume shrinkage of 5.53% (see Figure C1.3), which is 46% less than the reported literature. This reduction resulted from reducing the difference between relative green and sinter densities, as well as applying a relatively low sintering temperature of 1200 °C.

c.1 The linear regression equation, as indicated below and in Figure C1.2, can predict the relative sinter density of the DCTT 17-4PH samples based on various sintering times (from 0 to 7 hours) at 1600 MPa and 1200 °C. The linear regression equation: $y = 0.81x + 93.22$; y: relative sinter density by %; x: sintering time by hour.

d.1 The seven hours of sintering significantly lowered the γ-content to 0.12%, while the α/ά-content increased, as illustrated in Figure C1.4. The increase in BCC amount is linked to the α-phase, which decreased the porosity. Consequently, the DCTT samples achieved a higher HV (around 43%) and improved strength (approximately 10%) compared to the literature.

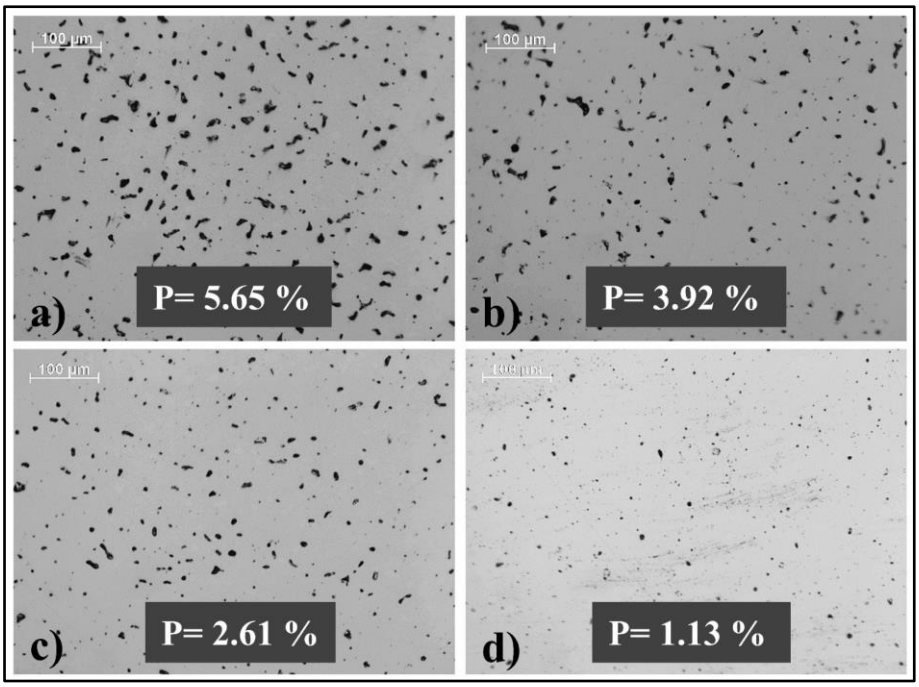

Figure C1.1. The impact of cold pressing on the optical microscopic ImageJ porosity of DCTT 17-4PH samples cold pressed at a) 800 MPa, b) 1000 MPa, c) 1200 MPa, and d) 1600 MPa after seven hours of sintering at 1200 °C.

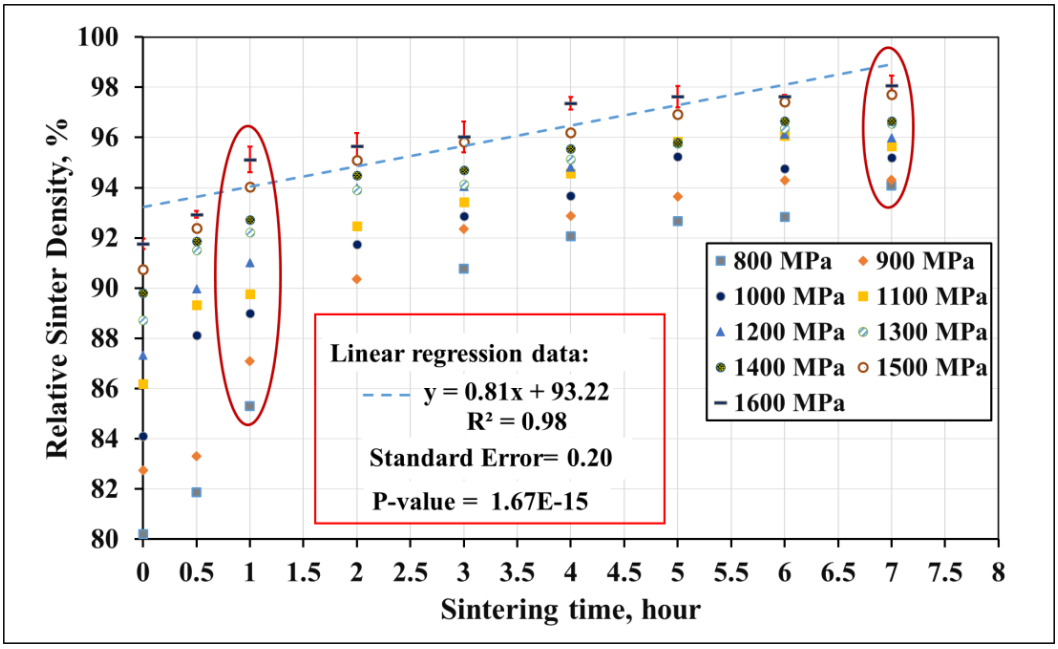

Figure C1.256. The impact of cold pressing and sintering time on the relative sinter densities of DCTT 17-4PH samples.

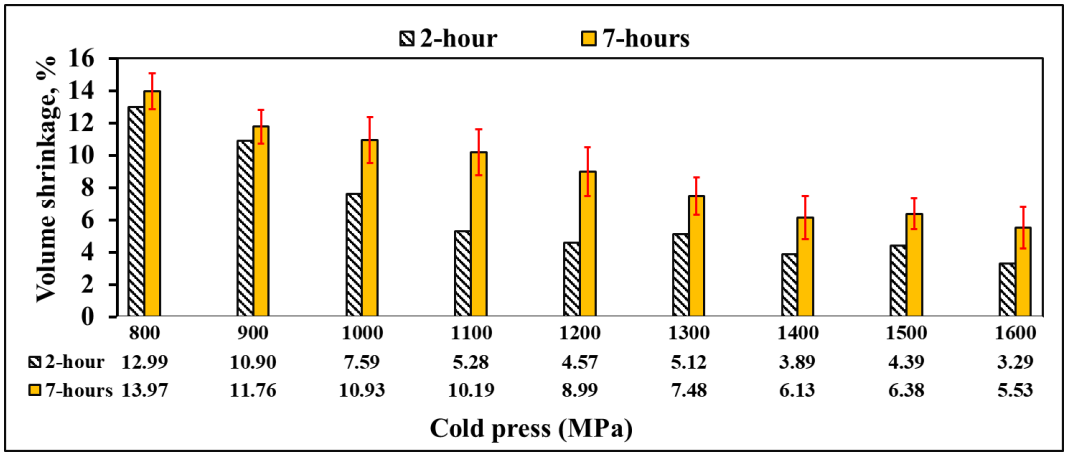

Figure C1.3. Volume shrinkage of selected DCTT 17-4PH samples sintered at 1200 °C for different times.

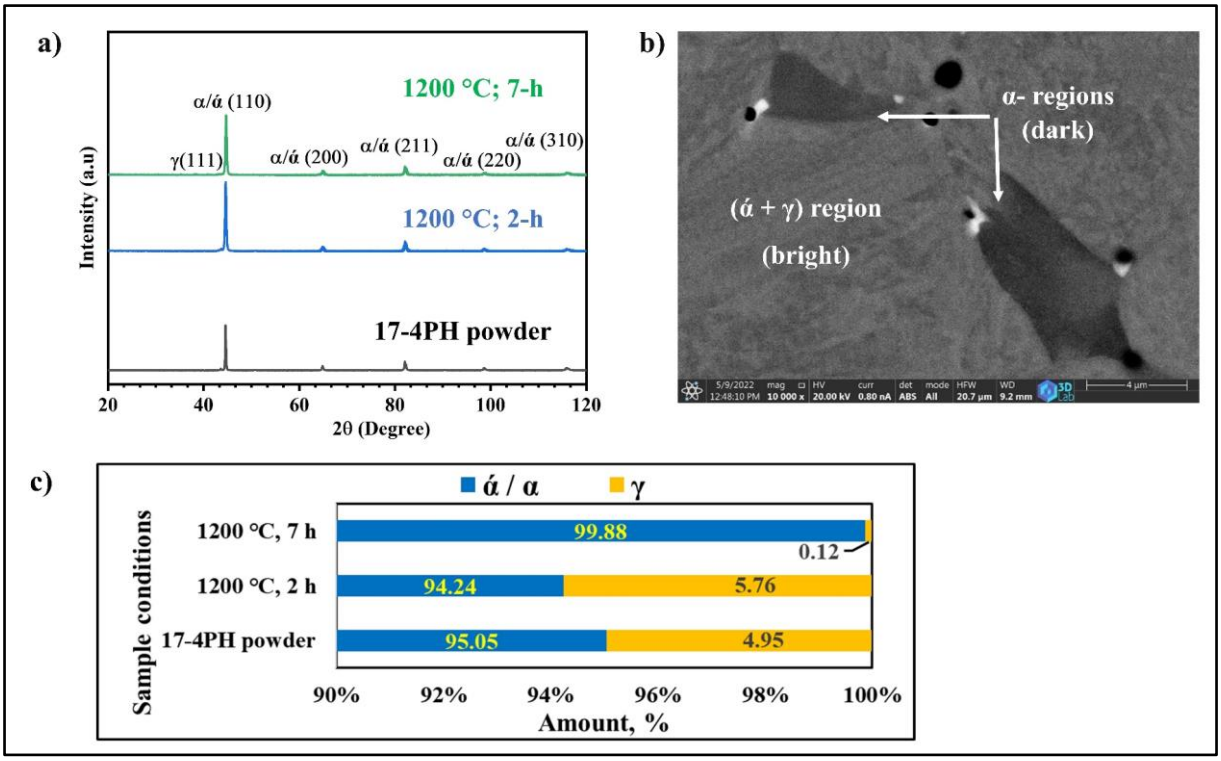

Figure C1.4. Illustrates a) the XRD diffractograms, b) the FIB-SEM image, and c) the phase amounts of DCTT 17-4PH samples. Note: The FIB-SEM image corresponds to a DCTT sample sintered at 1200 °C for two hours.

Claim 2. Steel powder of type 17-4PH produced through the 3D printing process is recyclable, and the powder metallurgical product created from it possesses suitable mechanical properties.

The recycled 17-4PH powder contained fused and welded particles, which are absent in the original 17-4PH powder. The recycled PSM 17-4PH samples exhibited a larger pore area (approximately double) compared to the original samples, as illustrated in Figure C2.1. The carbon content of the recycled 17-4PH powder (0.02%) was slightly higher than that of the original powder (0.01%). This was noted in recycled samples with a marginally increased martensitic content, as depicted in Figure C2.2. Consequently, the analyses of the recycled samples demonstrated a slightly higher strength (R1 with 917 MPa) compared to the original samples (O1 with 923 MPa), which can be considered negligible.

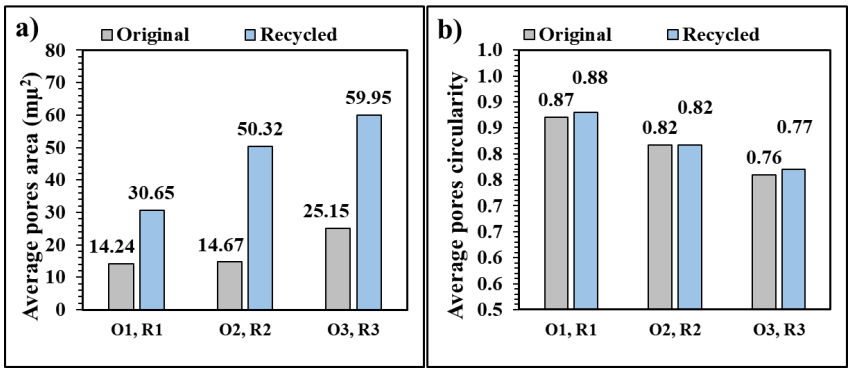

Figure C2.1. Represents a) average pores area, and b) pores circularity by ImageJ of unetched original and recycled samples.

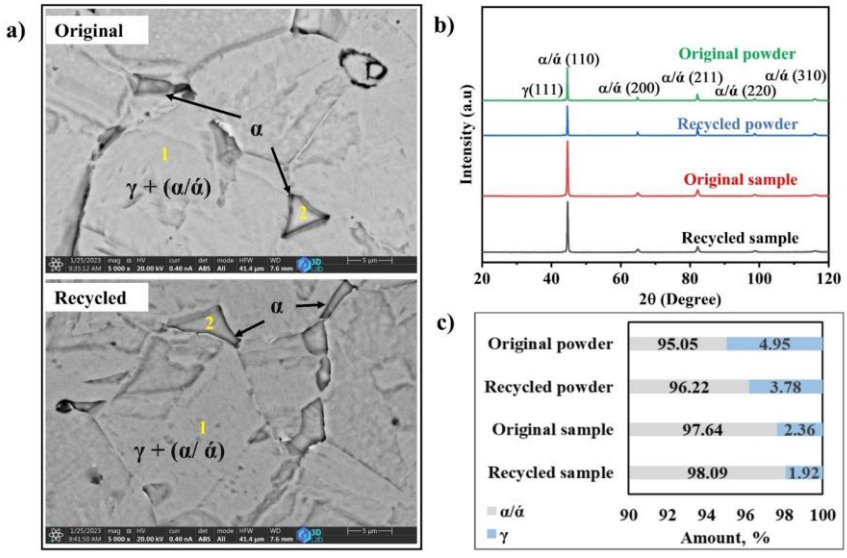

Figure C2.2. Phases approved by a) Backscattered-SEM images, b) XRD pattern, and c) XRD phases volume fraction of original and recycled samples.

Claim 3. Induction sintering produced 17-4PH parts with ~99% relative density after 1-hour of sintering instead of 7-hours by electrical sintering

a.3 Instead of long sintering time of seven hours using electrical furnaces in claim 1, induction furnace could achieve around 99% as a relative sinter density of INDS 17-4PH materials in one hour and at sintering temperature of 1300 °C. Sintering at 1200 °C, using induction furnace, led to incomplete of sintering and high porosity. The impact of cold pressing on enhancing relative sinter densities (by increasing relative green densities) was less pronounced in the case of induction sintering compared to electrical sintering (claim 1). The induction sinter density increased 4% with increasing cold pressing from 700 to 1600 MPa, 2% with increasing sintering temperature from 1200 to 1300 C, and 2% with increasing sintering time from 15 to 120 minutes (see Figure C3.1). There was no noticeable difference between the density of samples sintered at one and two hours. But 120 Minutes caused over coarsening, see Figures C3.2.

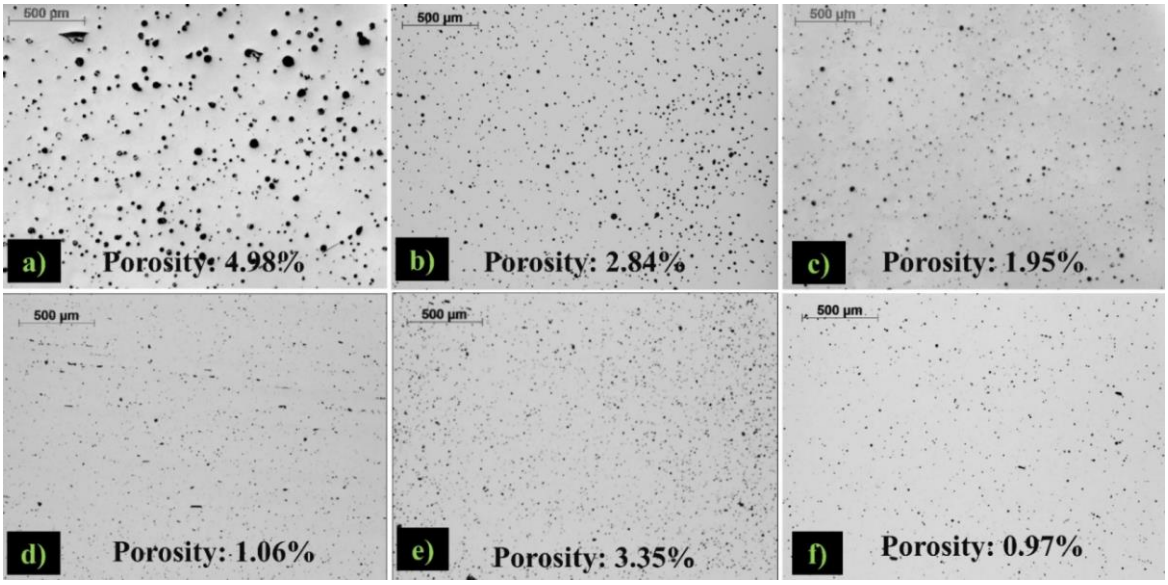

Figure C3.1. The ImageJ porosity 17-4PH optical microstructures manufactured at a) 1300 °C for 60 min at 700 MPa, b) 1300 °C for 60 min at 1000 MPa, c) 1300 °C for 15 min at 1600 MPa, d) 1300 °C for 60 min at 1600 MPa, e) 1200 °C for 120 min at 1600 MPa, and f) 1300 °C for 120 min at 1600 MPa.

a.3 The Cu did not evaporate during induction sintering; however, it diffused alongside the formation of δ-ferrite. The Cu-content in the α-region increased with rising sintering temperature and times, see Figure C3.2 (h). The Cu wt.% decreased by approximately 32% in α-region compared to ά+γ-region at 1300 °C for 60 minutes. This decrement ratio

decreased with a reduction in sintering time (15 minutes at 1300 °C) to 16%, and to 27% with a decrease in sintering temperature to 1200 °C for 120 minutes. Conversely, it increased to 46% with an increase in sintering time to 120 minutes at 1300 °C.

b.3 The FCC (γ-phase) increased from 5% to 13% with increasing sintering times from 15 to 120 minutes, see Figure C3.3. The amount of untransformed γ-phase (which can be retained austenite) after cooling is closely related to its amount during heating, influenced by the sintering times at 1300 °C. This might cause a decrease in mechanical properties during service due to the transformation to induced martensite.

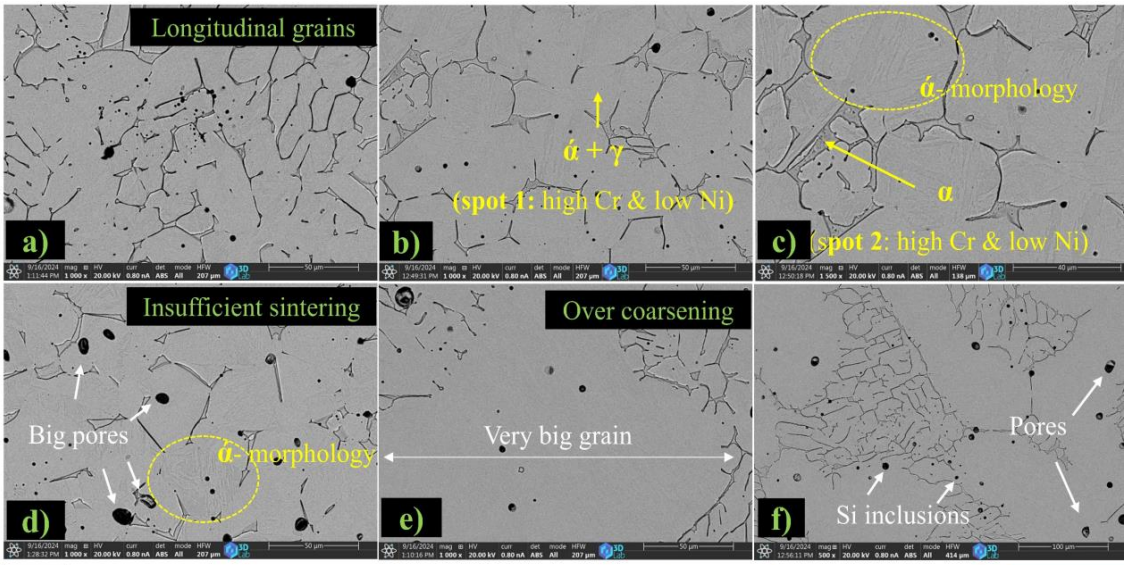

g)

Element by EDS	O K	SiK	MoL	CrK	FeK	NiK	CuK
Weight % (spot 1)	1.37	0.37	0.16	15.95	74.18	4.25	3.71
Weight % (spot 2)	1.43	0.44	0.23	22.34	70.57	2.45	2.54

h)

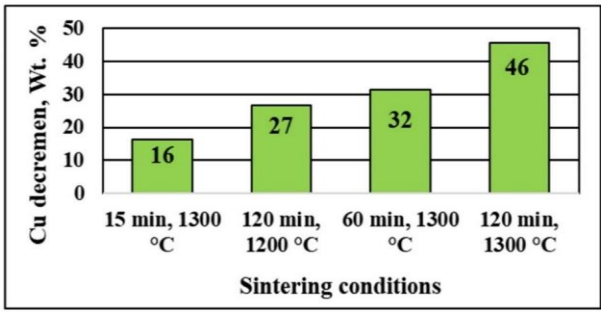

Figure C3.2. The SEM images and EDS analyses of INDS 17-4PH samples cold pressed at 1600 MPa and sintered at a) 1300 °C, 15 min., b and c) 1300 °C, 60-min (different magnifications), d) 1200 °C, 120-min, e and f) 1300 °C, 120-min (different magnifications). The EDS analyses of the spots in (c and b) are presented in (g). EDS Cu-decrement is presented in (h).

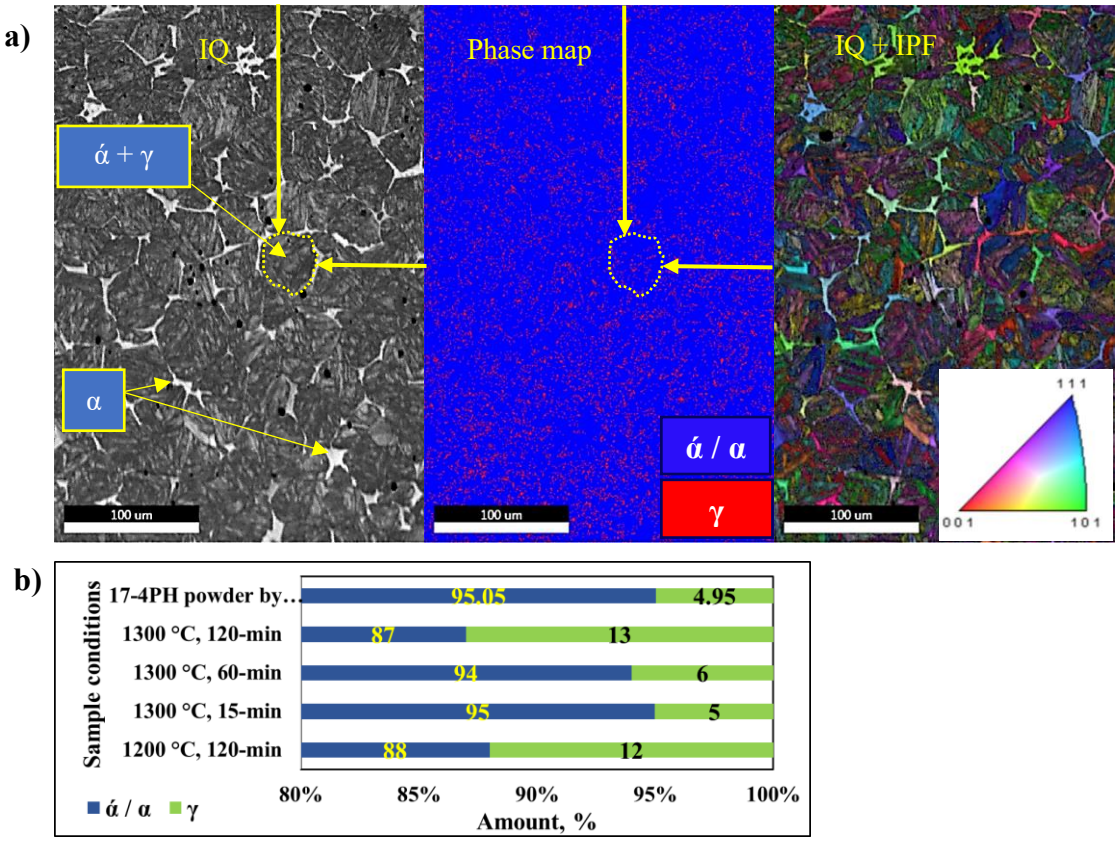

Figure C3.3. EBSD analysis results of (a) the IQ image and IPF map, and (b) the phases percentages of 17-4PH sample for cold pressed at 1600 MPa and sintered for 60 min.

Claim 4. Diminish scan voids and produce SLM 17-4PH parts with extremely high density and high mechanical properties

The zigzag scanning strategy and selecting appropriate energy density was sufficient to eliminate scan voids (see Figures 42 and 43) without altering the contour values and reducing the space between hatch scan tracks and contour tracks, as recommended by the literature. Utilising post-processing to remove the first voids shell from an SLM17-4PH sample may be considered unnecessary due to this achievement. However, in comparison to the literature, this work achieved an improvement in the HV value of over 5%, with a high compressive yield strength reaching 818 MPa.

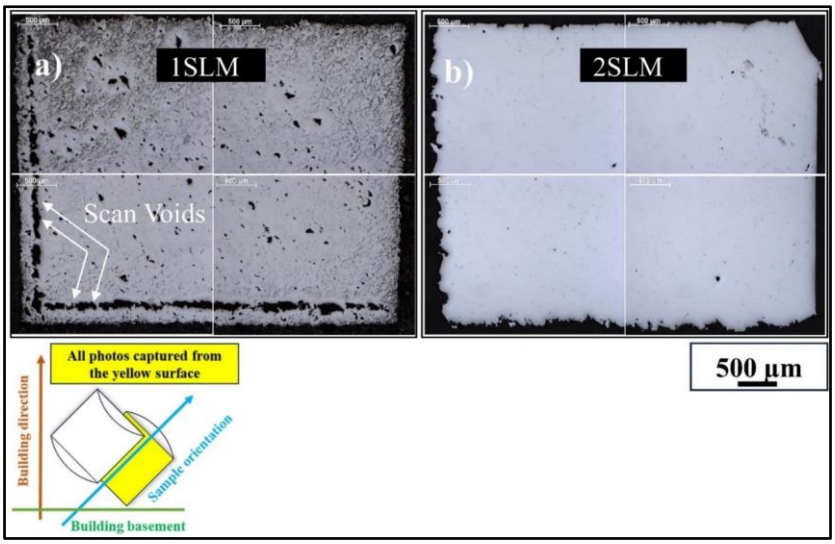

Figure 57. Illustrates the effect of the scan strategy on the formation of scan voids on the sectional surfaces of a) 1SLM, b) 2SLM, and c) 3SLM samples.

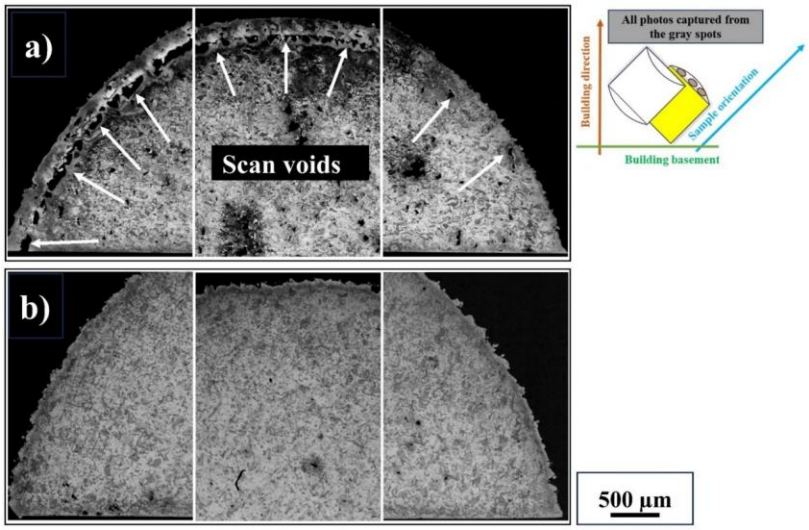

Figure 58. The effect of the scan strategy on the formation of scan voids on the top surfaces of a) 1SLM and b) 2SLM samples

Claim 5. Comparing between 17-4PH samples produced by conventional and induction sintering, and SLM methods by applying H900 condition

a.5 The γ-amount increased by approximately 3% in the HT-SLM compared to both HT-CPCS and HT-INDS samples (see Figure C5.1). This may be attributed to the higher carbon content in the recycled 17-4PH powder and the formation of retained austenite.

b.5 The final relative densities of the HT-INDS and HT-SLM samples were 98.79% and 98.85%, respectively. According to the SEM results (see Figure 53), the α-regions are larger in the HT-INDS case compared to the HT-CPCS, but are absent in the HT-SLM samples.

The grain size distributions of the HT-SLM sample were the smallest compared to both HT-CPCS and HT-INDS samples. The tops of the area fractions intersect with their grain sizes of approximately 5 µm, 6 m, and 10 m for HT-SLM, HT-CPCS, and HT-INDS samples. This confirmed by refined SEM microstructure of the HT-SLM sample, see Figure C5.2. All of the factors mentioned resulted in a lower HV for the HT-INDS (397) compared to that of HT-SLM (448), despite their similar densification values. The compressive yield strength, see Figure C5.3, of the HT-SLM was significantly higher (1442 MPa) than that of the HT-INDS samples (1218 MPa).

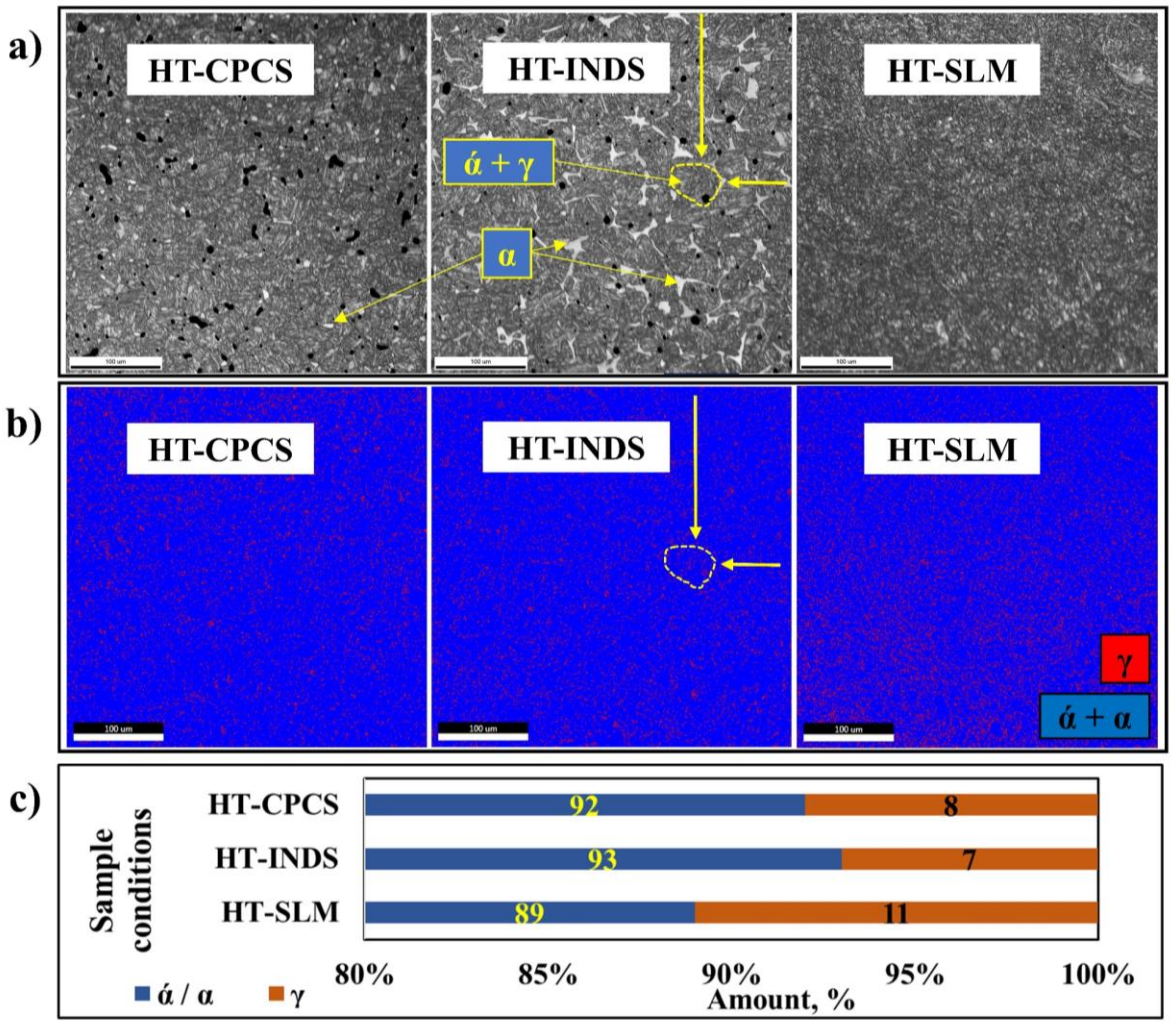

Figure C5.1. Showes a) the IQ+IPF images, b) the phases distributions, and c) the phases percentages of heat-treated 17-4PH samples.

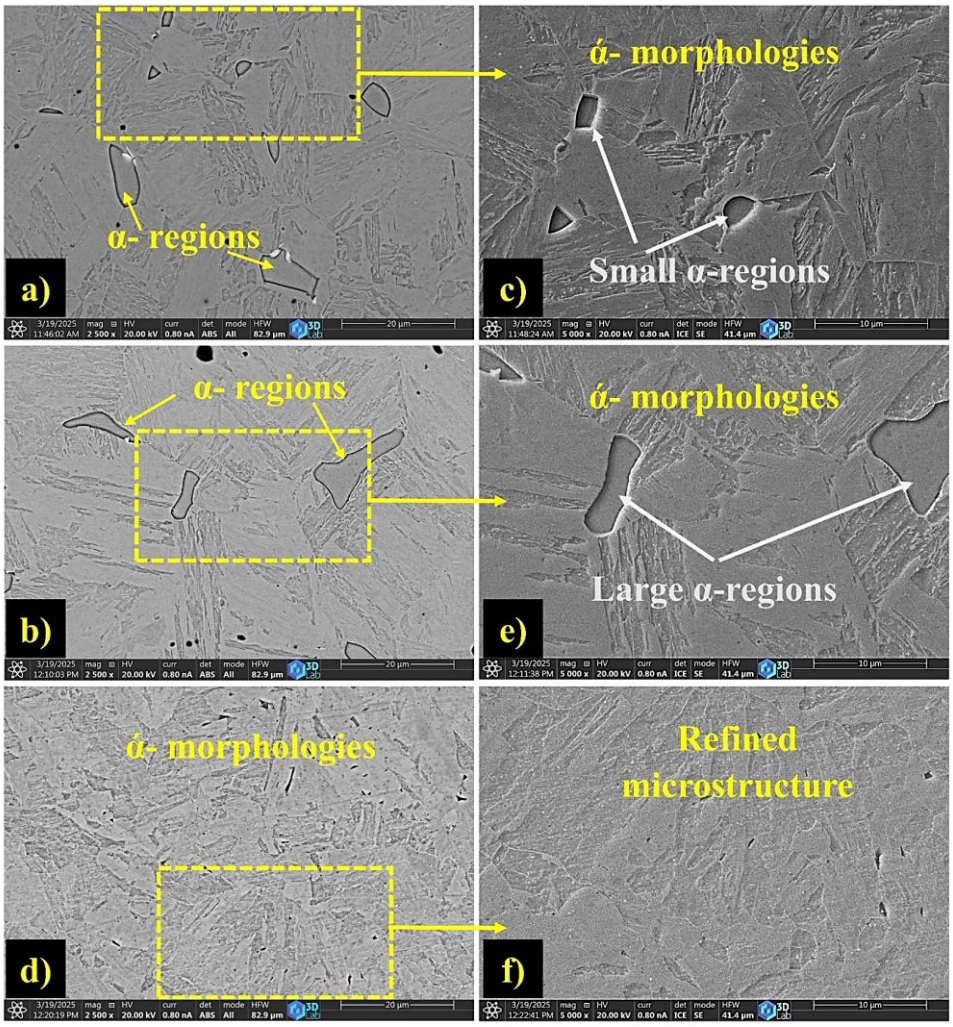

Figure C5.2. The SEM images of a) HT-CPCS, b) HT-INDS, and d) HT-SLM samples. c), e), and f) refer for the SE mode and higher magnifications of a), b), and c), recpectively.

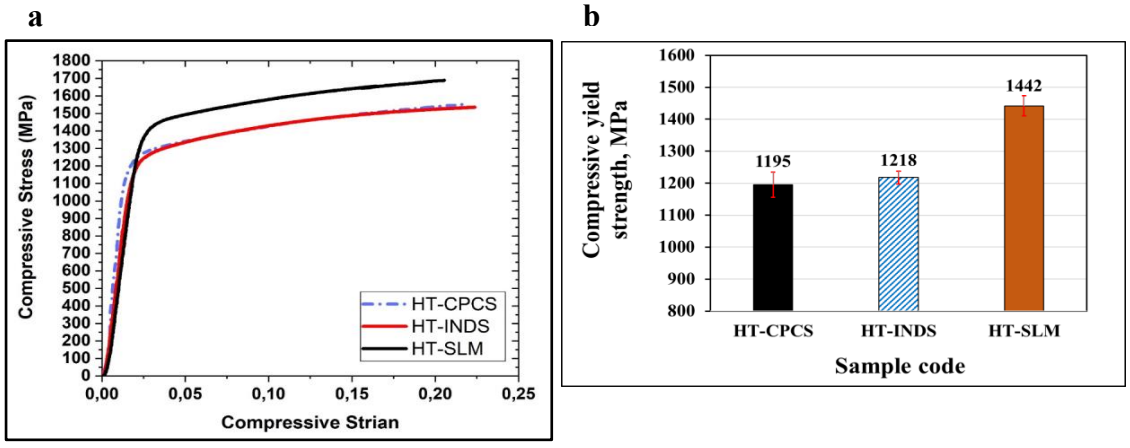

Figure C5.3. Represents a) the stress-strain curves, b) the strength all heat-treated 17-4PH samples

Author publications in the subject of the thesis

Journal paper

1- Kareem, Mohammed Qasim; Mikó, Tamás; Gergely, Gréta; Gácsi, Zoltán. A review on the production of 17-4PH parts using press and sinter technology. SCIENCE PROGRESS, 106: 1Paper: 003685042211460, 31 p. (2023). Independent citation: 4, *Journal Rank: Q1*

2- Kareem, Mohammed Qasim; Mikó, Tamás; Gergely, Gréta; Gácsi, Zoltán. Compaction behaviours of 17-4 PH, 316L, and 1.4551 stainless-steel powders during cold pressing. RESULTS IN ENGINEERING, 23: 102452, 8 p. (2024). Independent citation: 1, Journal *Rank: Q1*

3- Kareem, Mohammed Qasim; Mikó, Tamás; Gergely, Gréta; Gácsi, Zoltán. Optimisation of Powder Metallurgy Technology of 17-4PH Material. HELIYON, 11: 4: e42658, 15 p. (2025). *Journal Rank: Q1*

4- Mohammed, Qasim Kareem; Tamás, Mikó; Gréta, Gergely; Zoltán, Gácsi Choosing an Appropriate Additive Manufacturing Method for Printing 3D 17-4PH Parts: A Review. DOKTORANDUSZ ALMANACH.1, pp. 336-343., 8 p. (2022). Publication:33541234 Published Core Journal Article (Article) Scientific.

5- Kareem, Mohammed Qasim; Mikó, Tamás; Dávid Halápi; Gergely, Gréta; Gácsi, Zoltán. Employing Recycled 17-4PH Powder to Produce Press and Sinter Parts with Adequate Physical-Mechanical Properties. Submitted to RESULTS IN MATERIALS, *Journal Rank: Q2.*

Conference presentations

1. Mohammed, Qasim Kareem; Tamás, Mikó; Gréta, Gergely; Zoltán, Gácsi. Producing Cost-Effective Sintered 17-4ph Materials with High Physical and Mechanical Properties. The 17th Miklós Iványi International PhD and DLA Symposium 25-26 Oct 2021, Pécs, Hungary.
2. Mohammed, Qasim Kareem; Tamás, Mikó; Gréta, Gergely; Zoltán, Gácsi. The effect of applying massive cold pressing through conventional powder metallurgy on density of different stainless-steels compacts. In: Gökhan, GÜNDÜZ (eds.) Mediterranean International Conference on Research in Applied Sciences: The proceedings book Ankara, Turkey: İksad Yayınevi(2022) p. 62, Publication:33540745.
3. Mohammed, Qasim Kareem; Tamás, Mikó; Gréta, Gergely; Zoltán, Gácsi. Effect of Cold Pressing, Sintering Time, and Sintering Temperature on Densification of Press and Sintered 17-4PH Materials. (2022) microCAD Nemzetközi Multidiszciplináris Tudományos Konferencia 2022-10-13, Publication:33540797.
4. Mohammed, Qasim Kareem; Tamás, Mikó; Gréta, Gergely; Zoltán, Gácsi. Investigations of pressed and sintered components using 17-4PH powder collected in the chamber of an SLM printer Participated at the 23rd Annual Conference on Material Science -YUCOMAT 2022 which was held from 29.08 - 02.09.2022. in Herceg Novi, Montenegro, with Oral Presentation.
5. Mohammed, Qasim Kareem; Tamás, Mikó; Gréta, Gergely; Zoltán, Gácsi. Manufacturing of 17-4PH SLM Parts with Different Scanning Angles and Sample Orientations. Book of Abstracts from 9th International Scientific Conference on Advances in Mechanical engineering.Scientific Books of Abstracts, Vol. 2, pp 47-47 © 2023 Trans Tech Publications Ltd, Switzerland.

References

[1]-Ali S, Rani AM, Altaf K, Baig Z. Investigation of Boron addition and compaction pressure on the compactibility, densification and microhardness of 316L Stainless Steel. IOP conference series: materials science and engineering 344(1), 012023 (2018). doi:10.1088/1757-899X/344/1/012023

[2]-Acar AN, Ekşi AK, Ekicibil A. Effect of pressure on the magnetic and structural properties of X2CrNiMo17-12-2 austenitic stainless steel prepared by powder metallurgy method. Journal of Molecular Structure 15, 1198, 126876 (2019). doi:10.1016/j.molstruc.2019.126876

[3]-Kareem MQ, Dorofeyev V. Effect of fullerenes additions on physical–mechanical properties of hot-forged iron-based powder materials. IOP Conference Series: Earth and Environmental Science 877 (1), 012009 (2021). doi.org/10.1088/1755-1315/877/1/012009

[4]-R. Schroeder, G. Hammes, C. Binder, and A. N. Klein. Plasma Debinding and Sintering of Metal Injection Moulded 17-4PH stainless steel. Materials Research, 14 (4), 564–568 (2011). doi:10.1590/S1516-14392011005000082.

[5]- Bai, Yu, Lei Li, Leijie Fu, and Qiangfeng Wang. A review on high velocity compaction mechanism of powder metallurgy. Science Progress, 104 (2), 1–20 (2021). doi: 10.1177/00368504211016945.

[6]-B. Kozub, J. Kazior, and A. Szewczyk-Nykiel. Sintering kinetics of austenitic stainless steel aisi 316l modified with nanographite particles with highly developed bet specific surface area. Materials, 13 (20), 1–21 (2020). doi: 10.3390/ma13204569.

[7]-Cristofolini, Ilaria, A. Rao, Cinzia Menapace, and Alberto Molinari. Influence of sintering temperature on the shrinkage and geometrical characteristics of steel parts produced by powder metallurgy. Journal of Materials Processing Technology 210 (13), 1716-1725 (2010). doi:10.1016/j.jmatprotec.2010.06.002

[8]-S. Altıparmak, V. Yardley, Z. Shi, J. L.-I. J. of, and undefined 2020. Challenges in Additive Manufacturing of High-Strength Aluminium Alloys and Current Developments in Hybrid Additive Manufacturing. International Journal of Lightweight Materials and Manufacture, 4 (2), 246-261(2021).

[9]-Wu Y, German RM, Blaine D, Marx B, Schlaefer C. Effects of residual carbon content on sintering shrinkage, microstructure and mechanical properties of injection molded 17-4 PH stainless steel. Journal of materials science, 37, 3573-83 (2002). doi:10.1023/A:1016532418920

[10]-G. Singh, J. M. Missiaen, D. Bouvard, and J. M. Chaix. Additive manufacturing of 17–4 PH steel using metal injection molding feedstock: Analysis of 3D extrusion printing, debinding and sintering. Addit Manuf, 47, (2021).doi:10.1016/j.addma.2021.102287.

[11]-Zaky MT, Soliman FS and Farag AS. Influence of paraffin wax characteristics on the formulation of wax-based binders and their debinding from green molded parts using two comparative techniques. J Mater Process Technol, 209, 5981–5989 (2009).

[12]-H. Ye, X. Y. Liu, H. Hong. Sintering of 17-4PH stainless steel feedstock for metal injection molding. Materials Letters, 62(19), 3334–3336 (2008). doi: 10.1016/J.MATLET.2008.03.027

[13]-M. Q. Kareem, T. Mikó, G. Gergely, and Z. Gácsi. A review on the production of 17-4PH parts using press and sinter technology. Science Progress, 106 (1), (2023). doi: 10.1177/00368504221146060

[14]-Serafini FL, Peruzzo M, Krindges I, Ordoñez MF, Rodrigues D, Souza RM, Farias MC. Microstructure and mechanical behavior of 316L liquid phase sintered stainless steel with boron addition. Materials Characterization, 152, 253-64 (2019). doi: 10.1016/j.matchar.2019.04.009

[15]-Ertugrul O, Park HS, Onel K, W-P. M. Effect of particle size and heating rate in microwave sintering of 316L stainless steel. Powder Technology, 253,703-9 (2014). doi:10.1016/j.powtec.2013.12.043

[16]-Oh JW, Ryu SK, Lee WS, Park SJ. Analysis of compaction and sintering behavior of 316L stainless steel nano/micro bimodal powder. Powder Technology 322, 1-8 (2017). doi:10.1016/j.powtec.2017.08.055

[17]-Giganto S, Martínez-Pellitero S, Barreiro J, Zapico P. Influence of 17-4 PH stainless steel powder recycling on properties of SLM additive manufactured parts. Journal of Materials Research and Technology, 16, 1647-58 (2022). doi: 10.1016/j.jmrt.2021.12.089
[18]-Mohammad Moradi J, Emadoddin E and Omidvar H. Transient liquid phase bonding of 17-4-ph stainless steel using conventional and two-step heating process. Met Mater Int, 27, 5268–5277 (2020).
[19]-Zhang H. Powder injection molding of 17-4ph stainless steel. In: Metal Powder Industries Federation (ed) Powder injection molding symposium, 219–227 (1992).
[20]-Szewczyk-Nykiel A. The effect of the addition of boron on the densification, microstructure and properties of sintered 17-4 PH stainless steel. Technical Transactions Mechanics. In: Czasopismo Techniczne, 86–96 (2014).
[21]-Wang FZ, Wang QZ, Yu BH, et al. Interface structure and mechanical properties of Ti (C, N)-based cermet and 17–4PH stainless steel joint brazed with nickel-base filler metal BNi-2. J Mater Process Technol, 211, 1804–1809 (2011).
[22]-Patibandla AR. Effect of process parameters on surface roughness and porosity of direct metal laser sintered metals. Master thesis, University of Cincinnati, Cincinnati, USA, 2018.
[23]-Samal PK, Nandivada N, Hauer I, et al. Properties of 17-4ph stainless steel produced via press and sinter route. Adv Powder Metallurg Particulat Mater 2008; 7: 109–120.
[24]-Kazior J, Szewczyk-Nykiel A, Pieczonka T, Hebda M, Nykiel M. Properties of precipitation hardening 17-4 PH stainless steel manufactured by powder metallurgy technology. Advanced Materials Research 811, 87-92 (2013). doi: 10.4028/www.scientific.net/AMR.811.87
[25]-C.T. Schade, P.D. Stears, A. Lawley, R.D. Doherty. Precipitation-hardening PM stainless steels. International Journal of Powder Metallurgy, 43(4) (2007).
[26]-H. Irrinki. Mechanical properties and microstructure evolution of 17-4 PH stainless steel processed by laser-powered bed fusion. Master thesis, University of Louisville, 2016. doi:10.18297/etd/2408
[27]-S. Dobson, S. Vunnam, D. Frankel, C. Sudbrack, T. Starr. Powder variation and mechanical properties for SLM 17-4 PH stainless steel. in: International Solid Freeform Fabrication Symposium, University of Texas, Austin, United State of America, 2019. doi: 10.26153/tsw/17286
[28]-Muratal, Onur, and Ridvan Yamanoglu. Production of 316l stainless steel used in biomedical applications by powder metallurgy. IEEE-Scientific Meeting on electrical-Electronics & biomedical engineering and Computer Science (EBBT), 1-4 (2019).
[29]-Wu MW, Huang ZK, Tseng CF, et al. Microstructures, mechanical properties, and fracture behaviors of metal-injection molded 17-4PH stainless steel. Met Mater, 21, 531–537 (2015).
[30]-M. Vattur Sundaram, S. Karamchedu, C. Gouhier, E. Hryha, O. Bergman, L. Nyborg. Vacuum sintering of chromium alloyed powder metallurgy steels. Metal Powder Report, 74 (5), 244-250 (2019). doi: 10.1016/J.MPRP.2019.01.003
[31]-Coovattanachai, Ornmanee, Prayoon Lasutta, Nattaya Tosangthum, Rungtip Krataitong, Monnapas Morakotjinda, Anan Daraphan, Bhanu Vetayanugul, and Ruangdaj Tongsri. Analysis of compaction and sintering of stainless steel powders. Chiang Mai J. Sci 33 (2), 293-300 (2006).
[32]-Al-Mangour, Bandar. Powder metallurgy of stainless steel: state-of-the art, challenges, and development. Stainless Steel: Microstructure, Mechanical Properties and Methods of Application: Nova Science Publishers, 37-80 (2015).
[33]-Kondo, Suguru, Yuji Kume, Makoto Kobashi, and Naoyuki Kanetake. Densification behavior of different metal powders by compression and shear combined loading. Procedia Engineering 81, 1175-1179 (2014). doi: 10.1016/j.proeng.2014.10.284
[34]-Schade C. Processing, microstructures and properties of a dual phase precipitation-hardening PM stainless steel. Doctoral dissertation, Drexel University, Philadelphia, USA, 2010.
[35]-Kandala SR, Balani K, Upadhyaya A. Mechanical and electrochemical characterization of supersolidus sintered austenitic stainless steel (316 L). High Temperature Materials and Processes 38(2019), 792-805 (2019). doi: 10.1515/htmp-2019-0032

[36]-Szewczyk-Nykiel A, Bogucki R. Sinter-bonding of AISI 316L and 17-4 PH stainless steels. Journal of Materials Engineering and Performance 27, 5271-9 (2018). doi: 10.1007/s11665-018-3590-5
[37]-Samal PK, Nandivada N, Hauer I, Hoganas AB. Properties of 17-4 PH stainless steel produced via press and sinter route. Advances in Powder Metallurgy & Particulate Materials 7, 109-120 (2008).
[38]-Kurgan N, Varol R. Mechanical properties of P/M 316L stainless steel materials. Powder Technology 201(3), 242-7 (2010). doi: 10.1016/j.powtec.2010.03.041
[39]-Li D, Chen S, Shao WQ, et al. Application of master sintering curve theory to predict and control the sintering of nanocrystalline TiO_2 ceramic. Key Eng Mater, 368, 1588–1590 (2008).
[40]-Johnson DL. Solid-state sintering. In Brook RJ (ed) Concise encyclopedia of advanced ceramic materials. Pergamon: Elsevier, 454–458 (1991).
[41]-Bordia RK, Kang SJL and Olevsky EA. Current understanding and future research directions at the onset of the next century of sintering science and technology. J Am Ceram Soc, 100, 2314–2352 (2017).
[42]-U. ÇAvdar and E. Atik. Investigation of conventional-and induction-sintered iron and iron-based powder metal compacts. JOM, 66 (6), 1027–1034 (2014), doi: 10.1007/s11837-014-0977-0.
[43]-S. Raynova, Y. Collas, F. Yang, and L. Bolzoni. Advancement in the Pressureless Sintering of CP Titanium Using High-Frequency Induction Heating. Metall Mater Trans A Phys Metall Mater Sci, 50 (10), 4732–4742 (2019). doi: 10.1007/s11661-019-05381-z.
[44]-M. Ortega Varela de Seijas, A. Bardenhagen, T. Rohr, and E. Stoll. Indirect Induction Sintering of Metal Parts Produced through Material Extrusion Additive Manufacturing. Materials, 16 (2), 2023, doi: 10.3390/ma16020885.
[45]-Hermel, Waldemar, G. Leitner, and R. Krumphold. Review of induction sintering: fundamentals and applications. Powder metallurgy, 23 (3), 130-135 (1980).
[46]-S. Jayalakshmi, R. Singh, and M. Gupta. Metallic Glasses as Potential Reinforcements in Al and Mg Matrices: A Review. Technologies (Basel), 6 (2), 40 (2018). doi: 10.3390/technologies6020040.
[47]-Çavdar, U., E. Atik, and M. B. Akgul. Magnetic-thermal analysis and rapid consolidation of FE–3 wt.% CU powder metal compacts sintered by medium-frequency induction-heated system. Powder Metallurgy and Metal Ceramics 53 (2014): 191-198.
[48]-Blaine DC, Wu Y, Schlaefer CE, et al. Sintering shrinkage and microstructure evolution during densification of a martensitic stainless steel. In: Proceedings Sintering conference, 2003. Materials Research Institute, Pennsylvania State University, Pennsylvania, USA.
[49]-Kurgan N. Effect of porosity and density on the mechanical and microstructural properties of sintered 316L stainless steel implant materials. Materials & Design 55, 235-41(2014). doi: 10.1016/j.matdes.2013.09.058
[50]-De Mello JD, Binder R, Klein AN, Hutchings IM. Effect of compaction pressure and powder grade on microstructure and hardness of steam oxidised sintered iron. Powder Metallurgy 44(1), 53-61(2001). doi: 10.1179/003258901666176
[51]-Imgrund P, Rota A and Simchi A. Microinjection moulding of 316L/17-4PH and 316L/Fe powders for fabrication of magnetic–nonmagnetic bimetals. J Mater Process Technol, 200, 259–264 (2008).
[52]-HÖ. Gülsoy, S. Salman and S. Özbek. Effect of FeB additions on sintering characteristics of injection moulded 17-4PH stainless steel powder. J Mater Sci., 39, 4835–4840 (2004).
[53]-Hu, Y. Li, J. Lou, H. He, X. Zhang. Effects of sintering temperature and holding time on densification and mechanical properties of MIM HK30 stainless steel. International Journal of Metallurgy and Metal Physics, 3, 22 (2018). doi:10.35840/2631-5076/9222
[54]-T. S. Yoon, Y. H. Lee, S. H. Ahn, J. H. Lee, and C. S. Lee. Effects of sintering conditions on the mechanical properties of metal injection molded 316L stainless steel. ISIJ International, 43(1),119–126 (20030. doi: 10.2355/isijinternational.43.119.
[55]-M. A. Erden, N. Yaşar, M. E. Korkmaz, B. Ayvacı, K. Nimel Sworna Ross, and M. Mia. Investigation of microstructure, mechanical and machinability properties of Mo-added steel produced by powder metallurgy method. International Journal of Advanced Manufacturing Technology, 114 (9–10), 2811–2827 (2021). doi: 10.1007/S00170-021-07052-Z.

[56]-Bala P, Krawczyk J, Pawlowski B, et al. The kinetics of phase transformations during continuous heating from as-quenched state of 17-4PH steel. Metal 2015.
[57]-Trzepieciński T, Pieja T, Malinowski T, et al. Investigation of 17-4PH steel microstructure and conditions of elevated temperature forming of turbine engine strut. J Mater Process Technol, 252, 191–200 (2018).
[58]-Gulsoy HO, Ozbek S and Baykara T. Microstructural and mechanical properties of injection moulded gas and water atomised 17-4 PH stainless steel powder. Powder Metall, 50, 120–126 (2007).
[59]-Furlan KP, Binder C, Klein AN, et al. Thermal stability of the MoS2 phase in injection moulded 17-4 PH stainless steel. J Mater Res Technol, 1, 134–140 (2012).
[60]-Murray K, Coleman AJ, Tingskog TA, et al. Effect of particle-size distribution on processing and properties of MIM 17-4 PH. Int J Powder Metall, 47, 21–28 (2011).
[61]-Chagnon F and Trudel Y. Effect of density on mechanical properties of sinter hardened P/M materials. Advances in P/M & Particulate Materials, 3, 112–119(1999).
[62]-Kurgan N, Sun Y, Cicek B, Ahlatci H. Production of 316L stainless steel implant materials by powder metallurgy and investigation of their wear properties. Chinese science bulletin, 57, 1873-8 (2012). doi: 10.1007/s11434-012-5022-5
[63]-Yu Y, Li Y, Lou J, et al. Microstructure and mechanical properties of metal injection molding HK30 stainless steel sintered in N2 and Ar atmosphere. Int J Metallurg Metal Physics, 4, 30 (2019).
[64]-Zhang B, Yang F, Qin Q, et al. Characterisation of powder metallurgy H13 steels prepared from water atomised powders. Powder Metall, 63, 9–18(2020).
[65]-Chang CW, Chen PH and Hwang KS. Enhanced mechanical properties of injection molded 17-4PH stainless steel through reduction of silica particles by graphite additions. Mater Trans, 51, 2243–2250 (2010).
[66]-Jung ID, Ha S, Park SJ, et al. Two-phase master sintering curve for 17-4 PH stainless steel. Metall Mater Trans A, 47, 5548–5556(2016).
[67]-Firouzdor V and Simchi A. Co-sintering of M2/17-4PH powders for fabrication of functional graded composite layers. J Compos Mater, 44, 417–435(2010).
[68]-Bautista A, Moral C, Velasco F, et al. Density-improved powder metallurgical ferritic stainless steels for high-temperature applications. J Mater Process Technol, 189, 344–335(2007).
[69]-Konda Gokuldoss, P., Kolla, S. and J. Eckert. Additive manufacturing processes: Selective laser melting, electron beam melting and binder jetting—Selection guidelines. Materials, 10(6), 672(2017).
[70]-Ponnusamy, P., S. H. Masood, D. Ruan, S. Palanisamy, R. A. Rahman Rashid, and Omar Ahmed Mohamed. Mechanical performance of selective laser melted 17-4 PH stainless steel under compressive loading. (2017).
[71]-M. A. Aripin *et al.*, Effects of Build Orientations on Microstructure Evolution, Porosity Formation, and Mechanical Performance of Selective Laser Melted 17-4 PH Stainless Steel, Metals (Basel), 12(11), (2022). doi: 10.3390/met12111968.
[72]-Z. Hu, H. Zhu, H. Zhang, and X. Zeng. Experimental investigation on selective laser melting of 17-4PH stainless steel. Opt Laser Technol, 87,17–25 (2017). doi: 10.1016/j.optlastec.2016.07.012.
[73]-P. Ponnusamy *et al.*, A study of tensile behavior of SLM processed 17-4 PH stainless steel, in Materials Today: Proceedings, 4531–4534(2021). doi: 10.1016/j.matpr.2020.12.1104.
[74]-Z. Zhao *et al.*, Effect of Solution Temperature on the Microstructure and Properties of 17-4PH High-Strength Steel Samples Formed by Selective Laser Melting, Metals (Basel), 12 (3), 425 (2022). doi: 10.3390/met12030425.
[75]-Y. Sun, R. J. Hebert, and M. Aindow. Effect of laser scan length on the microstructure of additively manufactured 17-4PH stainless steel thin-walled parts. Addit Manuf, 35, (2020). doi: 10.1016/j.addma.2020.101302.

[76]-X. Lin, Y. Cao, X. Wu, H. Yang, J. Chen, and W. Huang. Microstructure and mechanical properties of laser forming repaired 17-4PH stainless steel. Materials Science and Engineering: A, 553, 80–88 (2012). doi: 10.1016/J.MSEA.2012.05.095.
[77]-C. Senthamarai Kannan, S. Sai Sree Chandra, G. Punith Krishnan, and S. Pravin Raj. A review on additive manufacturing of AA2024 and AA6061 alloys using powder bed fusion. IOPscience.iop.org, doi: 10.1088/1757-899X/988/1/012002.
[78]-F. Verhaeghe, T. Craeghs, J. Heulens, and L. Pandelaers. A pragmatic model for selective laser melting with evaporation. Acta Materialia, 57 (20), 6006–6012 (2009). doi: 10.1016/j.actamat.2009.08.027.
[79]-Zitelli, C., P. Folgarait, and A. Di Schino. Laser powder bed fusion of stainless steel grades: a review. Metals, 9, 731 (2019).
[80]-Popov, V.V., Grilli, M.L., Koptyug, A., Jaworska, L., Katz-Demyanetz, A., Klobčar, D., Balos, S., Postolnyi, B.O. and Goel, S., Powder bed fusion additive manufacturing using critical raw materials: A review. Materials, 14(4), 909 (2021).
[81]-S. Giganto, S. Martínez-Pellitero, J. Barreiro, P. Leo, and M. A. Castro-Sastre. Impact of the laser scanning strategy on the quality of 17-4PH stainless steel parts manufactured by selective laser melting. Journal of Materials Research and Technology, 20, 2734–2747 (2022). doi: 10.1016/j.jmrt.2022.08.040.
[82]-Sames, William J., F. A. List, Sreekanth Pannala, Ryan R. Dehoff, and Sudarsanam Suresh Babu. The metallurgy and processing science of metal additive manufacturing. International materials reviews, 61(5), 315-360 (2016).
[83]-Kudzal, Andelle, Brandon McWilliams, Clara Hofmeister, Frank Kellogg, Jian Yu, Joshua Taggart-Scarff, and Jianyu Liang. Effect of scan pattern on the microstructure and mechanical properties of Powder Bed Fusion additive manufactured 17-4 stainless steel. Materials & Design, 133, 205-215 (2017).
[84]-R. Rashid, S. H. Masood, D. Ruan, S. Palanisamy, R. A. Rahman Rashid, and M. Brandt. Effect of scan strategy on density and metallurgical properties of 17-4PH parts printed by Selective Laser Melting (SLM). J Mater Process Technol, 249, 502–511 (2017). doi: 10.1016/j.jmatprotec.2017.06.023.
[85]-Giganto, Sara, Pablo Zapico, Mª Ángeles Castro-Sastre, Susana Martínez-Pellitero, Paola Leo, and Patrizia Perulli. Influence of the scanning strategy parameters upon the quality of the SLM parts. Procedia Manufacturing 41, 698-705 (2019).
[86]-H. Gu and H. K. Rafi. Influences of Energy Density on Porosity and Microstructure of Selective Laser Melted 17-4PH Stainless Steel. 24th International Solid Freeform Fabrication Symposium - An Additive Manufacturing Conference, 474-489 (2013).
[87]-B. Spierings, M. Schoepf, R. Kiesel, and K. Wegener. Optimization of SLM productivity by aligning 17-4PH material properties on part requirements. Rapid Prototyp J, 20(6), 444–448(2014). doi: 10.1108/RPJ-04-2013-0045.
[88]-Du Plessis. Effects of process parameters on porosity in laser powder bed fusion revealed by X-ray tomography. Addit Manuf, 30, (2019). doi: 10.1016/j.addma.2019.100871.
[89]-Oliveira JP, Shamsolhodaei A, Shen J, et al. Improving the ductility in laser welded joints of CoCrFeMnNi high entropy alloy to 316 stainless steel. Mater Des, 219, 110717(2022).
[90]-Rodrigues TA, Escobar JD, Shen J, et al. Effect of heat treatments on 316 stainless steel parts fabricated by wire and arc additive manufacturing: microstructure and synchrotron X-ray diffraction analysis. Additive Manuf, 48, 102428(2021).
[91]-Abe Y, Kurose T, Santos M, et al. Effect of layer directions on internal structures and tensile properties of 17-4ph stainless steel parts fabricated by fused deposition of metals. Materials (Basel), 14, 243(2021).
[92]-Sunil B and Rajanna S. Evaluation of mechanical properties of ferrite-martensite DP steels produced through intermediate quenching technique. SN Appl Sci, 2, 1–8(2020).

[93]-S. M. Yeon *et al.*, Normalizing Effect of Heat Treatment Processing on 17-4 PH Stainless Steel Manufactured by Powder Bed Fusion, Metals (Basel), 12(5), (2022). doi: 10.3390/met12050704.
[94]-D. J. Shaffer, A. E. Wilson-Heid, J. S. Keist, A. M. Beese, and T. A. Palmer. Impact of retained austenite on the aging response of additively manufactured 17-4 PH grade stainless steel. Materials Science and Engineering: A, 817, (2021). doi: 10.1016/j.msea.2021.141363.
[95]-H. Eskandari, H. R. Lashgari, L. Ye, M. Eizadjou, and H. Wang. Microstructural characterization and mechanical properties of additively manufactured 17–4PH stainless steel. Mater Today Commun, 30, (2022). doi: 10.1016/j.mtcomm.2021.103075.
[96]-D. F. Susan, T. B. Crenshaw, and J. S. Gearhart. The Effects of Casting Porosity on the Tensile Behavior of Investment Cast 17-4PH Stainless Steel. J Mater Eng Perform, 24(8), 2917–2924(2015). doi: 10.1007/s11665-015-1594-y.
[97]-Isogawa S, Yoshida H, Hosoi Y, et al. Improvement of the forgability of 17-4 precipitation hardening stainless steel by ausforming. J Mater Process Technol, 74, 298–306(1998).
[98]-Murthy AS. Role of alloy additions on strengthening in 17-4 PH stainless steel. Doctoral dissertation, Missouri University of Science and Technology, Rolla, Missouri, USA, 2012.
[99]-D. Gu, M. Guo, H. Zhang, Y. Sun, R. Wang, and L. Zhang. Effects of laser scanning strategies on selective laser melting of pure tungsten. International Journal of Extreme Manufacturing, 2,(2),(2020). doi: 10.1088/2631-7990/ab7b00.
[100]-S. E. Kovacs *et al.*, Additive Manufacturing of 17-4PH Alloy: Tailoring the Printing Orientation for Enhanced Aerospace Application Performance, Aerospace, 10(7), (2023). doi: 10.3390/aerospace10070619.
[101]-Lashgari HR, Kong C, Adabifiroozjaei E, Li S, Microstructure, post thermal treatment response, and tribological properties of 3D printed 17-4 PH stainless steel, Wear. 456, 203367 (2020). doi: 10.1016/j.wear.2020.203367.
[102]-Y. H. Cho, S. Y. Park, J. Y. Kim, and K. A. Lee. 17-4PH stainless steel with excellent strength–elongation combination developed via material extrusion additive manufacturing. Journal of Materials Research and Technology, 24, 3284–3299 (2023). doi: 10.1016/j.jmrt.2023.03.228.
[103]-P.K. Samal, J.D. Pannell, Effect of Process Variables on the Dimensional Change of 434L Stainless Steel, Materials Science, North American Höganäs. Hollsopple, PA15935, 2011.
[104]-Tillmann W, Dias NF, Stangier D, Schaak C, Höges S. Heat treatment of binder jet printed 17–4 PH stainless steel for subsequent deposition of tribo-functional diamond-like carbon coatings. Materials & Design, 213, 110304(2022). doi: 10.1016/j.matdes.2021.110304
[105]-J.S. Weaver, J. Whiting, V. Tondare, C. Beauchamp, M. Peltz, J. Tarr, et al. The effects of particle size distribution on the rheological properties of the powder and the mechanical properties of additively manufactured 17-4 PH stainless steel. Additive Manufacturing, 39, 10185(2021). doi: 10.1016/j.addma.2021.101851
[106]-Bandi B, Van Krevel J, Srirangam P. Interaction between ferrite recrystallization and austenite formation in dual-phase steel manufacture. Metallurgical and Materials Transactions A, 53 (4), 1379-93(2022). doi: 10.1007/s11661-022-06597-2
[107]-Ullah, M. Wasif, and M. Tufail. Analysis of shrinkage and dimensional accuracy of additively manufactured tooling for the composite manufacturing. International Journal on Interactive Design and Manufacturing, 18 (2), 673–684(2024). doi: 10.1007/s12008-023-01640-x.
[108]-M.G. Kamardan, N.H.A. Zaidi, M.N. Dalimin, A.M.A. Zaidi, S.B. Jamaludin, M.M.A. Jamil. The sintering temperature effect on the shrinkage behavior of cobalt chromium alloy. American Journal of Applied Sciences, 7(11), 1443(2010).
[109]-T. Maki, Morphology and substructure of martensite in steels, Phase transformations in steels, 2, 34-58(2012). doi: 10.1533/9780857096111.1.34
[110]-G. Jacob and G. Jacob. Prediction of solidification phases in Cr-Ni stainless steel alloys manufactured by laser based powder bed fusion process. NIST Advanced Manufacturing Series 100-14, 2018. doi: 10.6028/NIST.AMS.100-14.

[111]-S. B. Pratomo, H. Oktadinata, T. W. Widodo. Effect of nickel additions on microstructure evolution and mechanical properties of low-alloy Cr-Mo cast steel. IOP Conference Series: Materials Science and Engineering, 541 (1), 0120502019(2019). doi: 10.1088/1757-899X/541/1/012050.
[112]-P. Zapico, S. Giganto, J. Barreiro, and S. Martínez-Pellitero. Characterisation of 17-4PH metallic powder recycling to optimise the performance of the selective laser melting process. Journal of Materials Research and Technology, 9(2), 1273–1285(2020). doi: 10.1016/J.JMRT.2019.11.054.
[113]-M. Q. Kareem, T. Mikó, G. Gergely, and Z. Gácsi. Compaction behaviours of 17-4 PH, 316L, and 1.4551 stainless-steel powders during cold pressing. Results in Engineering, 23, (2024). doi: 10.1016/j.rineng.2024.102452.
[114]-Z. Cui, S. He, J. Tang, D. Fu, J. Teng, and F. Jiang. Effect of Grain Size on the Plastic Deformation Behaviors of a Fe-18Mn-1.3Al-0.6C Austenitic Steel. Materials, 15(24), (2022), doi: 10.3390/ma15248717.
[115]-M. Higashi, N. Kanno. Effect of initial powder particle size on the hot workability of powder metallurgy Ni-based superalloys. Materials & Design, 194, 108926(2020). doi: 10.1016/j.matdes.2020.108926.
[116]-V. L. de la Concepción, H. N. Lorusso, and H. G. Svoboda. Effect of Carbon Content on Microstructure and Mechanical Properties of Dual Phase Steels. Procedia Materials Science, 8, 1047–1056(2015). doi: 10.1016/j.mspro.2015.04.167.
[117]-M. Q. Kareem, T. Mikó, G. Gergely, and Z. Gácsi. Optimisation of powder metallurgy technology of 17-4 PH material. Heliyon, 11(4),(2025). doi: 10.1016/j.heliyon.2025.e42658.
[118]-K. Zyguła *et al.*, The Influence of Induction Sintering on Microstructure and Deformation Behavior of Ti-5Al-5Mo-5V-3Cr Alloy, Metall Mater Trans A Phys Metall Mater Sci, 52(5), 1699–1713(2021). doi: 10.1007/s11661-021-06179-8.
[119]-Wilcox, H., B. Lewis, and P. Styman. Evaluation of the mechanical properties of precipitation-hardened martensitic steel 17-4ph using small and shear punch testing. Journal of Materials Engineering and Performance, 30 (6), 4206-4216(2021). doi: 10.1007/s11665-021-05756-7.
[120]-Martin *et al.*, Dynamics of pore formation during laser powder bed fusion additive manufacturing, Nat Commun, 10(1), (2019). doi: 10.1038/s41467-019-10009-2.
[121]-Sun, Yu, Rainer J. Hebert, and Mark Aindow. Effect of heat treatments on microstructural evolution of additively manufactured and wrought 17-4PH stainless steel. Materials & Design, 156, 429-440(2018).
[122]-T. Ronneberg, C. M. Davies, and P. A. Hooper. Revealing relationships between porosity, microstructure and mechanical properties of laser powder bed fusion 316L stainless steel through heat treatment. Mater Des,189, (2020). doi: 10.1016/j.matdes.2020.108481.
[123]-Cheruvathur, Sudha, Eric A. Lass, and Carelyn E. Campbell. Additive manufacturing of 17-4 PH stainless steel: post-processing heat treatment to achieve uniform reproducible microstructure. Jom, 68, 930-942(2016).
[124]-M. Shehata, T. M. Hatem, and W. A. Samad. Experimental Study of Build Orientation in Direct Metal Laser Sintering of 17-4PH Stainless Steel. 3D Print Addit Manuf, 6(4), 227–233(2019). doi: 10.1089/3dp.2017.0106.
[125]-S. Sabooni *et al.*, Laser powder bed fusion of 17–4 PH stainless steel: A comparative study on the effect of heat treatment on the microstructure evolution and mechanical properties, Addit Manuf, 46, (2021). doi: 10.1016/j.addma.2021.102176.
[126]-N. Haghdadi, M. Laleh, M. Moyle, and S. Primig. Additive manufacturing of steels: a review of achievements and challenges. Journal of Materials Science, 56, 64-107(2021). doi: 10.1007/s10853-020-05109-0.